TUNING THE ELECTRONIC AND MAGNETIC PHASES IN CaB_6, $PtSb_2$ AND Yb_3Pt_4

by

Marcus C. Bennett

A dissertation submitted in partial fulfillment
of the requirements for the degree of
Doctor of Philosophy
(Physics)
in The University of Michigan
2009

Doctoral Committee:

Professor James W. Allen, Co-Chair
Professor Meigan C. Aronson, Stony Brook University, Co-Chair
Professor Myron K. Campbell
Professor Rodney C. Ewing
Professor Cagliyan Kurdak
Assistant Professor Alexei V. Tkachenko

TABLE OF CONTENTS

CHAPTER

LIST OF FIGURES

Figure

LIST OF TABLES

Table

CHAPTER I

Introduction

This thesis is a study of magnetic materials that contain both local magnetic moments and itinerant electrons or holes. We investigate how changing both the carrier concentration (n) and the local magnetic moment concentration (N) affect the magnetic and electronic properties of a system. An overview of different types of magnetic materials is plotted on a carrier concentration - magnetic moment concentration (n-N) diagram (Fig. 1.1). We present the experimental results of compounds representing three different regions on the n-N plane. In each case, we are motivated by reports of observations of new electronic and magnetic phenomena. In this thesis, we perform extensive measurements and analysis of compounds that display these unexplained phenomena in an effort to better understand the mechanisms that lead to them.

1.1 Thesis Organization

In the remaining part of this first chapter, we introduce the novel electronic and magnetic phases associated with the three different regions on the n-N plane that we present in this thesis. We first introduce the Wigner lattice, which is located at the lower left corner, in the N=0, and low n region of Figure 1.1. In the next section, we introduce the unexplained dependences of T_C on n and N for dilute

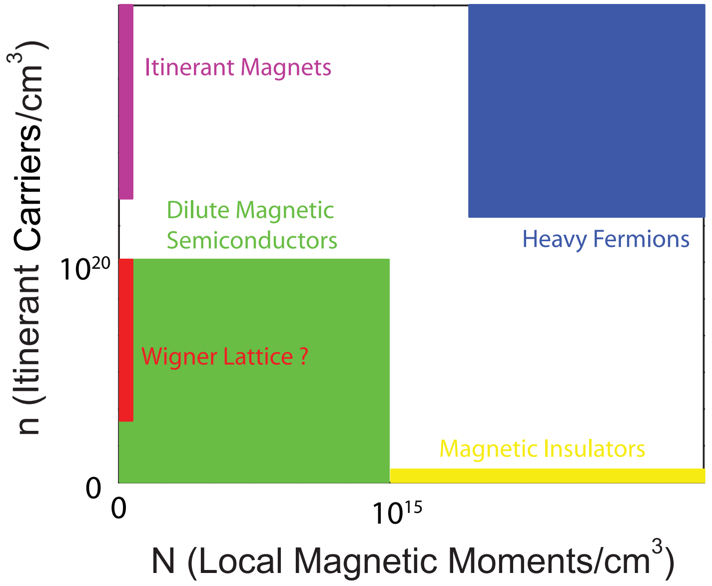

Figure 1.1: Schematic of different types of magnetism based on the local magnetic moment concentrations and itinerant carrier concentrations of the host materials.

magnetic semiconductors (DMS) located at the low to moderate N and n region of the plot. In the following section, we introduce the magnetic heavy fermion materials that have a quantum critical point (QCP), which are located in the hign N and n region. Chapter 2 is a description of the experimental techniques that were used. In Chapter 3, a description of the flux growth method that was used to grow all the single crystals of CaB_6, $PtSb_2$, and Yb_3Pt_4 that we studied is presented. In Chapters 4 through 6, our experimental results on each of the three compounds are presented. In the concluding chapter, we summarize our results and suggest further studies and measurements.

1.2 The Wigner Lattice

We begin our study at the low n, and N=0 region, where we use the semiconductor, CaB_6, to search for and study the properties of a three dimensional ferromagnetic Wigner lattice, which had never been observed until it was reportedly observed in La doped CaB_6 by Young et al in 1999 [1]. The observation of ferromagnetism in

$Ca_{1-x}La_xB_6$ (0.001<x<0.05) with Curie temperatures of 600 - 900 K was remarkable considering its semiconducting character and non-magnetic elements [1]. The maximum saturation moment, $M_S = 0.07\ \mu_B$ per electron was found at x=0.005, which is an average separation of 25 $\mathring{A}$ between neighboring electrons. With such large interelectron distances, it was concluded that a previously unobserved type of mechanism had to be responsible for the ferromagnetism. The proposed mechanism was the Wigner lattice, a decades old theory proposed by E. Wigner in the 1930s. Wigner showed that an electron gas in a positive background will crystallize into a lattice at sufficiently low density. A two dimensional Wigner lattice was experimentally observed in 1979 when electrons were floated on liquid helium [2, 3], but a three dimensional Wigner lattice has never been observed.

In an effort to observe and fully characterize the proposed Wigner lattice in doped CaB_6, we measured the field dependence of the magnetization of single crystals of electron doped CaB_6 at different temperatures over an extensive range of electron concentrations ranging from 10^{16} cm^{-3} to 10^{20} cm^{-3}, which were determined by Hall voltage measurements, but found no correlation between electron concentration and ferromagnetism. Electron microprobe analysis and magnetization measurements of some of the single crystals before and after acid etching found a correlation between ferromagnetism and the presence Fe and Ni impurities found on the crystal surfaces.

1.3 Tuning the Curie Temperature in Dilute Magnetic Semiconductors

We next move on to the low to moderate n and N region of the plot, represented by the dilute magnetic semiconductors. In this region, we measure $PtSb_2$ doped with rare earth elements. Previous measurements of dilute magnetic semiconductors (DMS) show unexplained dependences of T_C on n and N [4]. The purpose is to explore the possibility of controlling both n and N by doping, and then, after measurements of the electronic and magnetic properties, determining and explaining the relation between n, N and the Curie temperature (T_C) of the ferromagnetic crystals. From our experiments, we hoped to learn how the interactions between localized magnetic moments evolve from dipolar when n=0 to Ruderman Kittel Kasuya Yosida (RKKY) when both n and N are large. We also wanted to determine how the n and N dependence of T_C evolves from $T_C \propto N$ in the low n, high N region, such as in the rare earth chalcogenides, where we expect dipolar interactions dominate [5] to $T_C \propto n^2$ in the high n and N region, such as in the rare earth elements, Er, Tm and Dy, where we expect RKKY interactions to dominate [6, 7, 8]. In principle, in magnetic semiconductors, both the carrier concentration and local magnetic moment concentration can be controlled independently by adding either electrons or magnetic moments by doping with the appropriate elements. We synthesized a variety of single crystals of $PtSb_2$ doped with Ce, Gd, La and Yb and measured their electronic and magnetic properties. We found evidence for ferromagnetism in some of our crystals, and evidence for superconductivity in others, but in each case, we determined that these effects resulted from secondary impurity phases that formed on the surfaces of our crystals.

1.4 Quantum Critical Points in Heavy Fermion Compounds

The study of compounds in the high n and N section of figure 1.1, represented by rare earth based heavy fermion compounds, is the main focus of this thesis and was motivated by the discovery of quantum critical points (QCP) and their associated novel phases of matter, including an unconventional non-Fermi liquid (NFL) metallic state such as that observed in magnetic field tuned $YbRh_2Si_2$ [9] and pressure tuned

$CeCu_{6-x}Au_x$ [10], and unconventional superconductivity, such as that observed in the pressure tuned materials, $CePd_2Si_2$ [11] and $CeCu_2(Si_{0.9}Ge_{0.1})_2$ [12]. A QCP is a point at T=0 at which a second order phase transition takes place and is thus not driven by thermal fluctuation, but by zero point quantum fluctuations and is thus known as a quantum phase transition (QPT). Intense experimental and theoretical efforts are underway to try to better understand these novel phases, QPTs and the QCP itself [13, 14] and the four examples listed above are examples of magnetic field or pressure tuned rare earth based heavy fermion quantum critical systems that have been most thoroughly measured and studied. Since the early 1990s many metallic magnetic compounds have been tuned to quantum critical points by doping [15, 16], however, because doping introduces disorder, which significantly affects the physcial properties of magnetic metals, a tuning parameter other than doping should be used to tune the system to a quantum critical point. Thus, there is a shortage of stoichiometric materials to study that host quantum criticality and one of the goals of our research group is to synthesize new materials that host quantum criticality.

We have synthesized a new binary intermetallic antiferromagnet, Yb_3Pt_4, that can be tuned to a QCP with the application of a 1.6 T magnetic field, when the field is applied parallel to the rhombohedral a-axis of the crystal. We have extensively measured the properties of Yb_3Pt_4 in magnetic fields up to 9 T and temperatures as low as 60 mK, and have constructed a magnetic field-temperature (H-T) phase diagram to illustrate the unique properties of this new quantum critical antiferromagnet. In Chapter 6, we present our extensive measurements and results of the field and temperature dependences of the heat capacity, magnetization, AC magnetic susceptibility, and resistivity. Yb_3Pt_4 is a new unique quantum critical material with an unusual transition from a local moment paramagnet to a local moment antiferromagnet via a weakly first order phase transition at T_N=2.4 K. As the applied magnetic field increases, T_N decreases and the first order phase line terminates at a critical endpoint near 1.5 T and 1.2 K. As the magnetic field is further increased, T_N continues to decrease and reaches a QCP at 1.6 T. The properties of Yb_3Pt_4 deviate significantly from those of $YbRh_2Si_2$ and $CeCu_{6-x}Au_x$, suggesting a new scenario for quantum criticality is realized in Yb_3Pt_4.

CHAPTER II

Experimental Methods

In this chapter, we describe the experimental techniques used to measure the thermal, electronic and magnetic properties of the single crystals of CaB_6, doped $PtSb_2$ and Yb_3Pt_4 that we studied in this thesis. Most of the heat capacity and resistance measurements were performed using the ^3He insert option of our Quantum Design Physical Properties Measurement System (PPMS) at temperatures as low as 0.38 K and at magnetic fields as high as 9 T. We also have a second PPMS equipped with a 14 T magnet and a dilution refrigerator insert capable of temperatures as low as 50 mK. All of the magnetization and AC magnetic susceptibility measurements were performed using a Quantum Design Magnetic Properties Measurement System (MPMS) at temperatures ranging from 1.8 K to 300 K and in magnetic fields as high as 7 T.

2.1 Specific Heat

All heat capacity measurements were performed in a Quantum Design Physical Properties Measurement System (PPMS), with a 9 T superconducting magnet, and a ^3He insert, allowing access to temperatures as low as 0.38 K. The PPMS measures the heat capacity at constant pressure, $C_P=(dQ/dT)_P$, where Q is the flow of heat out of the crystal, using a numerical method developed by Hwang et al [17] [18]. This section begins with a description of the crystal mounting procedure, and the basic hardware, followed by a discussion of Quantum Design's measurement method and fitting technique. It is then shown how this fitting technique fails near very sharp phase transitions, and a method to estimate the latent heat of a first order phase transition using the PPMS raw data is introduced.

2.1.1 Hardware and Crystal Mounting

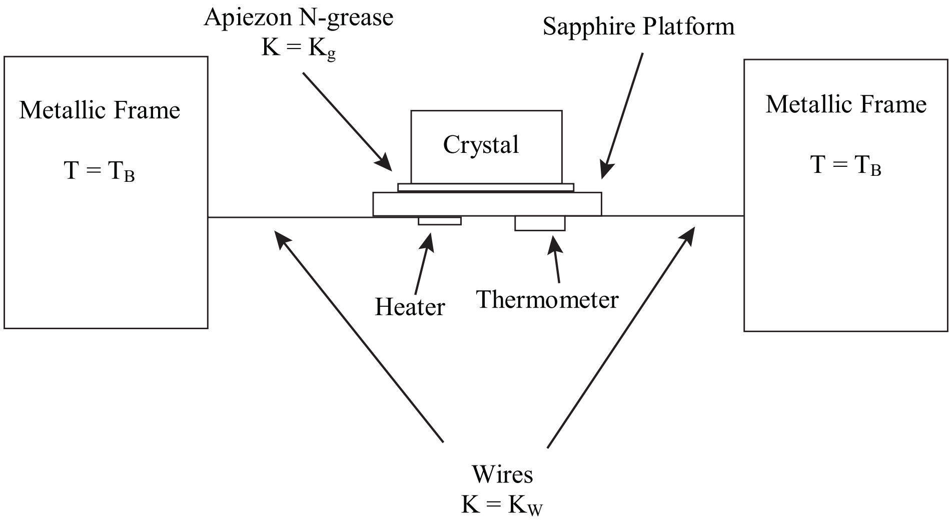

Figure 2.1: Schematic of the heat capacity hardware, and associated thermal connections. K_g is the thermal conductance of the grease, and K_W is the thermal conductance of the wires, and T_B is the temperature of the puck frame, which acts as the thermal bath.

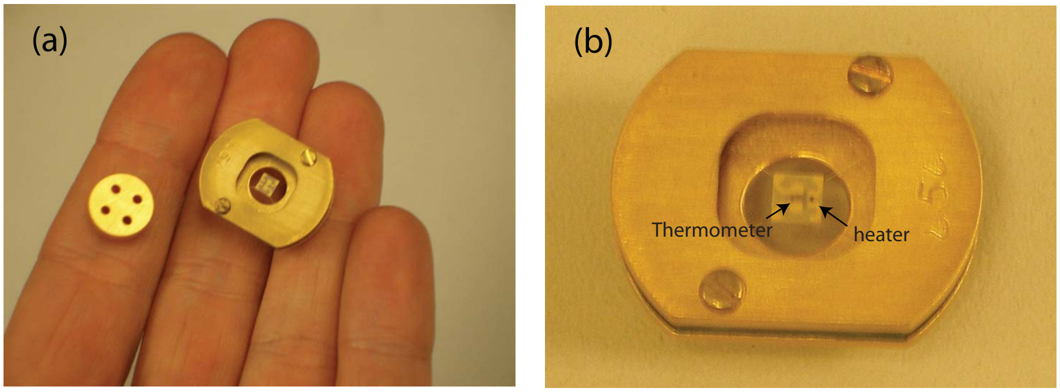

Figure 2.2: (a) Picture of the heat capacity puck used to mount the crystal for measurement in the He-3 insert of the PPMS. (b) A close-up picture of the heat capacity puck with the heater and the thermometer visible on the underside of the platform.

Fig. 2.1 is a schematic representing a single crystal mounted on the heat capacity puck. A small amount of Apiezon N grease is used to hold the crystal in place on a sapphire platform. The grease also acts as a good thermal connection between the crystal and the platform. A thermometer and a heater are located on the underside of the platform, which is suspended by four platinum wires that also serve as voltage and current leads for the heater and the thermometer, and provide a thermal connection to the surrounding bath (the metallic puck frame). Figure 2.2 shows two pictures of the heat capacity puck, including a close-up (Fig. 2.2(b)) that reveals the heater and the thermometer on the underside of the platform.

2.1.2 Measurement Technique

Since its start in the early 20^{th} century, a number of heat capacity measurement techniques and instruments have been developed [18, 19, 20, 21, 22, 23]. Quantum Design uses a numerical method developed by Hwang et al [17, 18] based on a thermal relaxation method. Lashley et al [19] provide a good review of the measurement technique, and the fitting method used in the PPMS to obtain the specific heat from the raw data. The heater applies a constant power, P, increasing the temperature of the system to T+ΔT (ΔT/T≈1%). The heater is then turned off, and the system is allowed to cool, losing heat through the wires to the bath at a rate, $P=K_W T$. Referring to Fig. 2.1, the flow of heat through the system is described by the two differential equations,

$$P = C_P \frac{dT_P}{dt} + K_g(T_P - T_C) + K_W(T_P - T_B)$$

$$0 = C_C \frac{dT_C}{dt} + K_W(T_C - T_P)$$

where P is the constant power applied by the heater, C_C is the heat capacity of the single crystal, C_P is the heat capacity of the platform, including the heater, thermometer, and the grease, T_C is the crystal temperature, T_P is the platform temperature, T_B is the temperature of the thermal bath (puck frame), K_g is the thermal conductance through the N-grease between the crystal and the platform, and K_W is the thermal conductance through the wires.

Ideally, the grease provides an excellent thermal connection between the sample and the platform, so that $K_g >> K_W$, and $T_C \approx T_P$. In the PPMS fitting routine, this assumption is called the "simple model". For this case, the two above expressions above simplify to one differential equation,

$$P = (C_P + C_C)\frac{dT_C}{dt} + K_W(T_C - T_B)$$

where P is constant during heating, and zero during cooling. During the cooling phase (P = 0), the entire platform, crystal, and grease cool exponentially as one unit, resulting in a simple solution to the differential equation:

$$T_C(t) = T_B + \Delta T e^{(-t/\tau)}$$

where $\tau=(C_P+C_C)/K_W$, and $\Delta T=T(t)-T_B$. Using this simplified picture to determine the heat capacity is often called the relaxation method [19, 20, 21, 22]. In the relaxation method, the total heat capacity, $C_{tot}=C_P+C_C$, is easily obtained by plotting the raw T(t) vs. t data on a log scale. The result is a straight line representation of the temperature decay region, whose slope is equal to $1/\tau$. Knowing the value of K_W, a linear fit is all that is required to determine C_{tot}. K_W is determined by measuring the temperature rise as a constant heater power is applied. Generally, the temperature dependence of C_P, C_C, and K_W are insignificant during the small temperature rise that occurs during the measurement. C_P, the platform heat capacity is determined by measuring the heat capacity of the entire platform with just the grease, before adding and measuring the crystal. This initial measurement determines C_P over the desired temperature range, which is then subtracted from the total heat capacity, $C_{tot}=C_P+C_C$.

Using the fitting method developed by Hwang et al [18], the PPMS numerically fits the entire T(t) vs. t heat pulse. It attempts to fit the data using both the simple model ($K_g >> K_W$), and the two tau method, which includes the heat flow between the crystal and the platform. The PPMS chooses the result of the model that gives a better fit. This is one of the strengths of the Quantum Design fitting method. It can measure the specific heat even when the crystal is not thermally well connected to the platform. In the following section, raw data taken using a single crystal of Yb_3Pt_4 will be used to illustrate how the PPMS fitting routine tails near very sharp phase transitions.

2.1.3 Very Sharp Phase Transitions

The fitting method used by the PPMS to obtain heat capacity values from raw data, does not yield accurate results near sharp phase transitions. Lashley et al [19] show, using a single crystal of Sm_2IrIn_8 near its first order phase transition at 14 K, that the PPMS, with its current fitting routine, is unable to obtain an accurate value for the heat capacity from the raw data for first order phase transitions near the critical temperature. In fact, the PPMS is unable to accurately measure any sharp phase transition near the critical temperature, whether it is first order or sharply second order. Measurements carried out on Yb_3Pt_4 near its very sharp, weakly first order magnetic phase transition at 2.4 K (Fig. 2.3) will be used to illustrate this point.

This weakly first order phase transition shows a decrease in latent heat as the magnetic field is increased, and resembles a second order phase transition when H = 1 T. A close look at the raw temperature versus time data reveals a way to differentiate a first order phase transition from a sharp second order transition, and to estimate its latent heat. At temperatures just below, and just above the transition, the PPMS

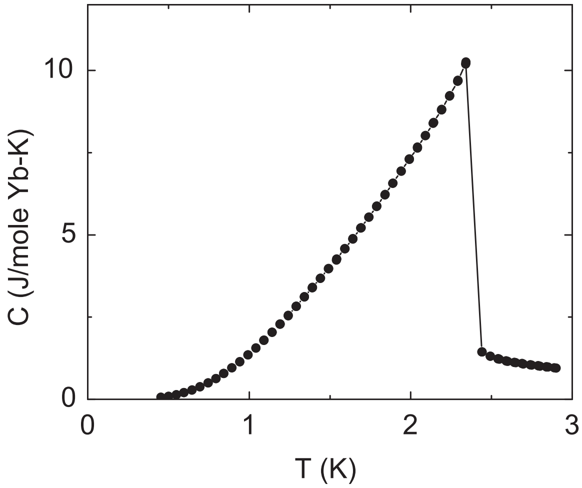

Figure 2.3: The temperature dependence of the specific heat near the weakly first order magnetic transition at 2.4 K. Because the transition in Yb_3Pt_4 is very sharp, the PPMS is unable to accurately fit the raw T(t) vs. t data.

fitting routine is accurate. Figure 2.4 shows a typical result for Yb_3Pt_4 just below the critical temperature, where the temperature versus time raw data fits well to the simple model employed by the PPMS, yielding an accurate result. It is easy to check the PPMS value for the heat capacity by applying the relaxation method to the cooling section of the raw data. As described previously, on a logarithmic scale, the exponential decay yields a straight line with the slope equal to $1/\tau$. However, the shape of the raw data changes significantly, when, during the heat pulse, the temperature rises through the critical temperature (Fig. 2.5). For this case, the fitting routine will not give an accurate result, because it tries to fit to a region with a single constant heat capacity, but the raw data has two regions with two different heat capacities. The two regions are clearly seen on a logarithmic scale (Fig. 2.5(b)). The steeper sloped, high temperature linear region represents the lower specific heat, at temperatures just above the T_C. The smaller sloped linear region represents the

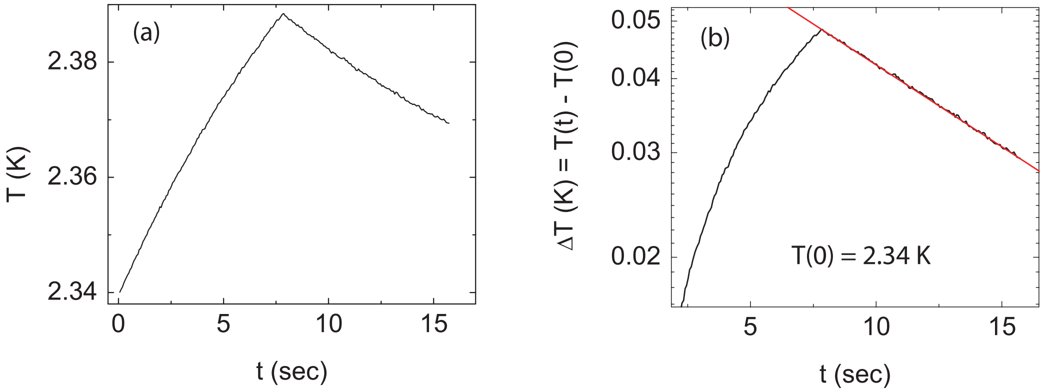

Figure 2.4: (a) Plot of the T(t) vs. t raw data used to determine the heat capacity of the Yb_3Pt_4 crystal just below the sharp phase transition at 2.4 K. (b) T-T_B vs. t on a semilog scale to show the linear region with slope equal to τ^{-1}

higher specific heat at temperatures just below T_C. The non-linear region in between represents the time during which there is a flow of latent heat associated with the first order phase transition. Ideally, the signature of a latent heat is a completely flat

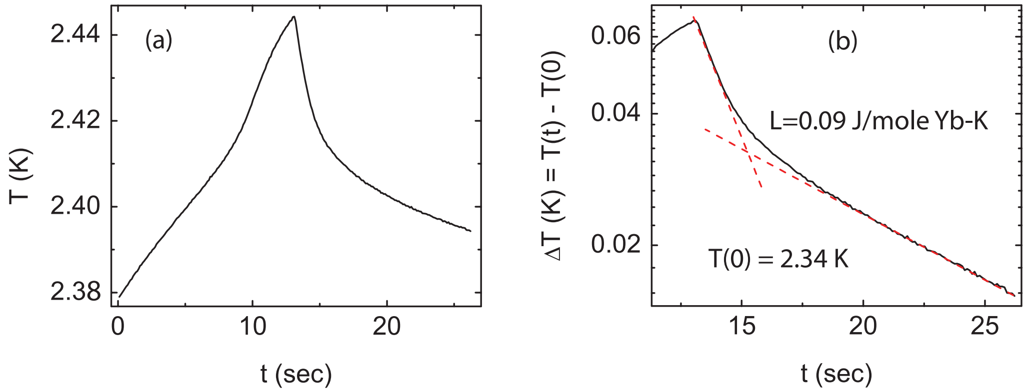

Figure 2.5: (a) The T(t) raw data with the heat pulse passing through the transition temperature. Attmepting to fit this data using the simple model will not give an accurate result.(b) The raw data plotted as ΔT vs t on a semilog scale. There are two different regions, the steeper slope representing the heat capacity just above the transition and the smaller slope representing the heat capacity just below the transition. The non-linear region in between is the signature of the latent heat associated with the first order phase transition.

horizontal line both on the temperature rise side, and the temperature decay side of the T(t) vs. t raw data. However, the condition depicted in Fig. 2.1 is far from ideal. Only the crystal is experiencing the first order phase transition. The platform, grease, thermometer, and heater do not. Even though the temperature of the crystal is not changing, the temperature of the other components continues to change as heat is added to or removed from the system. The result is the non-linear region observed in Fig. 2.5(b). The heat flow during the decay cycle can be estimated using dQ/dt=$K_W \Delta T$. K_W is calculated by the PPMS at each temperature, and does not change much over the temperature range of the zero-field 2.4 K phase transition. Near 2.4 K, it is approximately 5×10^{-7} J/Sec-K. The latent heat is then estimated by multiplying the power by the length of time the raw data remains in the non-linear region. As indicated in the figure, we estimate a latent heat of 0.09 J/mole Yb-K. In chapter 6, we will show how the latent heat changes as a function of applied magnetic field.

2.2 Resistivity

In this section we describe the technique used to measure the resistivity and the Hall effect. We describe the crystal mounting procedure, the hardware used, and the measurement method. Using the ^{3}He insert, we were able to measure the resistance from 0.38 K up to 300 K in fields up to 9 T. This enables the measurement of the magnetoresistance in addition to the usual temperature dependence of the resistivity, which is especially useful when creating magnetic field-temperature phase diagrams, like the one for Yb_3Pt_4. As described below, with the 9 T field, we can calculate the charge carrier concentration via measurements of the Hall effect.

2.2.1 Hardware and Crystal Mounting

The first step in the crystal mounting procedure is to make sure that the crystal is free of any macroscopic impurities, and that the surface is clean. The quantity of importance is the resistivity, ρ=RA/L, where A is the cross sectional area of the sample, R is the measured resistance and L is the distance between the voltage leads.

Thus, before attaching electrical leads and mounting the crystal on the PPMS puck, its shape and dimensions need to be measured and recorded. The PPMS comes equipped with a 8 pin plug-in crystal mounting stage (Fig. 2.6(a)). As shown in the diagram, the crystal need to be mounted on the plug-in stage. The stage has room for two crystals, to be wired to each set of four pads, consisting of two outer current leads (I^+, I^-) and two inner voltage leads (V^+, V^-). Figure 2.7 is a picture of an actual resistance puck with two crystals attached. The crystal should first be glued onto the stage using GE varnish, but care must be taken to put varnish only on the side of the crystal that will be glued to the stage. If excess varnish accidentally gets onto the wiring side of the crystal, it needs to be promptly removed, or it will interfere with the crystal contacts. Once the varnish is dried, and the crystal is held to the surface, small gauge platinum wire is used to connect each lead from the crystal surface to the correct contact pads on the stage. The first step is to attach four platinum wires to the crystal, two outer current leads, and two inner voltage

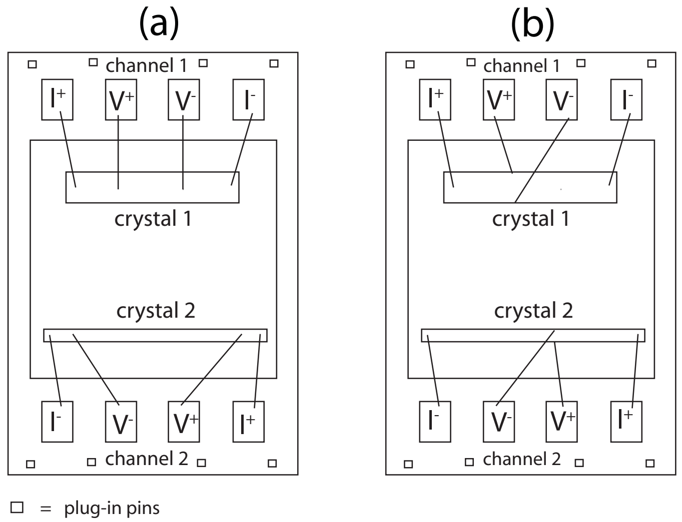

Figure 2.6: (a) A schematic of the mounting stage used for doing regular temperature or magnetic field dependent resistance measurements using the ^{3}He insert of the PPMS. (b) The same schematic as in (a), but with the crystals wired to obtain the magnetic field dependent Hall voltage.

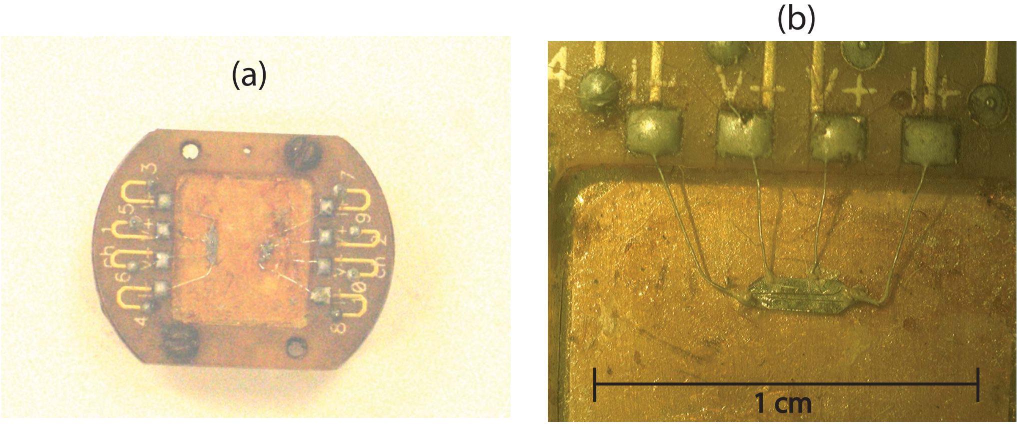

Figure 2.7: (a) A picture of the resistance puck used for the PPMS ^{3}He insert with two crystals mounted. The Pt wires are attached to the crystals using silver epoxy and to the puck frame using regular Pb-Sn solder. (b) A close-up of the crystal attached at channel 1.

leads. The Pt leads should be cut roughly 1 cm long. The best way to place them on the crystal surface is by using tweezers to dip one end of a Pt wire into silver epoxy, then carefully place that end at the proper position on the crystal surface. Once all four leads have been laid onto the crystal, the epoxy needs to be cured for several hours at about 100 C. The entire crystal plus stage can be placed in the oven as long as the temperature is kept near or below 100 C. When the epoxy is cured the two-lead contact resistance needs to be measured. Any resistance above $\sim 10\ \Omega$ is too high. To obtain a lower contact resistance, the first thing to try is to put a relatively high current through the bad contact. If no improvement in the contact resistance is achieved using a maximum of 100 μA, the contact needs to be redone. Silver epoxy contacts can be removed by soaking them in a 50/50 mix of methanol and toluene. Once the contact resistances of the silver epoxy joints are at acceptable values, the other ends of the Pt wires can be attached to the contact pads of the stage using regular Pb-Sn solder with any standard flux and any standard soldering iron. After all the leads are attached, it is advisable to check the resistance of the crystal using at least one other method such as lock-in amplifier, or a sensitive four lead digital voltmeter to be compared to the value given by the PPMS, to verify that neither the contacts nor the crystal itself has been damaged by the mounting process and is ready to be measured. After this test, the crystal holding stage can be placed back in its 8 pin holder.

2.2.2 The PPMS Resistance Measurement Method

As described in the Quantum Design Hardware and Options Manuals [17] all of the resistivity measurements were done using the standard PPMS measurement technique, which uses a bridge circuit to drive an AC current through the sample, and measures the corresponding change in voltage across the votage leads. The current is driven at 7.5 Hz, and typically we set the current to 100 - 500 μA. The first stage in the measurement process is to maximize the signal to noise, but this turns out to be a balancing act. The first step is to set the minimum base temperature of $\sim$ 0.38 K. If the current is too high or the contact resistances are too high, there could be significant heating, which can prevent the ^{3}He system from reaching its minimum temperature. If the system is unable to get below $\sim$ 0.45 K, either the excitation current is too high, or one of the current contacts is too high. Sometimes a contact can fail during the cooling process. If the system successfully reaches 0.38 K, the current should be increased to as high a value as possible without heating the system. This can be achieved by writing a sequence which repeats a five or ten step resistance measurement at different currents. If the value of the resistance does not change with increasing current, the highest current should be used.

2.2.3 Measuring the Hall Voltage

By applying a magnetic field to the crystal and measuring the voltage perpendicular to the direction of the current, the carrier concentration can be determined via the Hall effect. Whenever there is both a current and a magnetic field present, charged particles will feel a force, $\vec{F}$=e$\vec{v} \times \vec{B}$, where e is the electron charge and $\vec{v}$ is the velocity of the electron. This will result in negatively and positively charged particles moving to opposite sides of the crystal perpendicular to the direction of the current, resulting in a potential difference called the Hall voltage. To measure the Hall voltage, the voltage leads need to be positioned to measure the voltage difference across the crystal perpendicular to the direction of the current (Fig. 2.6(b)). The charge carrier concentration is determined by

$$n = \frac{i}{(\Delta V/\Delta B)et}$$

where i is the current through the crystal, ΔV/ΔB is the slope of the linear Hall voltage versus applied magnetic field data, e is the charge of the electron, and t is the thickness of the crystal, determined by dividing the cross sectional area by the distance between the two Hall leads. The data are only linear if the carrier concentration is constant across the full field range at the chosen temperature. Because it is generally not possible to completely avoid any of the normal magnetoresistance mixing in with the perpendicular voltage component, the same number of data points must be taken with the same magnetic field range applied in the opposite direction so that the positive and negative field data can be averaged to filter out the parallel component of resistance and isolate the pure Hall voltage signal.

2.3 Measurement of Magnetic Properties

All of the magnetic measurements of Yb_3Pt_4 were done using a Quantum Design Magnetic Property Measurement System (MPMS) in temperatures from 1.8 K to 300 K, and in fields up to 7 T. To characterize the magnetic properties of Yb_3Pt_4, we measured the field and temperature dependence of the magnetization, and the

AC magnetic susceptibility. In this section, each type of measurement is described. We begin with a description of the crystal mounting procedure, which is the same for both measurement methods.

2.3.1 Crystal Mounting

For all standard magnetic measurements, the crystal is mounted in a drinking straw, and held in place by using a small amount of Apiezon N-grease to stick the crystal to the side of the straw, or the crystal can be placed in a straw segment, and the segment can then be placed in a full sized straw (Fig. 2.8). For crystals with a very small magnetization, like CaB_6, the diamagnetic signal of the straw will drown out the crystal signal. In cases such as these, a sample holder with as small a background as possible should be used. For our measurements of doped CaB_6, we used high purity quartz tubing, which has an extremely small, nearly zero magnetization. Once the crystal is mounted in the holder, the holder is attached to end of the sample rod and lowered into the MPMS inside the measurement coils, where it then must be precisely centered. A crystal rotation insert is also available for measuring the angular dependence of the magnetization or AC magnetic susceptibility (Fig. 2.8 (a),(b)). The crystal is glued onto the platform using GE varnish.

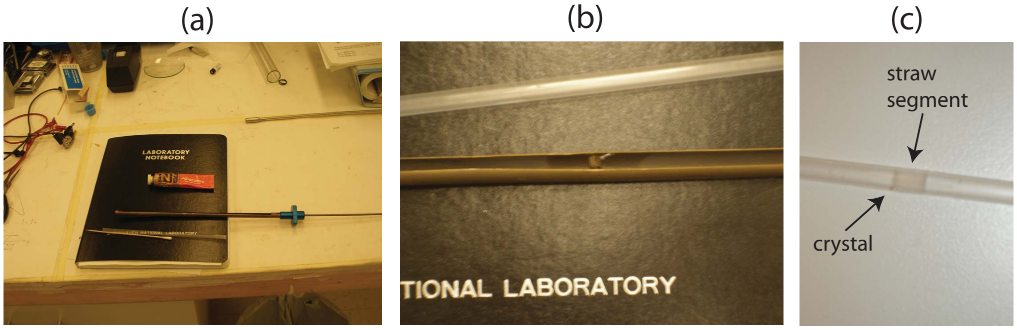

Figure 2.8: (a) A photograph of the end of the rotator insert for the MPMS next to a drinking straw, a tube of N-grease used to stick the crystal to the inside of the straw, and a wooden stick, used to apply the N-grease to the straw. (b) A close-up of the rotation insert, showing the platform on which the crystal gets mounted. (c) A close up of the middle of a drinking straw, where a straw segment containing a crystal has been placed.

2.3.2 Magnetization

As described in the Quantum Design MPMS manuals [24], the magnetization of a crystal is measured by moving it through a set of four very precisely wound superconducting pick-up coils (Fig. 2.9) [25], with the two outer coils counterwound relative to two inner coils, allowing the MPMS to almost completely filter out the large magnetic fields of the superconducting magnet to 0.1%. The signal detected by the pick-up coils is coupled to the Superconducting Quantum Interference Device (SQUID) via an isolation transformer. The crystal is moved through the coils by a stepper motor, which can be adusted to move the crystal from 0.1 cm to 12 cm, and take anywhere from 2 to 64 evenly spaced data points. We typically used scan lengths of either 4 or 6 cm, and 24, or 32 data points respectively. The first step is to center the crystal with respect to the pick-up coils. This is done by lowering the crystal to approximately the right position, and intiating a full lenth scan in a small applied field typically ranging from 100 to 1000 Oe. Normally, the biggest part of the signal corresponds to the crystal. The MPMS can then auto-adjust the starting position. Because the coil set has two coils in the center plus one above and one below, the total voltage induced will be twice as high for the center compared to the voltage induced by each of the outer coils. Fig. 2.10 is a schematic of the voltage versus position signal for a well centered crystal [25]. After taking a measurement, the actual signal is fit to the expected signal for a magnetic dipole moving through the SQUID pick-up coils, and the value of the magnetization is obtained from this fit.

For the special case of very small signals, such as the case with CaB_6, it is sometimes difficult to find a centering signal in the background noise. In this case, the starting position can be obtained, by first centering a test crytal that has a very

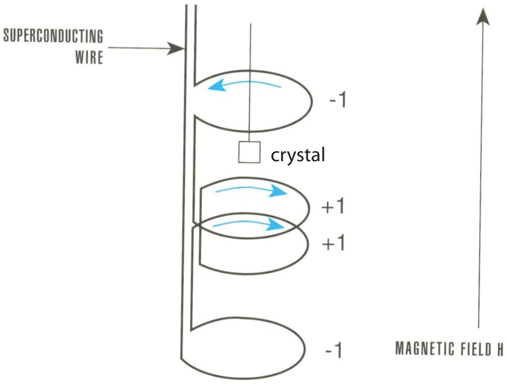

Figure 2.9: A schematic of the pickup coils used to detect the magnetic signal in the MPMS. The blue arrows show the direction of the current induced by the magnetic crystal. There are a total of four wire turns, with two of them counterwound with respect to the other two to cancel the current induces by the applied magnetic field (Figure from McElfresh, 1994 as referenced in the text).

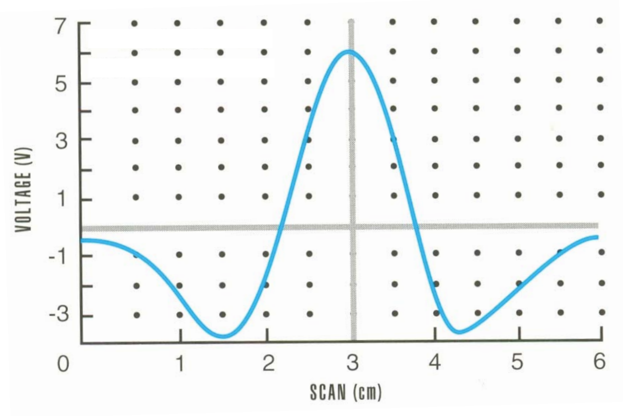

Figure 2.10: A schematic of the signal induced by a well centered crystal with a positive magnetization (Figure from McElfresh, 1994 as referenced in the text).

large signal, then replacing the test crystal with the actual small signalled crystal. If the crystal has a magnetic signal, but just too small to be seen from scan to scan, the MPMS should be set to average many scans. For a typical crystal with a healthy signal, we generally average 3 scans. In the case of CaB_6, which had a very weak signal, we averaged 27 scans. In addition, we used highly pure quartz tubes to minimize the background signal. Drinking straws have a small diamagnetic signal that can interfere when trying to measure very small magnetizations.

2.3.3 Arrott Plot Analysis

Arrott plot analysis is a method to determine the Curie temperature and critical exponents of a ferromagnetic phase transition based on measurements of the field dependence of the magnetization taken at different temperatures [26, 27, 28]. In this method, the magnetic field, H, is expanded in odd powers of the magnetization,

$$H = a_0 M + a_1 M^3 + a_2 M^5 + ...$$

Keeping just the first term in the expansion, H/M=a_0+a_1M^2. We then plot M^2 vs H/M and extrapolate the high field lines to the closest axis (Fig. 2.11). The Y-intercept of the isotherms gives us the extrapolated spontaneous magnetization squared, M^2, at each temperature below T$_C$. The X-intercept is the zero field inverse magnetic susceptibility, χ_0^{-1} at temperatures above T$_C$. T$_C$ can be roughly determined by observing which isotherm passes through the origin. A more careful analysis of the temperature dependences of both extrapolated values can then

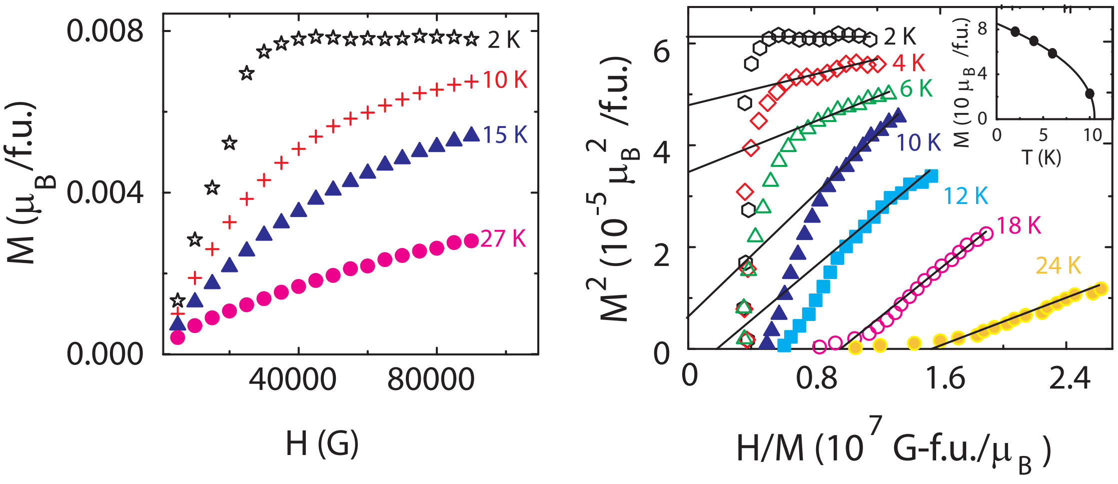

Figure 2.11: (a) The field dependence of the magnetization for a single crystal of Gd doped PtSb$_2$ at different temperatures as indicated. (b) Arrott plots for the same crystal indicating that T$_C$ ≈11 K. Inset: The temperature dependence of the extrapolated zero field spontaneous moment fit to a power law in reduced temperature, t=(T-T$_C$)/T$_C$, with M$\propto |t|^{-\beta}$, with β=0.37, and T$_C$=10.25 K.

be plotted as a function of the reduced temperature, t=(T-T_C)/T_C and standard graphical fitting routines can be use to determine both T_C and the values of the critical exponents. Fig. 2.12 shows the field dependence of the magnetization taken at different temperatures and the associated Arrott plot for single crystal of Gd doped $PtSb_2$. The inset shows the extrapolated spontaneous magnetization as a function of temperature with the best fit to M vs $(T_C\text{-}T)^{-\beta}$ giving the critical exponent for the spontaneous moment, β=0.37 and T_C=10.25 K.

2.3.4 AC Magnetic Susceptibility

The AC magnetic susceptibilty sytem and measurement technique is described in detail in the MPMS Options manual [24]. The preparation for an AC magnetic susceptibility measuremet is exactly the same as the preparation for the DC magnetization measurement. The crystal is mounted near the center of a drinking straw, a small magnetic field is applied, and the sample is centered in this DC field. However, for an AC susceptibility measurement, the crystal must be centered and measured using a 6 cm scan length. The MPMS has a measurement resolution of 5×10^{-12}Am^2 over a frequency range of 0.001-1000 Hz [24].

The AC susceptibility measures χ_{AC}=dM/dH=χ'+iχ''. A small AC field is applied to the crystal, and the resulting in phase, χ', and out of phase, χ'' signals are recorded. The MPMS first applies what Quantum Design calls drive nulling, during which the MPMS records and then nulls the response of the entire system to the drive frequency. subtracts unwanted background noise stemming from the AC current drive, the 60 Hz line, and other electronic noise. This takes place with the crystal centered in the bottom measurement coil. After the nulling process, the MPMS measures and averages a number of measurements as specified by the program and is fit to

$$M_b = A + Bt + M'cos(\omega t) + M''sin(\omega t),$$

[24] where M_b signifies that the measurement is taken in the bottom coil, A is the remaining DC offset, B is the linear drift in temperature or magnetic field, ω is the frequency of the AC drive signal, and M' and M'' are the in-phase and out-of-phase parts of the measurement signal. In the next measurement stage, the stepper motor moves the crystal up to the center of the two middle coils and performs a similar process, producing a second measurement, M_c. The results of the two measurements are $M_{b,c}$=Mf(b,c)+M_0, where M is actual crystal signal, M_0 is the remaining background signal left from an imperfect nulling process, and f(b,c) is the response function expected for an idealized dipole which varies with the position in the coils. The final χ' and χ'' signals are then given by

$$M = N\frac{M_c - M_b}{f(c) - f(b)}$$

where N is a normalization factor [24]. The operator then determines the signal averaging in the measurement program.

2.3.5 Detecting Superconductivity

Measurements of the temperature dependence of the AC magnetic susceptibility can detect the presence of superconductivity. When a material becomes superconducting, it expels magnetic flux [29]. This effect is known as the Meissner effect and is unique to superconductivity [29]. This expulsion of magnetic flux from a superconducting material is observed in measurements of the AC magnetic susceptibility. When the magnetic flux is expelled from the superconducting crystal, the magnetometer will measure a negative magnetic susceptibility, that when normalized for crystal volume will indicate that magnetic flux lines initially passing through the crystal in its normal state, have been completely expelled from the crystal in its superconducting state. For example, Fig. 2.12 is a plot of the temperature dependence of the AC magnetic susceptibility, normalized by volume, for a partially superconducting crystal of Yb-doped $PtSb_2$. When the flux has been completely expelled from the crystal, the normalized value will be $-1/4\pi$. If the result is some fraction of $-1/4\pi$, then the crystal is only partially superconducting, so if only half of the crystal volume is superconducting, the measurement will find a reading of $-1/8\pi$ in the superconducting state, so this measurement can also determine the amount of a superconducting impurity phase that may be present in a crystal. For the case of the Yb-doped crystal of $PtSb_2$ shown in the figure, χ'=-0.00045 in the superconducting state, indicating that less than 0.1% of the crystal is experiencing superconductivity. This extremely small volume superconducting region is from a small amount of superconducting impurity phase, PtSb, on the surface of the crystal and is not a bulk effect.

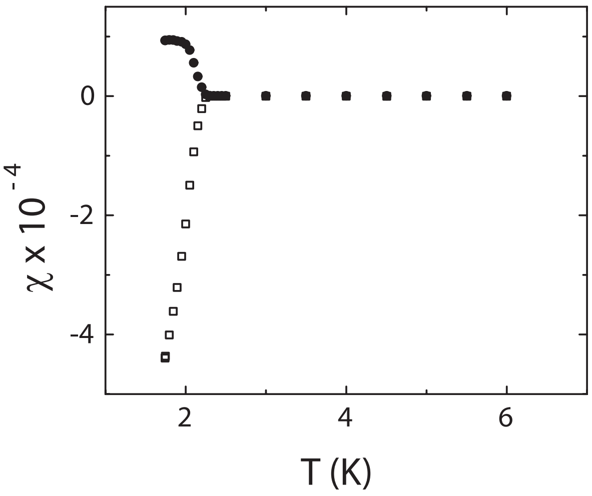

Figure 2.12: The temperature dependence of the volume normalized AC magnetic susceptibility, χ=χ' (hollow squares)+iχ''(filled circles) for a partially superconducting crystal of Yb-doped $PtSb_2$.

CHAPTER III

Growth of Single Crystals from Metallic flux

3.1 Introduction

The flux growth technique was used to grow all of the compounds that were studied in this thesis. Single crystals of CaB_6 were grown from Al flux, doped $PtSb_2$ from Sb flux, and Yb_3Pt_4 from Pb flux. An excellent overview of this technique has been written by Fisk and Remeika [30]. The growth of intermetallic crystals from metallic flux is analogous to the growth of sugar crystals from water. To grow large sugar crystals, water is heated up and regular polycrystalline sugar is dissolved in to it. A piece of string, or a wood stick is then placed into the solution to act as a nucleation site, or the crystals can grow on the walls of the container. The crystals slowly grow after the solution is removed from the heat source and allowed to cool. In this case the water acts as the flux from which the sugar crystals grow. For the case of CaB_6, molten Al is the flux, and for $PtSb_2$ and Yb_3Pt_4 the fluxes are molten Sb and Pb.

3.2 Advantages of Flux Growth

The flux growth method is an inexpensive and relatively easy way to grow crystals, requiring only a simple box furnace with a maximum temperature of 1500 C or less. Fisk and Remeika [30] present a good review of some of the advantages and disadvantages of the flux growth method. The materials are placed in a small Al_2O_3 or MgO crucible, which is then sealed in a quartz tube backfilled with Ar gas. Flux growth enables crystal growth at temperatures much lower than the actual melting points of the constituent metals, which improves crystal quality by minimizing strain and defects sometimes induced by a higher temperature environment. The formation of the crystals within the metallic flux also serves as an extremely clean environment, again leading to improved crystal quality. Flux growth enables the formation of crystals containing elements with very high vapor pressures, such as Yb, which are prone to evaporate in a simple solid state reaction. In the flux growth method, while some of the Yb will evaporate into the enclosed atmosphere, and deplete the mixture, most of it dissolves and remains in the metallic flux. Laboratories searching for new intermetallics to study can simply choose two or three metallic elements and experiment with the element ratios, and end up with a multitude of potentially interesting and useful single crystals. In the case of some element combinations, such as the Yb-Pt binaries, the existence of the many different phases can also be a disadvantage when attempting to isolate just one kind of crystal.

3.3 Disadvantages of Flux Growth

One of the main disadvantages of the flux growth method is the inconsistency of both crystal type and quality, with the quality of crystal varying from compound to compound and from batch to batch. The crystals are sometimes too small or delicate to measure. Also, the flux itself can become a part of the crystal, leading to even more potentially parasitic binary and ternary compounds. Often, during initial growth, and sometimes even after the best ratio of elements and oven settings have been determined, a single batch will contain several different crystal types, both binary and ternary. Especially during initial exploratory growths, it is difficult to predict exactly what crystals will grow. Since there is a limited number of metals suitable for use as a flux, sometimes it is not possible to grow certain compounds using this technique. The most significant problem with flux growth is the inconsistent purity of the crystals. They often contain flux inclusions, and worse, secondary phases contained within the sample, or on the sample surface, which ultimately can result in the detection of phase transitions that are not associated with the bulk single crystal. Sometimes, the crucible type contributes to this problem. We tended to use Al_2O_3 crucibles, and at sufficiently high temperatures, the Al will evaporated out of the container, and could contribute to unwanted impurity phases. SiO_2 is also available as a crucible material, but this could lead to impurity phases from the Si.

3.4 Determining the Ratio of Elements

After deciding which compound to grow, previously published binary phase diagrams are a good place to start [31], but they are often incomplete, and in the case of the Yb-Pt phases, we grew at least three previously unreported peritectic phases, Yb_5Pt_9, Yb_3Pt_5, and what we believe to be Yb_4Pt_7. We also grew the known ternary compound, Yb_2Pt_2Pb. The unintended growth of ternary compounds due to the incorporation of the element used for flux is not unusual. For example, the role of Pb must be considered when planning to grow Yb-Pt binary compounds and we always consider an Yb-Pt-Pb ternary phase diagram, which we interpolate by trial and error.

We first consider the simpler, binary phase diagram method twhen first attempting to grow a certain material. For example, if we want to grow Yb_3Pt_5 from Pb flux, we would first look on the Yb-Pt phase diagram (Fig. 3.1) [31], find the peritectic,

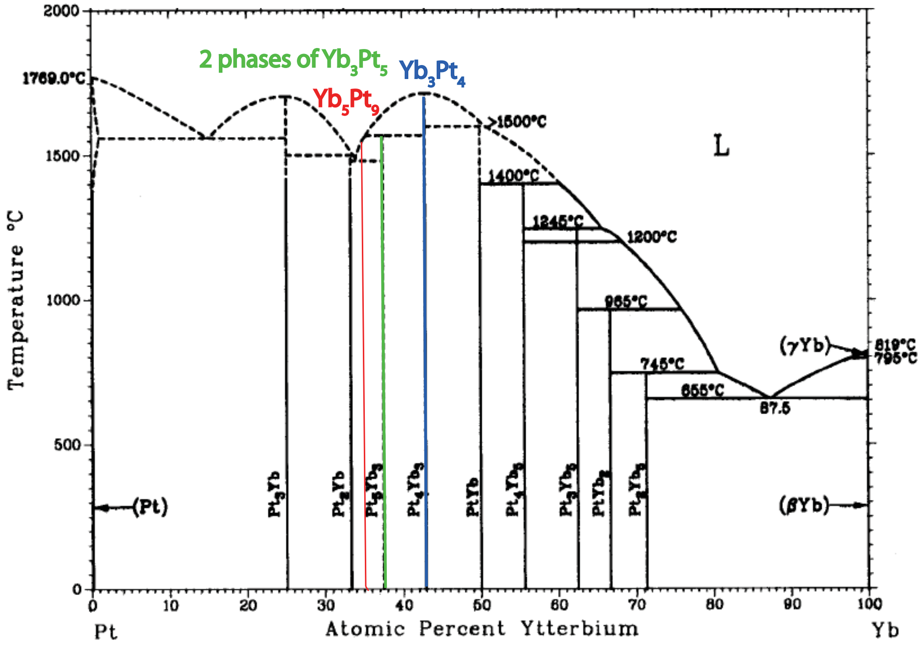

Figure 3.1: The Yb-Pt binary phase diagram (from Binary Alloy Phase Diagrams Handbook, 1990, as referenced in the text). These diagrams are often incomplete. The dashed lines representing the liquidus mean that the lines have not been experimentally established, only inferred. In addition, we found at least two new phases, Yb_5Pt_9, and a second phase of Yb_3Pt_5.

and determine the correct ratio of Yb-Pt that should be used to start near the top of the Yb_3Pt_5 liquidus then cool to the bottom of the Yb_3Pt_5 liquidus to maximize the amount of Yb_3Pt_5 grown. As a general rule, we would make sure that the total mix of Yb, Pt and Pb consisted mostly of Pb (95-98%) to make sure that the Yb and Pt could dissolve into it. Thus for this simple method, we would begin with roughly 95% Pb, making sure that the mass of Pb was enough to mostly fill the crucible. The remaining 5% of the mix would consist of Yb and Pt in a molar 3:5 ratio.

Sometimes this simple method works well, but as described above, normally the element used as flux must also be considered and sometimes will form ternary compounds with the elements meant for binary compounds. This occurs for Yb and Pt in a Pb flux. Yb_2Pt_2Pb grows easily over a wide range of element ratios. The growth of single crystals of Yb_3Pt_4 from Pb flux turns out to be very sensitive to the exact ratio of Yb:Pt:Pb used. This situation is further complicated by the very high vapor pressure of Yb, which results in the evaporation of some percentage in the growth melt, which affects the element ratios present in the melt, resulting in a decrease in Yb relative to the other elements.

The best way to find and maximize the element ratios and temperature profile of the growth is by trial and error, growing crystals using slightly different ratios of Yb:Pt:Pb in certain regions in an Yb-Pt-Pb digram, which is produced by creating a three axis plot representing all possible ratios of Yb:Pt:Pb (Fig. 3.2). Each side of the digram in Fig. 3.2 represents one of the three binary phase diagrams, Yb-Pt, Pt-Pb, and Yb-Pb. The result is an unknown three-dimensional liquidus surface, that is determined experimentally by trial and error. Thus, we end up with points, or regions on the diagram that correspond to the growth of different crystals. For example, we found two places that produce single crystals of Yb_3Pt_4. The first region produces small blocky crystals (Fig. 3.3(a)), while the other region produces long, thin, bar-like crystals (Fig. 3.3(b)).

3.5 Growth Procedure

Because the top of the mix will sometimes spill as it is sealed in a quartz tube, the Yb and Pt should be placed on the bottom of the crucible so that any spillage is in the form of Pb, and will not affect the ratio significantly. Once the mix is in the crucible the crucible is placed in a flat bottomed quartz tube, and the whole thing is evacuated by a regular roughing pump and backfilled with Ar gas several times to prevent oxidation. Using a propane or hydrogen torch the quartz tube is then sealed under vacuum. The material plus quartz tube is then placed in a larger crucible, which is placed in a box furnace and baked. The maximum temperature

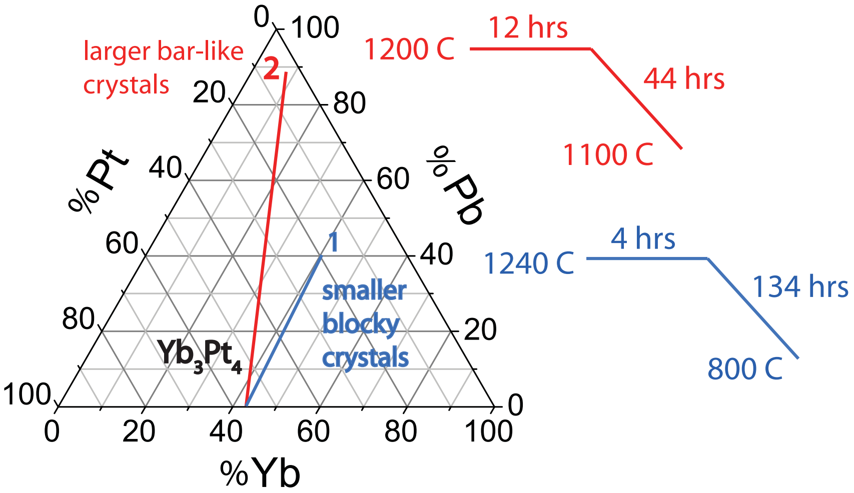

Figure 3.2: A three axis diagram representing all the possible combinations of Yb, Pt and Pb. After a careful exploration via multiple trial and error, we found two regions that produced Yb_3Pt_4. In region 1, a ratio of Yb:Pt:Pb=40:20:40 produces smaller blocky crystals ~1 mg, using a growth temperature profile (blue) of 12 hours at 1240°C followed by a 44 hour cool-down to 1100°C. In region 2, with a ratio Yb:Pt:Pb=9:3.5:87.5, we find much bigger bar-like crystals up to ~70 mg, using a growth temperature profile (red) of 4 hours at 1240°C followed by a 134 hour cool-down to 800°C.

can not be set over 1200 C, because this is the melting temperature for quartz. As a general rule, the furnace is sent to 1190 C, and allowed to sit for 4 hours to make sure that all the material is melted and dissolved in the crucible. The whole mix is then cooled gradually. A reasonable rate to start with is 7 C per hour until the bottom of the peritectic liquidus is reached, and the desired crystals have grown. Maximizing crystal quality and size requires maximizing the cooling rate and determining the best temperature to remove the melt normally requires a number of trials. Since the crystals are now sitting in molten Pb, the Pb needs to be removed. Placed above the the mixture in crucible is some quartz wool, or a tantalum strainer to allow the Pb to pour out, but stopping any crystals. The whole thing is then placed upside down in a centrifuge, which is then spun, forcing the molten Pb out of the crucible, leaving

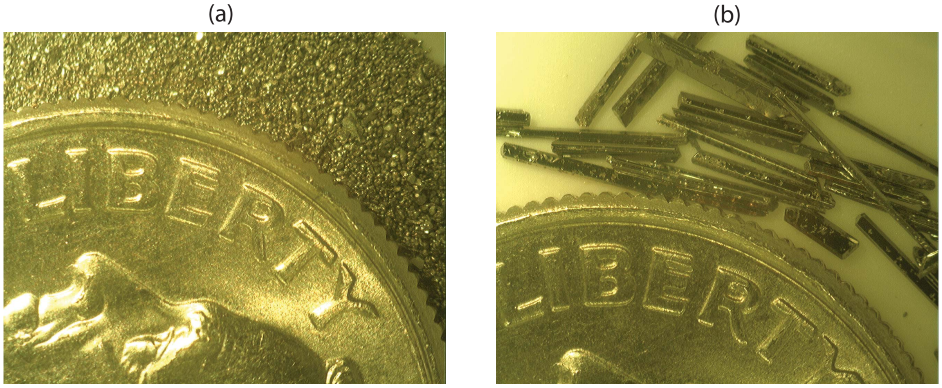

Figure 3.3: (a) A picture of single crystals of Yb_3Pt_4 grown using the temperature profile and element ratios in region 1 (blue, Fig. 3.2), next to a dime. (b) A picture of single crystals of Yb_3Pt_4 grown using the temperature profile and element ratios in region 2 (red, Fig. 3.2), next to a dime.

the crystals. When the whole thing has cooled to room temperature, it is placed in some paper and smashed open with a hammer, or crushed open with a vise to reveal the crystals.

3.6 Crystal Isolation

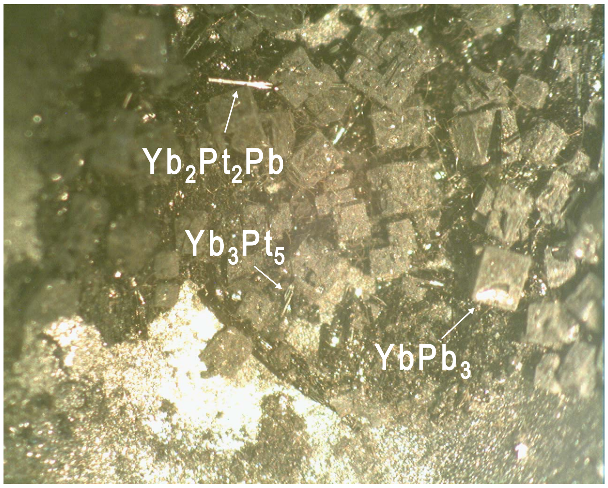

Figure 3.4: A photograph of the side of a crucible on which at least three different phases grew, as indicated on the photograph.

The first step after a growth is crystal isolation and identification. The contents of the crucible are visually inspected and any obvious crystals are separated out. This step is sometimes complicated by the presence of multiple phases. For the case of the Yb-Pt-Pb melt for example, before determining exactly how to grow each phase, we often grew multiple phases (Fig. 3.4). The next step is to remove any remaining metallic flux on the crystal surface. One of the easier ways to do this is to use an etchant that will remove the flux, while leaving the desired crystal intact. For the case of removing Pb flux from Yb-Pt binaries, a 50/50 by volume mixture of acetic acid and H_2O_2 removes residual Pb flux from the crystal surface, but does not affect any of the Yb-Pt binaries. However, this method can not be used for Yb_2Pt_2Pb, because the etchant will dissolve the crystal. In this case, each crystal needs to have each of its sides polished manually using emory cloth and ethanol or some other lubricant.

3.7 Crystal Identification

For previously measured compounds, identification can be quite simple. A matching powder X-ray pattern, or a matching distinct anomaly in the specific heat can verify the desired crystal identity. We simply collect crystals and crush them into a powder with an agate mortar and pestle, place the powder on a slide, which is then mounted in the X-ray diffractometer. Fig. 3.5 shows the known X-ray powder pattern for Yb_3Pt_4 taken at the National Synchrotron Light Source (NSLS) at Brookhaven National Laboratory, on a batch of crystals grown in our laboratory. If there is not enough material for a powder pattern, single crystal X-ray diffraction can be used to verify the crystal structure. In the first successful growth of Yb_3Pt_4, the crystals were splinter-like with typical dimensions of $0.2\times0.2\times1$ mm^3. Before we figured out how to grow it, we had only a few single crystals, not enough for powder X-ray measurements, so we chipped a small fragment off of one of the crystals, and determined the crystal structure using single crystal X-ray diffraction. Below we discuss the importance of determining the correct stoichiometry of the compound before making any conclusions based on X-ray diffraction measurements.

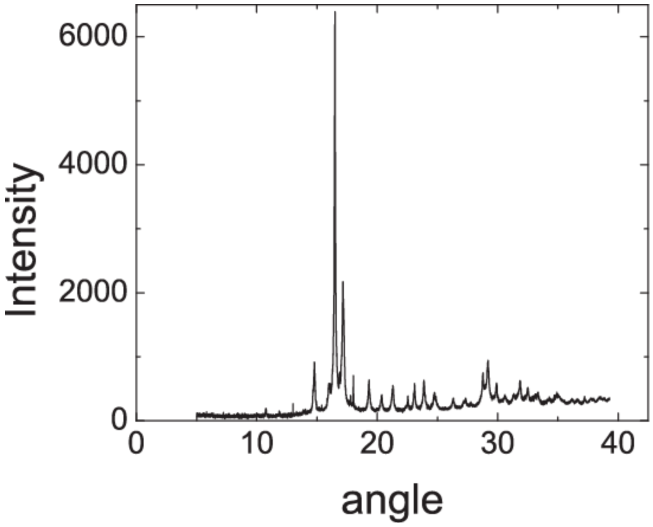

Figure 3.5: The X-ray powder pattern for Yb_3Pt_4 (Figure courtesy of P. Stephens).

It can be a difficult challenge to accurately identify new or unknown compounds. The first technique to try is powder X-ray diffraction. In the early stages of our exploration of the Yb-Pt binary compounds, we grew at least three unknown phases, including Yb_5Pt_9. We realized we had a new Yb-Pt binary compound after comparing the powder pattern to known powder patterns of other Yb-Pt binaries with similar stoichiometries [32] (Fig. 3.6). It is also difficult to differentiate between Pt and Pb during X-ray analysis. Normally, an initial guess of the stoichiometry is determined by microprobe analysis. The importance of first determining the rough stoichiometry by microprobe analysis, which gives the stoichiometry of the crystal within 2%, is best illustrated by a false conclusion on one of the initially unknown compounds that we grew and measured, Yb_2Pt_2Pb. After obtaining the crystals structure from single crystal X-ray diffraction measurements, we concluded that the compound was Yb_2Pt_3. This error occurred, because Pb and Pt are difficult to distinguish.

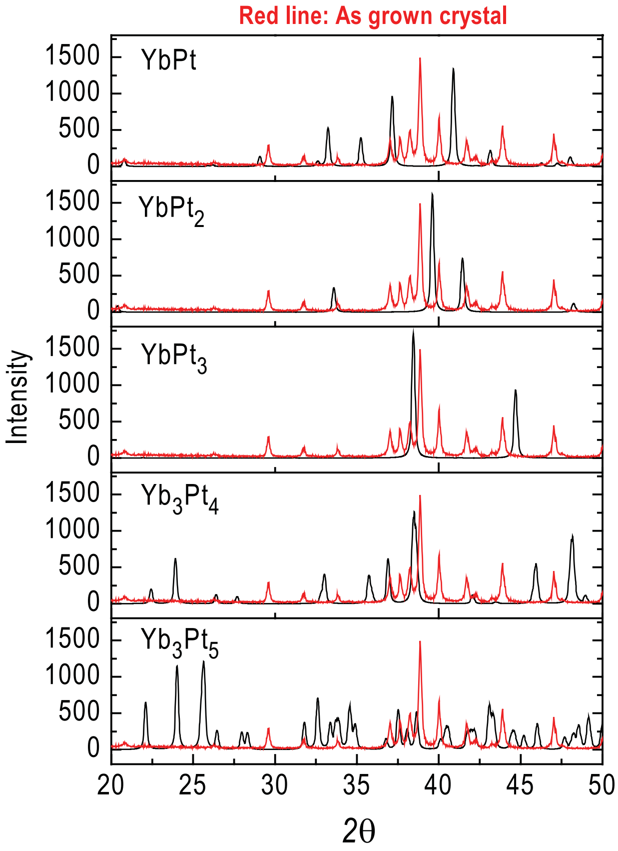

Figure 3.6: The powder diffraction patterns for several Yb-Pt binary compounds compared with the powder pattern obtained from Yb_5Pt_9, which at the time was unknown. The powder patterns of the known structures were obtained from the Cambridge Structural Database, as referenced in the text (Figure courtesy of M. S. Kim).

For the case of Yb_3Pt_4, microprobe analysis was carried out using a Cameca SX100 system, containing Yb and Pt standards used to accurately normalize the measurements. The atomic ratio of Yb:Pt was found to be uniform across the surface with a systematic error of ∼2%. Single crystal X-ray diffraction measurements revised the approximate atomic Yb:Pt ratios to 3:4, finding a rhombohedral P42/mnm crystal structure for Yb_3Pt_4, as described in Chapter 6.

Measurement of the heat capacity is an excellent way to identify compounds with distinct phase transtions that produce large anomalies in the specific heat. Yb_3Pt_4 can be identified by its unique anomaly at 2.4 K. It can also be identified by its unique temperature and field dependent AC magnetic susceptibility, its resistivity, and by its magnetoresistance. With all the tools of compound identification described above, the insidious problem of minority impurity phases can still sneak into an experiment. In the next section, we discuss the very tedious, but essential methods to identify impurity phases. As discussed in Chapters 4 and 5, ignoring this step can lead to spurious results from impurity phases falsely attributed to the bulk crystal.

3.8 Finding Impurity Phases

One of the disadvantages of the flux growth method is the possibility of growing minority impurity phases on the crystal surface, or within the crystal. The best way to find impurity phases on the crystal surface is by microprobe analysis. A careful scan of the entire surface of each crystal is advisable. The impurity phases will show up as lighter or darker shades on the elemental intensity measurement images. Electron microscopy and electron microprobe analysis were used extensively to determine the rough stoichiometry of newly grown crystals and to look for impurity phases on the crystal surface. The EMAL lab at the University of Michigan is equipped with a Hitachi model S3200N scanning electron microscope (SEM), and a more accurate Cameca SX100 Microprobe Analyzer. A microprobe analyzer is just a highly accurate SEM. Electron microscopy works by bombarding the crystal surface with an external beam of electrons, which penetrate the crystal surface, knocking bound electrons from the inner atomic core, resulting in the release of X-rays from the atoms near the crystal surface. Detectors count the X-rays and using the relative intensity of X-rays of different energies corresponding to the different elements, the stoichiometry can be determined. The microprobe renders a more accurate result in two different ways. First, unlike the SEM which uses only one detector, the microprobe has several more sensitive detectors that can be separately tuned to detect only certain X-ray frequencies. Second, the microprobe always measures actual elemental standards and re-calibrates the machine before each measurement. The SEM relies only on a data base, and has no actual standards. It is extremely important to make sure that the crystal has as flat a surface as possible with respect to the incoming electron beam. An uneven, or angled surface will result in an inaccurate stoichiometry result, because the detectors will not measure all the emitted X-rays.

Other methods to find impurity phases are measurements of the heat capacity, magnetization, and AC magnetic susceptibility. These methods work only if the impurity phase has a phase transition detectable by one of these methods. The easiest to find are superconducting impurity phases. For a BCS superconductor for example, it is easy to determine what percentage of the crystal is superconducting using the famous result, $(C_S-C_N)/C_N=1.43$, where C_S is the value of the electronic heat capacity at T_C of the superconducting state and C_N is the value of the electronic heat capacity at T_C of the normal state. A value smaller than 1.43 indicates that the crystal is only partially superconducting, indicating the possible presence of an impurity phase. Another way to determine the percentage of the crystal that is superconducting is via the AC magnetic susceptibility, using the fact that a completely superconducting crystal will completely expel magnetic flux. A partially superconducting crystal will only partially expel magnetic flux. The way to find Pb, or In flux inclusions is to look for partial superconducting transitions near 7 K and 3.5 K. A magnetic transition might also be easy to attribute to an impurity phase. For a ferromagnetic impurity phase, the saturation magnetization and the Hund's rule moment will be smaller than expected for an Yb, or Ce based bulk crystal if it originates with a minority impurity phase.

CHAPTER IV

The Search For a Wigner Lattice in Electron Doped CaB_6

4.1 Observation of High T_C Ferromagnetism in Doped CaB_6

In a ferromagnet, the Curie temperature (T_C) is determined by the competition between magnetic interactions and thermal energy. The reported observation of ferromagnetism in $Ca_{1-x}La_xB_6$ (0.001<x<0.05) with Curie temperatures of 600 - 900 K [1, 33] was completely unexpected. An extremely high T_C indicates very strong ferromagnetic interactions, but this seems unlikely in $Ca_{1-x}La_xB_6$, because all the elements that make up this compound are non-magnetic. Table 3.1 lists T_C and the saturation moments (M_S) for a number of known high T_C ferromagnets and for two single crystals of $Ca_{1-x}La_xB_6$. As indicated in the table, the maximum T_C for $Ca_{1-x}La_xB_6$ occurs for x=0.01, and the maximum M_S occurs for x=0.005. Relative

Table 4.1: The Curie temperature and saturation moment of two single crystals of $Ca_{1-x}La_xB_6$ compared with some other known ferromagnets.

Compound	T_C(K)	M_S (μ_B/f.u.)	Ref.
Fe	1043	2.22	[34]
Co	1388	1.72	[34]
Ni	627	0.606	[34]
Gd	292	7.63	[34]
Dy	88	10.2	[34]
MnBi	630	3.52	[34]
$Ca_{0.995}La_{0.005}B_6$	600	0.07	[1, 33]
$Ca_{0.99}La_{0.01}B_6$	900	0.03	[1, 33]

to other ferromagnets, CaB_6 has a high T_C, but the very low saturation moment shows that we have a low magnetic moment density. Because there are no magnetic elements present in the single crystals, the source of the magnetism must originate with the magnetic moments of the itinerant electrons. For the crystal with the highest saturation moment, the electron concentration, inferred based on the amount of La doped into the single crystals, indicates that the average spacing between electrons is 25 $\mathring{A}$. This large distance between moments makes the extremely high T_C all the more remarkable. An obvious question follows: what then is the source of this ferromagnetism? We designed our experiments to consider two possible origins: the formation of a Wigner lattice and contamination from high T_C magnetic impurities. Initially, based on the initial published report, the possibility of contamination seems unlikely, because D. P. Young et al measured a number of other La doped alkaline earth hexaborides, and added the tetravalent dopant Th to CaB_6 as well [1, 33]. $Sr_{1-x}La_xB_6$, and $Ba_{1-x}La_xB_6$ also displayed similar magnetic behavior, and each showed a maximum magnetic moment at x=0.005, in complete agreement with the results for $Ca_{1-x}La_xB_6$. To further dispel the contamination argument, CaB_6 was also doped with Th. La is trivalent and is therefore an electron donor when it replaces divalent Ca. Th is tetravalent and thus contributes two electrons per atom. As expected, $Ca_{1-x}Th_xB_6$ displayed a maximum moment at x=0.0025 [1, 33], suggesting that the magnetism is primarily a function of the electron density, which is consistent with a ferromagnetic Wigner lattice. However, mass spectrometry measurements showed that Fe is present in some ferromagnetic crystals of CaB_6 in amounts that are roughly proportional to M_S [35], suggesting that the ferromagnetism originates with Fe impurities. In another study, electron dispersive x-ray spectroscopy and Auger electron spectroscopy measurements have shown that Fe contamination is present several microns into single crystals of $Ca_{1-x}Th_xB_6$ [36], again suggesting that the origin of the ferromagnetism is Fe based impurities and not the formation of a Wigner lattice. The goal of our experiments on doped CaB_6 is to determine whether the origin of the ferromagnetism is intrinsic as in the case of the Wigner lattice, or extrinsic, coming from Fe contamination. We begin in the next section with a theoretical description of the Wigner lattice. In the following section, we describe the known properties of undoped and doped crystals of CaB_6. With the theoretical background and description of the basic properties of CaB_6 in place, we then present our transport and magnetization measurements, and microprobe analysis results of the surface of a ferromagnetic crystal and ultimately our conclusions about the origins of the ferromagnetism.

4.1.1 The Wigner Lattice

In the 1930s, E. Wigner showed that an electron gas in a positively charged background crystallizes into a lattice at sufficiently low electron density [37, 3]. In a 1987 publication [3], Tsidil'kovskii presents an excellent summary of the early theoretical and experimental developments of the Wigner lattice. For the electrons to become localized in a lattice, the potential energy per electron needs to be larger than the thermal kinetic energy. As the electron density decreases, the potential energy increases, and the kinetic energy decreases, resulting in a critical electron density, n_C, where the kinetic and potential energies are equal and a lattice forms. The first experimental observation of a Wigner lattice occurred in 1979 when electrons were floated on the surface of liquid helium and a two dimensional Wigner lattice formed [2, 3]. A three dimensional Wigner lattice has never been experimentally confirmed. n_C is easily calculated in the free electron gas model, where the kinetic energy, E_K=3/5E_F=50.1 eV/r_S^2, and the potential energy, E_P=e^2/r_0, where E_F is the Fermi energy for the free electron gas, r_0 is the mean distance between electrons, and r_S is the same distance, but in units of Bohr radii, with r_S=r_0/a_0, and $r_0=(3/4\pi n)^{1/3}$ [3, 5]. In other words, E_K is dominant for small r_S (large n), and E_P is dominant for large r_S (small n). Using this simple picture, the results of the calculation for n_C, and its associated critical spacing, r_C are r_C=1.1, and $n_C^{1/3}a_0$=0.56. In our measurements, we found a typical value of our samples of n=5×10^{18} cm^{-3}, which corresponds to $n_C^{1/3}a_0$=0.009, which places all of our crystals well within the Wigner lattice regime. Later theoretical efforts added various interactions including exchange and correlation energy [1], while another included lattice vibrations, and the fact that critical displacement from the lattice sites results in melting [3]. More accurate descriptions followed. In 1980, Ceperley used a quantum Monte Carlo method to derive what are considered the most accurate estimates of r_C and n_C [38]. The result predicts that between the free electron gas and the crystalline state, there is an intemediate spin polarized fluid state, which is either paramagnetic or ferromagnetic. If the spin polarized fluid is paramagnetic, $r_C=75 \pm 5$ and $n_C^{1/3}a_0=0.0083 \pm 0.0005$. If the spin fluid is ferromagnetic, $r_C=100 \pm 20$ and $n_C^{1/3}a_0=0.0062 \pm 0.0013$. Ortiz also used quantum Monte Carlo methods to identify the same phase boundaries, obtaining somewhat different values of $r_C=65 \pm 10$ and $n_C^{1/3}a_0$=0.0099 for the crystallization of the electron gas, and $25 \pm 5 < r_C < 35 \pm 5$ for the spin-polarized fluid [39]. In this case, the fluid gradually changes from paramagnetic at low values of r_C to ferromagnetic at high values of r_C. One of our primary experimental goals is to test the accuracy of these results, and to seek evidence for other phases which might be present as functions of electron concentration, temperature and magnetic field. Before describing the experimental details, we first describe the properties of undoped CaB_6 in the following section.

4.1.2 Properties of Undoped CaB_6

Single crystals of CaB_6 are grown from Al flux using an excess of Ca relative to stoichiometric amounts of Ca and B [40]. Undoped CaB_6 has a simple cubic crystal structure (no. 221), with a lattice constant, a=4.15 $\mathring{A}$ comprised of Ca atoms and B_6 octahedra [41, 42]. The band structure of the hexaborides is determined by the hybridization of the B atoms [43]. For divalent cations, including Ca, Sr and Ba, the Fermi level lies in the gap between the third and fourth lowest lying bands, resulting in an insulating material. For trivalent cations, there is partial filling of the fourth band leading to metallic behavior. LaB_6 for example is metallic and superconducting [44]. Results from these early tightbinding calculations were confirmed by more sophisticated GW calculations [45], which predict that CaB_6 is a direct gap semiconductor. There were, however some conflicting reports about whether undoped CaB_6 is a semiconductor or a semimetal and if it was a semiconductor, how big a gap it had. A 1997 theoretical prediction based on LDA calculations predicted that CaB_6 should be a semimetal [46] and Denlinger et al pointed out that even within the more reliable GW calculations, the size of the predicted gap varies from 0.3 to 0.8 eV [47], emphasizing the need for further experimental measurements of the gap of an undoped CaB_6 single crystal. In 2002, Denlinger et al, using angle resolved photoemission spectroscopy (ARPES) measurements confirmed that stoichiometric CaB_6 is a semiconductor with a direct 1.15 eV gap [47]. As expected for a semiconductor, the magnetic susceptibility is negative and temperature independent (diamagnetic) [48]. Also consistent with semiconducting behavior, CaB_6 has a thermally activated resistance [40], which increases with decreasing temperature as $\rho(\mathrm{T})=\rho_0 \mathrm{e}^{-\Delta/kT}$, where Δ is the energy gap between the carriers and the lowest lying itinerant state. From measurements of the temperature dependence of ρ, Δ=0.4 eV [40], which is substan-

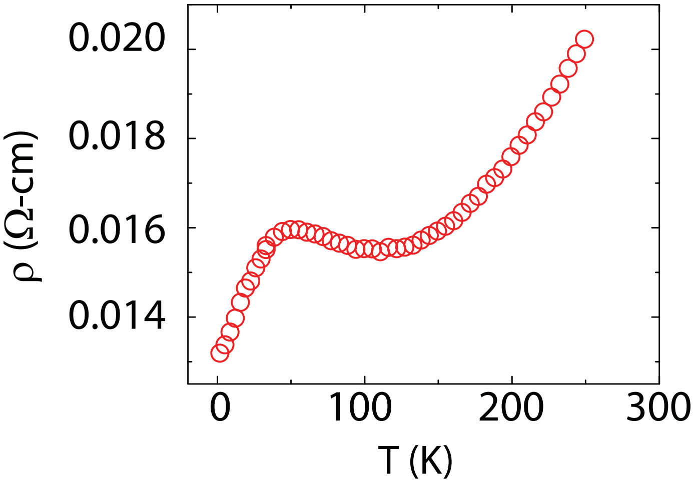

Figure 4.1: The temperature dependence of the resistivity for a CaB_6 crystal with n=1.2×10^{19} cm^{-3}. The resistivity has regions where it increases with decreasing temperature and regions where it decreases with decreasing temperature, illustrating that this crystal is close to the metal-insulator transition.

tially smaller than the value obtained from ARPES measurements. We argue that this suggests the possibility that the defect states play a role in the transport.

Doping CaB_6 with La, leads to some of the divalent Ca ions being replaced by trivalent La ions which adds electrons to the system, ultimately driving it metallic, resulting in the creation of a Fermi surface, which has been confirmed by de Haas van Alphen measurements [49]. Measurements of the temperature dependence of the resistivity also shows a change from the thermally activated resistance of a semiconductor to that of a metal, with ρ increasing with increasing temperature [1]. This insulator to metal transition occurs near the doping levels at which the ferromagnetism is observed. Crystals with this range of n typically show behavior that is neither purely semiconducting nor purely metallic, often with one or more broad maxima in the temperature dependence of the resistivity (Fig. 4.1). In the next section, we present our experimental results, beginning with Hall effect measurements to determine the carrier concentration of 14 doped CaB_6 crystals.

4.1.3 Hall Voltage Measurements

In order to determine if there is some relationship between the electron concentration, n, and the Curie temperature, T_C, we first collected multiple crystals with a range of electron concentrations and measured both the Hall effect and the field dependence of the magnetization to determine the saturation magnetizaton, M_S. We performed Hall voltage measurements on 14 crystals of CaB_6 that were not intentionally doped and found a range of electron concentrations ranging from 10^{17} to 10^{20} cm^{-3}. Hall effect measurements were conducted at temperatures ranging from 0.4 K to 100 K using a 9 T superconducting magnet, and also at the National High Magnetic Field Laboratory at Los Alamos using a 50 T medium pulse length magnet. The Hall voltage was linear in field over the entire field range (Fig. 4.2(a)) with a slope indicating that electrons are the dominant carriers. Figure 4.2(b) is a plot of the temperature dependence of the electron concentration for six of the crystals, showing that the electron concentration is temperature independent in all cases. In Figure 4.3, we show that we have obtained crystals that represent a significantly larger range of electron concentrations than those of previous studies [1, 50, 51],

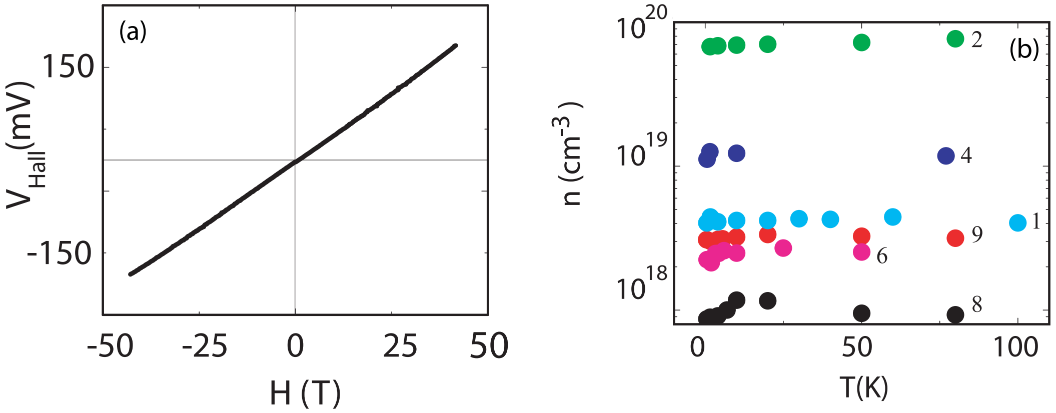

Figure 4.2: (a) The field dependence of the Hall voltage taken in fields approaching 50 T at 0.5 K. (b) The temperature dependence of the electron concentration for six of our crystals, showing that n is largely temeperature independent.

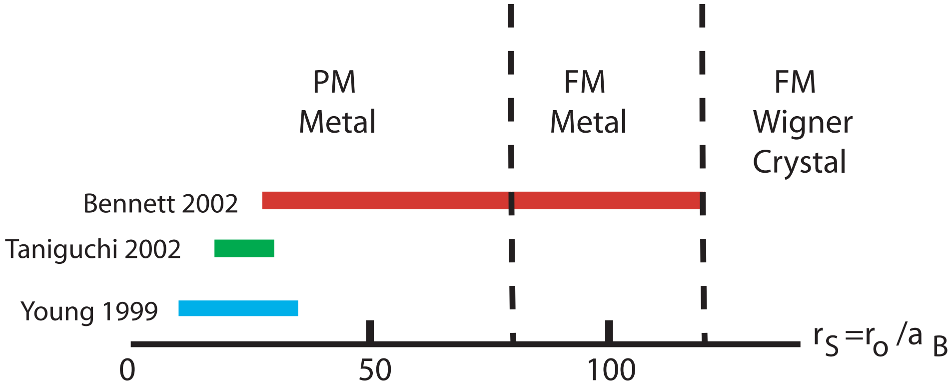

Figure 4.3: A schematic showing the range of electron concentrations studied by Young et al (from Young, 1999, as referenced in the text), Taniguchi et al (from Taniguchi, 2002, as referenced in the text), and in this work. The dashed lines represent the different states of the electrons as a function of electron concentration in units of r_S according to Ceperleys theoretical predictions.

and we compare each range to the theoretical predictions of various Wigner lattice states according to the predictions of Ceperley [38]. After establishing the carrier concentration for all fourteen of the crystals, we measured the corresponding field dependence of the magnetization as described in the next section.

4.1.4 Magnetization Measurements

We measured the field dependence of the magnetization at 250 K, and at fields as high as 7 T for all fourteen of the crystals. All of the crystals were found to be ferromagnetic with the characteristic non-linear field dependence of the magnetization, and coercive fields ranging from 40 to 200 Oe. Figure 4.4 is a plot of the field dependence of the magnetization for four of the crystals with different electron concentrations. We then fit each M(H) curve to a Langevin function to obtain M_S, which we then plotted as a function of n in Figure 4.5(a) (black circles) and compared the data with those of Young et al (red circles) [1]. We find no systematic relation between M_S and n. In Figure 4.5(b), we re-plot M_S in units of μ_B per electron (μ_B/e) and find unphysically large values in the low n region, with M_S reaching as high as 35 μ_B/e. We conclude that it is unlikely that the magnetization can be correlated to

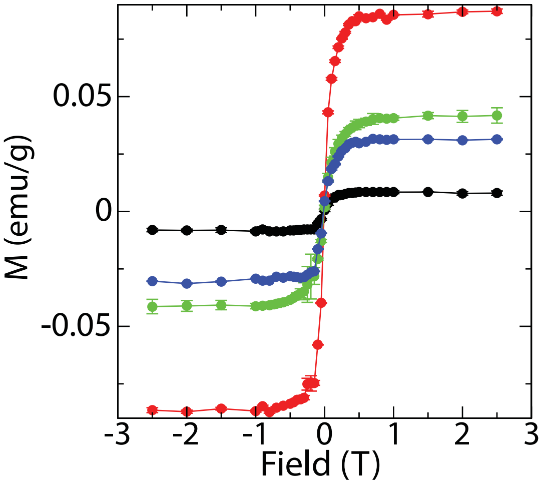

Figure 4.4: A plot of the field dependence of the magnetization for four different crystals of CaB_6 with electron concentrations of 9×10^{17} cm^{-3} (black circles), 2.5×10^{18} cm^{-3} (red circles), 3×10^{18} cm^{-3} (green circles) and 5×10^{19} cm^{-3} (blue circles).

the variations in n as might be expected for instabilities of an electron gas. The next set of experiments was designed to test whether the ferromagnetism is of extrinsic origin. The first experiment, described in the next section, uses microprobe analysis to search the crystal surfaces for ferromagnetic contaminant phases.

4.1.5 Surface Analysis

We used electron microprobe analysis using a Cameca Microprobe Analyzer at the University of Michigan Electron Beam Microanalysis laboratory (EMAL) to scan the surface of several of our crystals to look for ferromagnetic contaminant phases. Analysis of the surface of single crystals of CaB_6 found Fe and Ni impurities on the surface for all of the crystals that we examined. As an example, we will describe the results of our surface analysis on two of our crystals, one with smooth, flat surfaces with visible terracing and the other with a rough surface. Both show significant amounts of Fe and Ni on the surface. Figure 4.6 is an electron backscattering image of one of the corners of a single crystal, illustrating the smooth surfaces and terracing. The consistent brightness over the whole surface indicates a homogeneous

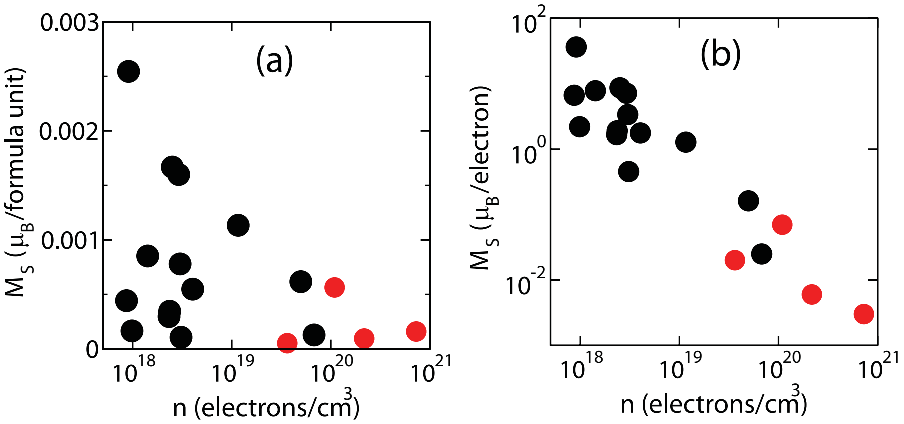

Figure 4.5: (a) A plot of the saturation magnetization as a function of the electron concentrations for all of the crystals measured in this study (black circles) and the same plot for the data of Young et al (red circles) (from Young, 1999, as referenced in the text).(b) The same data as in (a), but with M_S plotted in units of μ_B per electron to illustrate the unphysical values obtained by assuming that the ferromagnetism is intrinsic.

composition, but at the edges of the growth steps, we observe a brighter shade, indicating the presence of contamination consisting of elements with a higher atomic number relative to CaB_6. To identify the nature of this contamination, we measured electron microprobe maps for Ca, Fe and Ni and compared them with the electron backscattering image (Fig. 4.7). Figure 4.7(b) shows that the Ca concentration is spatially uniform over the crystal surface. The Fe map (Fig. 4.7(c)) shows that the bright regions on the step edges first seen in the electron backscattering image contain Fe. The Ni map (Fig. 4.7(d)) shows that the step edges also contain small amounts of Ni. These contaminant phases on the step edges are likely to be close to pure Fe and Ni, because no other elements show an enhancement in this region, although we can't rule out the presence of Fe-B binary phases, which might also be present in small amounts. Figure 4.8(a) is a backscattering image for a crystal with a rough surface over a 50 μm square region on its surface, showing bright contaminant regions, that Fe and Ni maps reveal are primarily Fe and Ni (Fig. 4.8(c),(d)). The significant amounts of Fe and Ni contamination result in the shadowing evident in the Ca map

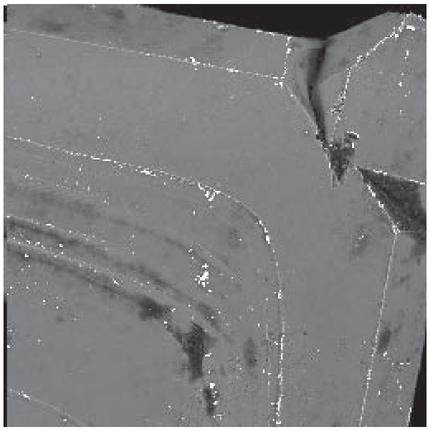

Figure 4.6: An electron backscattering image for a corner of a crystal with a smooth surface. The presence of elements with a higher atomic number relative to CaB_6 is evident on the step edges.

(Fig. 4.8(b)), which otherwise shows a spatially uniform Ca concentration. It should be noted that the crystals were previously etched, and it is in principle possible for crystals to become contaminated from the acid in the etch. It is unlikely that Fe and Ni were introduced during acid etching, given that the Fe and Ni contamination extends well into the crystal surface. It is more likely that the contamination took place before or during crystal growth from contaminated batches of the component elements, Ca, and B, or the Al flux, which may have become contaminated from unclean growth apparatus such as the crucibles or the quartzware. In the next section, we describe the etching experiment that we conducted to show this.

4.1.6 Etching Experiments

For our final experiment, we used 50% aqua regia solution to etch the Fe and Ni contaminated surfaces of a crystal of CaB_6 with $n=1.2\times10^{19}$ cm^{-3}. An edge finder determined that the etch rate is 300 ±100 $\mathring{A}$ per second. We measured the field dependence of the magnetization before and after a 6000 $\mathring{A}$ and 12000 $\mathring{A}$ etch (Fig. 4.9(a)). The first etch reduced M_S by 47%, but the second etch did not further reduce M_S, showing that the Fe and Ni contamination extends roughly 6000 $\mathring{A}$ into

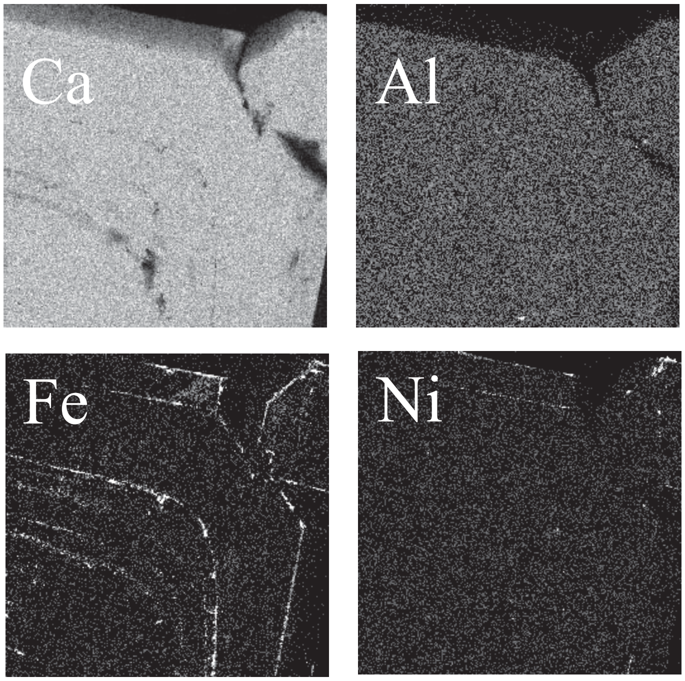

Figure 4.7: (a)The Ca microprobe map, showing a uniform distribution of Ca over the crystal surface. (b) The Al microprobe map showing that there is no residual Al flux on the surface of the crystal (c) The Fe microprobe map showing the presence of Fe along the step edges. (d) The Ni microprobe map showing the presence of Ni along the step edges, but in smaller amounts compared with the Fe.

the crystal surface. In Fig. 4.9(b), we show that the resistivity of the crystal does not change as a result of the etch, indicating that it is representative of the bulk crystal and not affected by the surface impurities. In Figure 4.10(a) we show the electron backscattering image, and microprobe Fe (Fig. 4.10(b)) and Ni (Fig. 4.10(c)) maps of the same 50 μm square region of the same unetched crystal shown in Fig. 4.7, but with sharper contrast to show that the Fe and Ni are found in different areas of the same region, trapped in surface features. The typical Fe and Ni contaminant particle size is of the order of microns. The next etching test was performed on two other smooth surfaced single crystals by comparing electron microprobe images of the surfaces of two single crystals of CaB_6 before and after etching. Fig. 4.10 shows Fe microprobe maps of these two crystals before etching (d,g), then after a 30 second etch (e,h), and then after a second 60 second etch (f,i). It is evident from the images

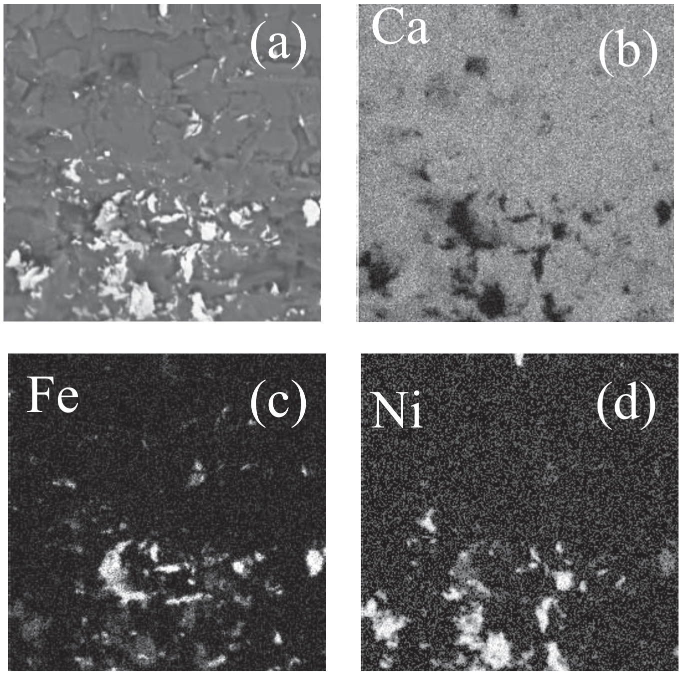

Figure 4.8: (a) The electron backscattering image for a rough surfaced crystal. The bright shades indicate the contamination. (b) The Ca map, showing a uniform distribution of Ca over the crystal surface, except where the contamination covers the surface, where the shadowing occurs. (C) The Fe microprobe map showing the presence of significant amounts of Fe on the crystal surface. (d) The Ni microprobe map showing significant amounts of Ni on the crystal surface.

that the Fe contamination extends fairly deeply into the crystal surface and that the acid etching gradually removes the contamination from the edges of the steps, but the Fe is especially persistent in these locations, and it would require a 10,000 to 20,000 $\mathring{A}$ etch to completely remove the Fe. As summarized in the following final section, we conclude that the ferromagnetism in CaB_6 originates with Fe and Ni impurities found at step edges of the single crystals at depths to roughly 10,000 $\mathring{A}$.

4.2 Summary

We sought to determine whether the high T_C ferromagnetism in doped CaB_6 originates with the formation of a Wigner lattice [51]. For a ferromagnetic Wigner lattice, we would have expected to find a systematic relation between n, T_C and M_S. Also, below T_C, we would expect to find an insulating state, which would result in a

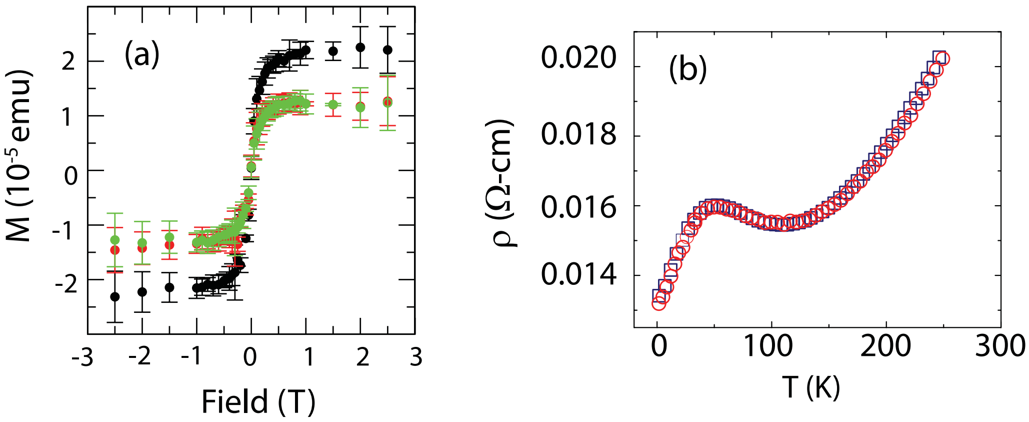

Figure 4.9: (a) The field dependence of the magnetization for a CaB_6 crystal before etching (black circles), and after 6000 $\mathring{A}$ were removed by an acid etch (red circles) and after 12000 $\mathring{A}$ were removed by the etch (green circles). (b) The temperature dependence of the resisitivity before etching (red circles) and after a 6000 $\mathring{A}$ etch (blue squares).

sharp increase in the resistivity at T_C. By measuring the Hall voltage, and the field dependence of the magnetization, we determined that M_S was not related to n. We also found no correlation between the measurement of the temperature dependence of the resistance and the presence of ferromagnetism. None of our ferromagnetic crystals showed the thermally activated resistivity expected for an insulating state. Finding it unlikely that the ferromagnetism resulted from the formation of a Wigner lattice, we searched the crystal surfaces for magnetic impurities. Electron microprobe analysis found Fe and Ni contaminants on the crystal surfaces, and roughly 10,000 $\mathring{A}$ into the bulk. Acid etching experiments found that the Fe and Ni impurities could be removed by etching with a 50% solution of aqua regia. We measured the field dependence of the magnetization for a crystal before and after etching and found that M_S substantially decreased after etching. We are left to conclude that the ferromagnetism in CaB_6 does not come from the formation of a Wigner lattice or any other intrinsic origin, but is of extrinsic origin, resulting from Fe and Ni based contaminant phases.

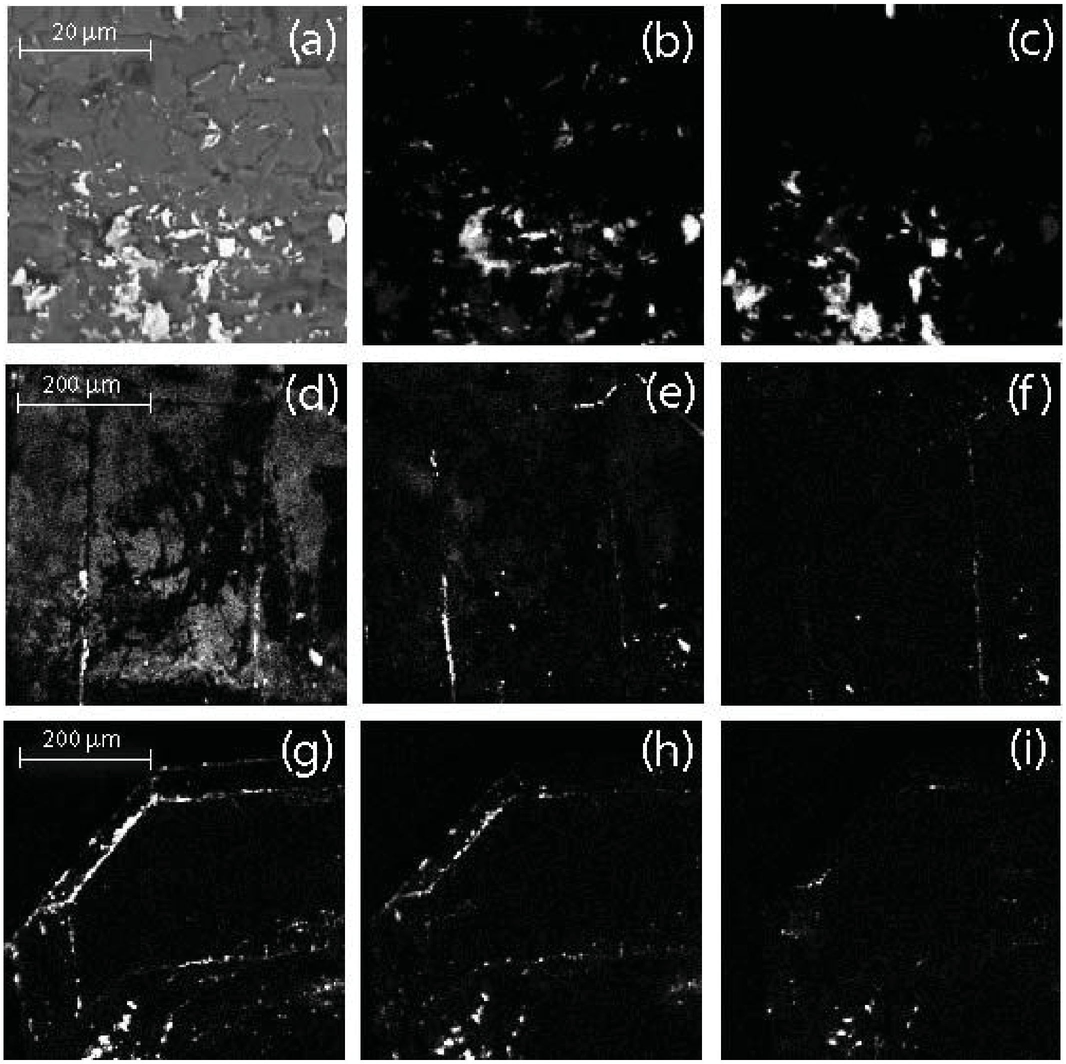

Figure 4.10: (a) An electron backscattering image of a 50 μm square region on the surface of a single crystal of CaB_6 before etching. (b) An electron microprobe map for Fe of the same region of the same single crystal as in (a). (c) An electron microprobe map for Ni of the same region of the same single crystal as in (a). (d) An electron microprobe map for Fe for a single crystal of CaB_6 before etching. (e) An electron microprobe map for Fe for the same region of the same as crystal as in (c) after a 30 second acid etch. (f) An electron microprobe map for Fe for the same region of the same crystal as in (c) after a second 60 second etch. (g) An electron microprobe map for Fe for another single crystal of CaB_6 before etching. (h) An electron microprobe map for Fe for the same crystal as in (g) after a 30 second acid etch. (i) An electron microprobe map for Fe for the same crystal as in (g) after a second 60 second etch.

CHAPTER V

The Origins of Superconductivity and Ferromagnetism in Rare Earth Doped $PtSb_2$

5.1 Ferromagnetism in Dilute Magnetic Semiconductors

The simplest magnetic interaction that can lead to ferromagnetism in a lattice of localized spins with no itinerant carriers present is dipolar. When dipolar interactions dominate, we expect $T_C \propto N$ [5], but as N decreases, the distance between local moments will increase and the dipole-dipole interactions will become weaker. However, with a sufficient density of intinerant carriers present, Ruderman-Kittel-Kasuya-Yosida (RKKY) interactions will occur and the localized moments will interact strongly despite the large distances between them. In the RKKY interaction, the magnetization density of the conduction electrons is spatially modulated around the localized magnetic moments and the spatially oscillating spin density of the conduction electrons conveys the spin information between even very distantly spaced local moments, allowing them to interact indirectly. Depending on the distance between the local moments and on the value of k_F, they will order either ferromagnetically, or antiferromagnetically, with the ordering temperature for a given N, $T_{C,N} \propto n^2$ [6, 7, 8]. The purpose of our experiments is to better understand how the interactions which lead to ferromagnetism evolve from dipolar when no itinerant carriers are present to RKKY when many itinerant carriers are present. In this chapter we focus on the region in Figure 1.1 located horizontally to the right of the N=0 Wigner lattice region (red region) in the low to moderate n and N region (green region) represented by the dilute magnetic semiconductors (DMS), a type of semiconductor made by substituting magnetic ions in place of some percentage of the regular cations of the host semiconductor. DMS are ideal for this study, because in principle we can control both n and N by doping with suitable magnetic and/or non-magnetic elements. We begin our study by looking for a consistent general relation among T_C, n and N in previously measured ferromagnetic DMS. Figure 5.1 is a plot of the n and N dependence of T_C for the previously measured DMS, Ga(Mn)As [52], PbSnMnTe [53], and Gd and La doped EuS [54]. For (III,Mn)V compounds with high n, a modified mean field theory, predicting $T_C \propto Nm^*n^{1/3}$, where m* is the effective mass [55], agrees with experimentally obtained values for the Curie temperature. As shown in Figure 5.1, for most compounds there are regions on the n-N plane where $T_C(n)$ is sub-linear, suggesting that it is the closest fit of the three predictions to the known

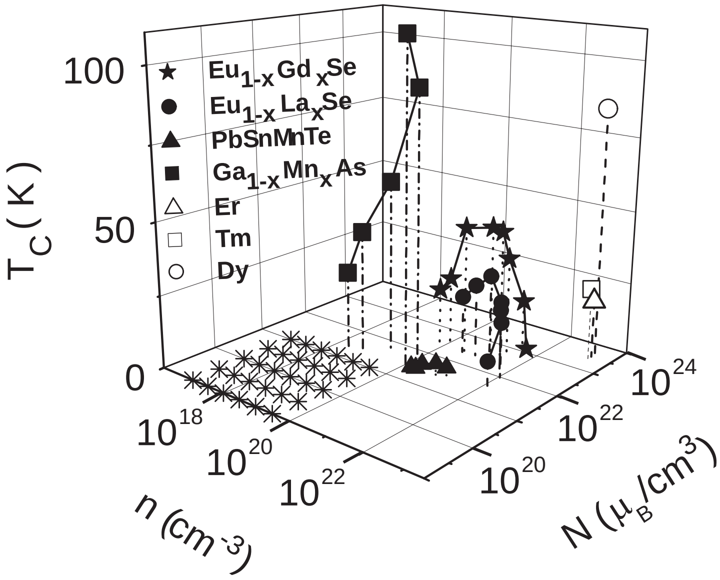

Figure 5.1: Curie temperatures for the DMS described in the introduction and the three rare earth metals, Er, Tm and Dy plotted as a function of the carrier concentration, n, and the magnetic moment density, N. The patterned region is an unexplored sector on the n-N plane potentially accessible using rare earth doped $PtSb_2$.

DMS data. For comparison, we also include the ferromagnetic rare earth metals Er, Tm and Dy, located in the high n and N area of this region where RKKY interactions dominate. By the flux growth process described in Chapter 2, we grew a new DMS from Sb flux, rare-earth doped $PtSb_2$ with values of n and N that allow us to access the unexplored region of the n-N plane marked by asterisks in Figure 5.1. We plan to determine the n and N dependence of T_C in this unexplored region and together with the known results displayed in Figure 5.1 try to find a common relation among T_C, n and N. Before presenting our experimental results of rare earth doped crystals, we first summarize the known properties of undoped $PtSb_2$, which have been thoroughly characterized in previous experiments [56, 57, 58, 59, 60, 61, 62, 63]. The following two sections then describe our transport, heat capacity and AC magnetic susceptibility measurements of single crystals of rare earth doped $PtSb_2$ doped with Ce, Eu, Gd, La and Yb, which find superconductivity in some of the Yb and La doped crystals and ferromagnetism in some of the Ce and Gd doped crystals. In each of these sections, we also present electron microprobe anlaysis results which indicate that secondary impurity phases are present on the surface of most of our single crystals. We find that these impurity phases and not the bulk properties of the crystals are the source of the superconductivity and ferromagnetism. In the final experimental section, we present heat capacity measurements of five of our crystals that have been etched to remove the surface impurity phases, and show that some of the rare earth elements are successfully doped into the bulk, changing the electronic properties, but not enough magnetic moments are doped into the system to access the regime of most interest.

5.2 Properties of Undoped $PtSb_2$

In this section, we describe the properties of undoped $PtSb_2$ determined by previous theoretical calculations and experiments. Powder X-ray diffraction measurements find that crystals of $PtSb_2$ form in the pyrite structure (cP12) with a lattice constant of 0.644 nm [59]. Tight binding band structure calculations predict that $PtSb_2$ has an indirect energy gap of 0.8 eV [60]. Experimentally, an indirect gap of 0.11 eV has been determined by measurements of the temperature dependence of the resistivity and by infrared absorption measurements [56, 61]. The transport properties have been measured for a number of single crystals and they vary from crystal to crystal, because most crystals deviate from ideal stoichiometry [58]. Only a few single crystals show semiconducting behavior, with ρ increasing with decreasing temperature, while most show behavior with both semiconducting and metallic aspects [58]. For example, some of the crystals have a maximum in $\rho(T)$ between 150 and 400 K, while in other crystals, $\rho(T)$ saturates at low temperature [58]. Previous Hall effect measurements show that the carriers can be electrons resulting from Sb vacancies, or holes, resulting from Pt vacancies or Sb interstitials. n ranges from 10^{17} to 10^{20} cm^{-3} [58, 57], which is exactly the range of n that we wish to study, making $PtSb_2$ an ideal material, provided that it is also possible to vary N by doping with magnetic elements. We attempt to control N by doping $PtSb_2$ with the rare earth elements La, Eu, Ce, Gd and Yb. The rare earth elements are ideal for this study of systems of local moments and itinerant carriers, because of the localized nature of the magnetic moments of the f electrons. We grew all of our single crystals of rare earth doped $PtSb_2$ from Sb flux and performed extensive measurements of their transport, magnetic and compositional properties. We present our transport,

Table 5.1: The electron concentrations calculated from Hall voltage measurements for 7 rare-earth doped single crystals of $PtSb_2$.

Crystal	n (cm^{-3})
Yb1	1.8×10^{19}
Ce1	5×10^{19}
Gd1	4×10^{19}
Gd2	2×10^{19}
Gd3	2×10^{19}
Eu	3×10^{17}
La1	5.7×10^{18}
La2	7.5×10^{18}

heat capacity, magnetization, AC magnetic susceptibility and electron microprobe measurements of these crystals in the following section.

5.3 Experimental Results

In this section, we present the resistivity, specific heat, magnetization and AC magnetic susceptibility as well as electron microprobe measurements of our rare earth doped $PtSb_2$ crystals. The first step in our experiment is to verify that our single crystals were within the desired carrier concentration range of 10^{16} to 10^{20} cm^{-3}. Using our PPMS, we measured the Hall effect in all of our single crystals at temperatures ranging from 1.8 K to 300 K and in fields up to 9 T. In all cases, the field dependence of the Hall voltage was linear and the carriers were electrons, suggesting that they originate from the rare earth dopants or from Sb interstitials. From the Hall voltage data, we calculate electron concentrations ranging from 10^{17} to 10^{20} cm^{-3} for all of our crystals. We find that the electron concentration is largely temperature independent for all of the measured single crystals. Table 4.1 is a Table of electron concentrations for some of our single crystals. We observe superconductivity in three Yb doped crystals and one of the La doped crystals and ferromagnetism in some but not all of the Ce and Gd doped single crystals. Based on our heat capacity measurements, we find that although most of the rare earth elements are not absorbed into the bulk, a small percentage of them do end up in the bulk, resulting in modified electronic properties. We then use electron microprobe analysis to find the secondary impurity phases responsible for the superconductivity and ferromagnetism. In the next two sections, we present the experimental results for the superconducting crystals followed by the experimental results for the ferromagnetic crystals. We then present the bulk properties of the crystals and conclude with a summary of our results.

5.3.1 Superconductivity in single crystals of Yb and La doped $PtSb_2$

The first signs of superconductivity appeared in measurements of the temperature dependence of the resistivity in one La doped crystal and three Yb doped crystals. We performed this measurement on all of our doped single crystals from 1.8 K to 300 K and found a variety of results. Figure 5.2 is a plot of the temperature dependence of the resistivity for three different crystals to illustrate some of the different temperature dependences. The Eu doped crystal shows the thermally activated resistance expected in a semiconductor. The Yb doped crystal shows a decrease in resistivity with decreasing temperature characteristic of metal, followed by a sudden drop in resisitivity at the lowest temperatures, indicating a transition to a superconducting state. The La doped crystal shows a temperature dependence that has characteristics of both a semiconductor and a metal, with the resistivity initially increasing with decreasing temperature, but then after reaching a maximum near 150 K, decreasing with decreasing temperature. Like the Yb doped crystal, it also shows a sudden drop in the resistivity at the lowest temperatures, indicating a transition to a superconducting state. To further characterize the superconducting state, we measured the temperature dependence of the resistivity in different magnetic fields. The transition temperature decreases with increasing magnetic field and the temperature range over which the transition takes place broadens, also consistent with a superconducting transition with a critical field, $H_C \sim 800$ G. However, the resistivity does not drop all the way to zero, indicating that the crystal is only partially superconducting, suggesting that perhaps an impurity phase is the source of the superconductivity. We found partial superconducting transitions for three crystals of Yb doped $PtSb_2$ and one La doped crystal, with values of T_C ranging from 1.6 K to 2.2 K and associated H_C ranging from 500 to 1200 G (Fig. 5.3). We compared our results to the results for the $YbSb_2$ crystal [64] to determine whether the superconductivity might originate with small impurity regions of $YbSb_2$ unintentionally introduced into our crystals during growth. It is clearly observed in Figure 5.3 that H_C for the rare earth doped $PtSb_2$ crystals is five to ten times higher than H_C for $YbSb_2$. We conclude that the source of the superconductivity in our crystals does not lie fully with $YbSb_2$.

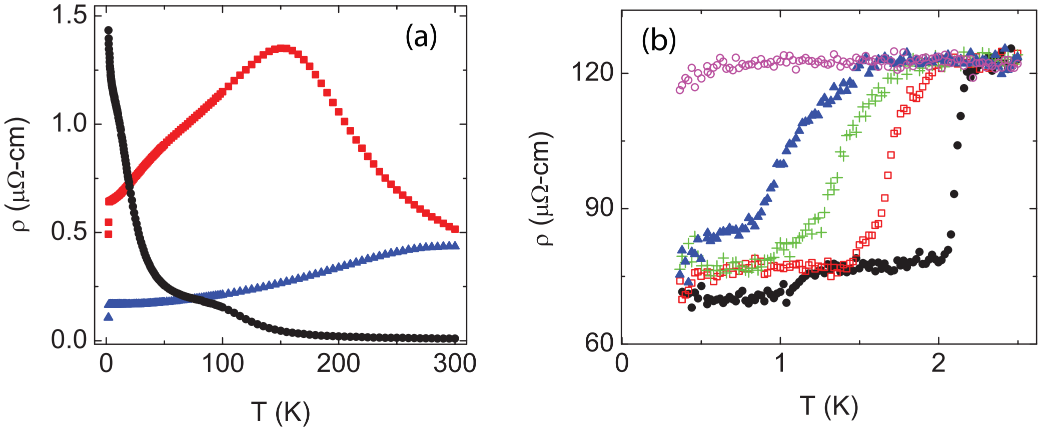

Figure 5.2: (a) The temperature dependence of the resistivity for a Eu doped crystal (black circles), a La doped crystal (red squares) and an Yb doped crystal (blue triangles). (b) The temperature dependence of the resistivity of a single crystal of Yb doped $PtSb_2$ in zero field (black circles), 200 G (red squares), 350 G (green crosses), 500 G (blue triangles), and 1000 G (magenta circles) at temperatures up to 2.5 K.

To determine what percentage of each crystal is superconducting, we measured the temperature dependence of the specific heat of the superconducting single crystal

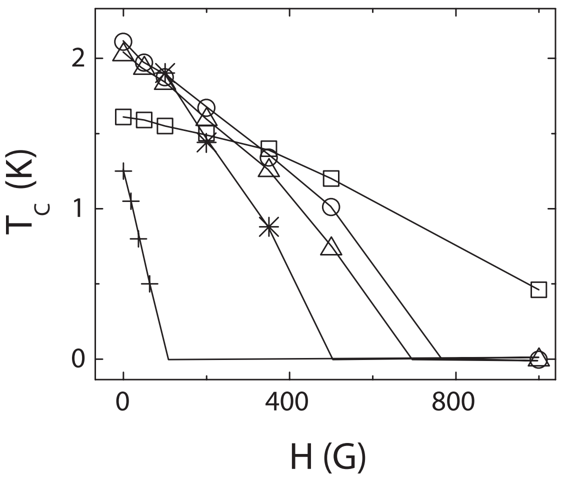

Figure 5.3: The field dependence of the superconducting transition temperature, T_C, for three single crystals of Yb doped $PtSb_2$ (circles, triangles, squares), and one crystal of La doped $PtSb_2$ (asterisks) and the data from one crystal of $YbSb_2$, previously measured by Yamaguchi et al, referenced in the text.

of La doped $PtSb_2$ and the temperature dependence of the AC magnetic susceptibility of four single crystals of Yb doped $PtSb_2$ and two single crystals of La doped $PtSb_2$. The temperature dependence of the specific heat of the La doped crystal was measured from 0.38 to 2.6 K (Fig. 5.4), but there is no observable anomaly near 2 K (Fig. 5.4 inset), where the transition in the resistivity is observed. To estimate the percentage of the crystal that is superconducting, we assume that the superconducting transition is well described by the Bardeen-Cooper-Schrieffer (BCS) theory, where $(C_S\text{-}C_N)/C_N=1.43$, where C_S is the electronic specific heat at T_C of the superconducting state, and C_N is the the electronic specific heat at T_C of the normal state [29]. Based on the sensitivity of our specific heat measurement, no more than 1% of the crystal is superconducting. To corroborate the result from the specific heat measurement we also measured the zero field AC magnetic susceptibility of four single crystals of Yb doped $PtSb_2$, and two single crystals of La doped $PtSb_2$. The AC susceptibility, $\chi=\chi'+i\chi''$ was measured from 1.8 K to 6 K at a frequency of 113 Hz

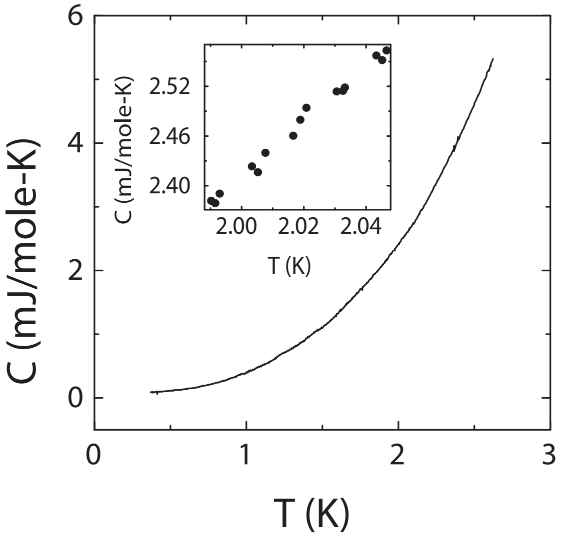

Figure 5.4: The temperature dependence of the specific heat of a single crystal of La doped $PtSb_2$. Inset: The specific heat near 2 K shows no noticeable anomaly.

and with an amplitude of 4.17 Oe. Figure 5.5(a) shows the temperature dependence of the in phase and out of phase AC magnetic susceptibility for one of the partially superconducting Yb doped crystals. χ' drops sharply near 2 K, indicating that, as expected at the superconducting transition, magnetic flux is being expelled from the crystal. The peak in χ'' indicates that at base temperature, 1.8 K, χ' is very close to its final temperature independent value. The base temperature value is χ'=-0.00045 is less than 0.1% of the expected value of -1/4π for a fully superconducting crystal experiencing the Meissner effect, indicating that less than 0.1% of the Yb doped crystal is superconducting.

To determine whether or not the superconductivity is associated with an impurity phase located on the crystal surface, we measured the AC magnetic susceptibility of one of the partially superconducting La doped crystals before and after a 15 minute etch in heated aqua regia (Fig. 5.5(b)), which dissolved roughly half of the original crystal. Before the etch there is clearly a Meissner effect indicating the presence of superconductivity, but after the etch, there is no longer any Meissner effect, indicating that the source of the superconductivity is likely a surface phase occupying a relatively small part of the crystal volume.

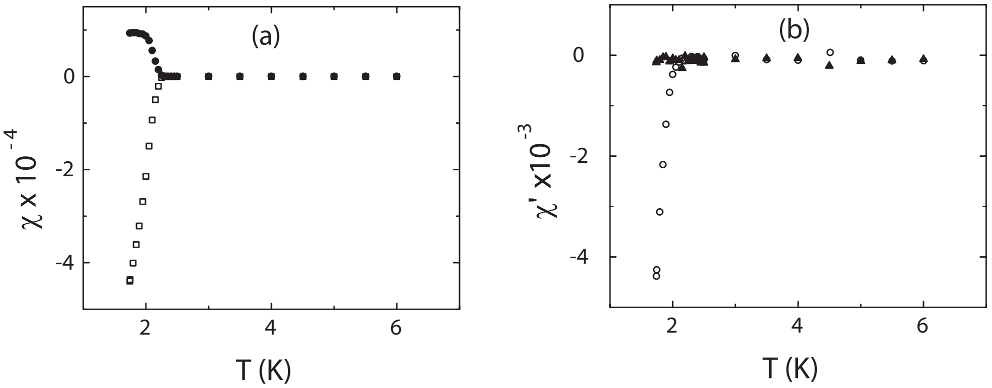

Figure 5.5: (a) The temperature dependence of the in-phase, χ' (squares) and out-of-phase, χ'' (circles) components of the AC magnetic susceptibility for a single crystal of partially superoconducting Yb doped $PtSb_2$. The peak in χ'' indicates that the value of χ' at the 1.8 K base temperature is close to its minimum temperature independent value. (b) The in-phase AC magnetic susceptibility of a single crystal of partially superconducting La doped $PtSb_2$ before (circles) and after (triangles) a 15 minute etch in heated aqua regia. The superconductivity is no longer present after the etch.

To find and identify the superconducting impurity phase on the crystal surface, we used electron microprobe analysis to measure a single crystal of Yb doped $PtSb_2$. Figure 5.6(a) is an electron backscattering image of a single crystal of partially superconducting Yb doped $PtSb_2$. The surface shows some flat regions and also areas with a more irregular topography. The two regions of different shading show that there are at least two different compositions, with the brighter shaded region having a composition with a larger average atomic number relative to the darker shaded region. To determine the composition, we measured EDS maps for Pt (Fig. 5.6(b)), Sb (Fig. 5.6(c)), and Yb (Fig. 5.6(d)). The Pt map shows that the two different phases seen in the electron back scattering image each contain Pt, where the brighter shaded area (Fig. 5.6(b) left) has a higher concentration of Pt relative to the darker shaded

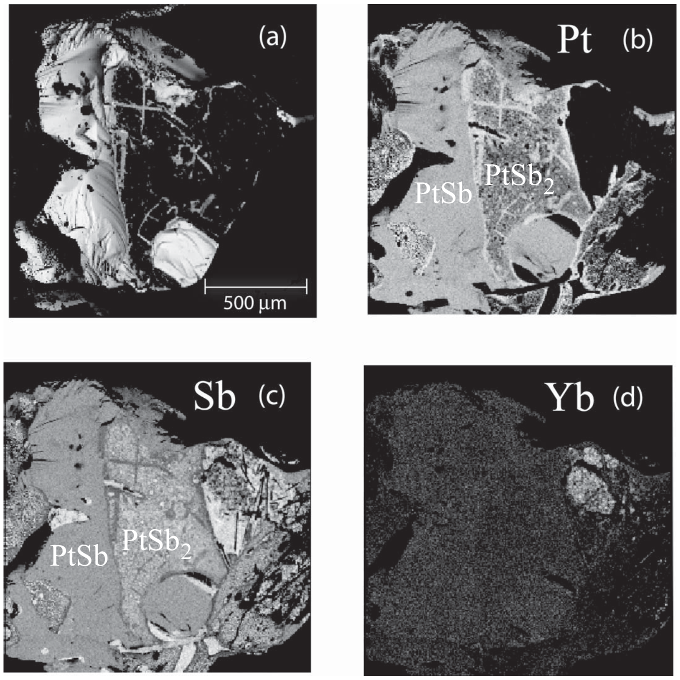

Figure 5.6: (a) Electron backscattering image of a single crystal of partially superconducting Yb doped $PtSb_2$. (b)(Pt), (c)(Sb), and (d)(Yb) are electron microprobe maps of the same crystal.

area (Fig. 5.6(b) right). The Sb map (Fig. 5.6(c)) also shows that the same two regions also contain Sb, with the lighter shaded region (Fig. 5.6(c) right) containing a higher concentration of Sb relative to the darker shaded region (Fig. 5.6(c) right). Not surprisingly residual Sb from the flux is also present in patches on the crystal surface. Quantitative EDS analysis shows that the lighter shaded region on the left side of the Pt map, which corresponds to the darker shaded region on the Sb map is PtSb, and the other region is $PtSb_2$. We believe that the impurity phase responsible for the partial superconductivity in the Yb and La doped crystals originates from thin surface layers of PtSb with a superconducting transition temperature, T_C=2.1 K [63], which is consistent with the T_C near 2 K observed in all of the superconducting crystals. We also considered the possibility that the superconducting impurity phase might be $YbSb_2$, but with T_C=1.25 K [64], it is different from the 2 K found in our crystals. Indeed, careful EDS analysis found no $YbSb_2$ on the crystal surface.

5.3.2 Ferromagnetism in Single Crystals of Ce and Gd Doped PtSb$_2$

Weak ferromagnetism was observed in some of the Gd and Ce doped crystals. We measured the field dependence of the magnetization in one Ce doped crystal and five Gd doped crystals in fields up to 9 T and at temperatures ranging from 2 to 100 K. Figure 5.7(a) is a plot of the field dependence of the magnetization for a single crystal of Gd doped PtSb$_2$ at the different temperatures indicated in the figure. As expected for a ferromagnet, the temperature dependence becomes more and more non-linear as the temperature decreases, and eventually saturates above 2 T at the lowest temperature (Fig. 5.7(a), stars). T$_C$ was determined by Arrott plot analysis of the M(H) data for all of the ferromagnetic crystals. T$_C$ for the Gd doped crystals range from 1.9 to 10.5 K, and 19 K for the Ce doped crystal. For the Gd doped crystal with T$_C$=10.5 K, the magnetization saturates above 4 T (Fig. 5.7(a)) and the associated Arrott plot (Fig, 5.7(b)) shows that a spontaneous moment develops near 10.5 K as the temperature decreases. The temperature dependence of the extrapolated zero field magnetization is mean-field like, with M(H=0)$\propto$ (1-T/T$_C$)$^{1/2}$. The different Curie temperatures among the Gd and Ce doped crystals suggest that the composition of the ferromagnetic phase varies among the different doped crystals.

We measured the temperature dependence of the DC magnetic susceptibility for all the Gd and Ce doped crystals in a 0.2 T magnetic field at temperatures from 1.8 to 300 K, and found that they all follow a Curie law, χ(T)=C/(T+θ), where C is the Curie constant, and θ is the Weiss temperature. In each case, assuming the Hund's rule moment of 7.92 μ_B for Gd^{3+}, we used the Curie constant to determine

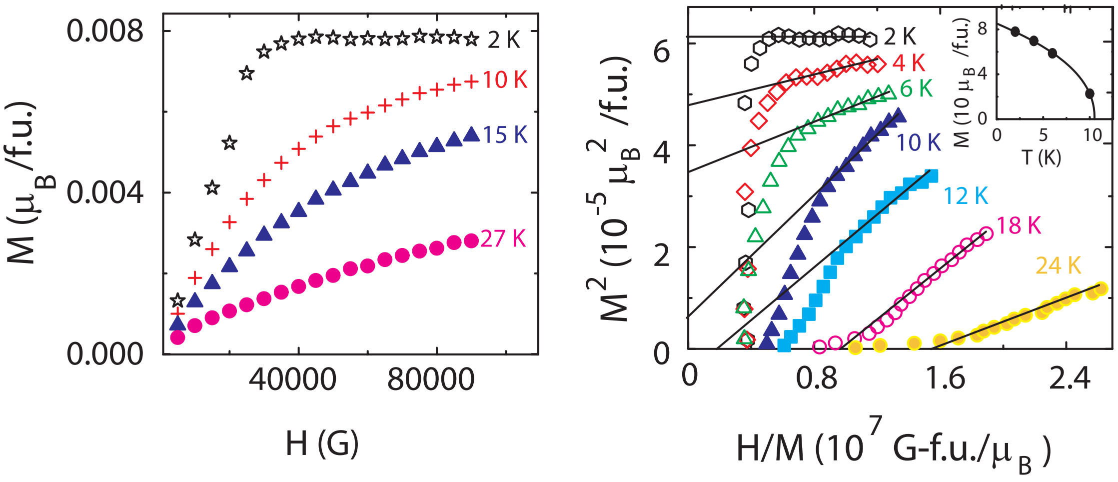

Figure 5.7: (a) The field dependence of the magnetization for a single crystal of Gd doped $PtSb_2$ at different temperatures as indicated. (b) Arrott plots for the same crystal indicating that T_C $\approx$11 K. Inset: The temperature dependence of the extrapolated zero field spontaneous moment fit to a power law in reduced temperature, t=(T-T_C)/T_C, with M$\propto$ $|t|^{-\beta}$, with β=0.37, and T_C=10.25 K.

the concentration, N, of rare earth ions in the doped crystals, since

$$C = \frac{Np^2\mu_B^2}{3k_B}$$

where μ_B is the Bohr magneton, k_B is the Boltzmann constant, N is the number of magnetic atoms, and p is the effective magnetic moment. For five of our Gd doped single crystals, we found that 0.07 to 0.16 % of the unit cells contain a Gd ion. Figure 5.8 is a plot of the temperature dependence of the magnetization for a single crystal of Gd doped $PtSb_2$ showing the typical Curie-Weiss behavior. In an effort to understand the mechanism behind the magnetic order, we looked for a relationship between the Curie temperature and the concentrations of rare earth elements in each ferromagnetic crystal (Fig. 5.8 inset). We find no relationship between T_C and the Gd concentration, which is not surprising, because the low concentrations of Gd that we found would amount to one Gd ion per 52 unit cells at most. If the ferromagnetic phase was a bulk phase, the implied large Gd-Gd spacing makes it unlikely that the Gd ions are responsible for the ferromagnetism. We conclude that the ferromagnetism more likely originates from a secondary impurity phase. Accordingly, we measured the temperature dependence of the specific heat for the Gd doped crystal with T_C=10.5 K (Fig. 5.9), which revealed a barely discernable anomaly near T_C. This result corroborates, at least qualitatively, the magnetization measurements that suggest that at most 0.16 % of the crystal is ferromagnetic.

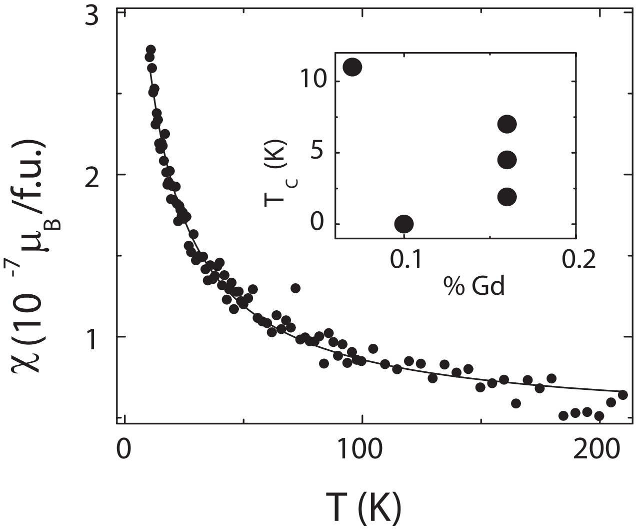

Figure 5.8: The temperature dependence of the DC magnetic susceptibility for a single crystal of Gd doped $PtSb_2$ taken in a 0.2 T field. Inset: T_C plotted as a function of Gd concentration for five different Gd doped crystals.

We performed an etching test to find out if the source of the ferromagnetism is an impurity phase on the crystal surface. Figure 5.10 is a plot of the temperature dependence of the the DC magnetic susceptibility in a 1 T field before and after a 15 minute etch in heated aqua regia. Before the etch, the susceptibility shows a rapid increase with decreasing temperature and a maximum near 10 K indicating magnetic order. After the etch, the susceptibility is negative and temperature independent except at the lowest temperatures. This diamagnetic behavior is expected for semiconductors with very low carrier concentration, such as undoped $PtSb_2$. This

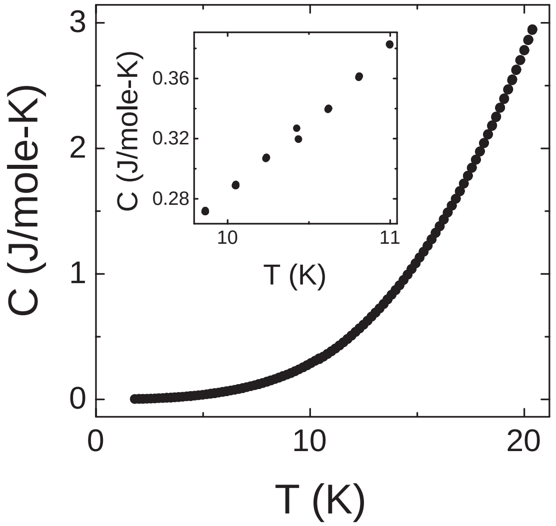

Figure 5.9: The temperature dependence of the specific heat for the Gd doped crystal with T_C=10.5 K. Inset: The specific heat near 10.5 K shows at most a tiny anomaly.

result shows that the ferromagnetism in the unetched crystal originated with a secondary impurity phase residing on the crystal surface that is easily removed with a 15 minute acid etch. However, the Curie tail observed in the etched crystal at the lowest temperatures indicates that some of Gd was successfully doped into the bulk $PtSb_2$ crystal. The inset of figure 5.10 shows a Curie-Weiss fit to the data from the etched crystal. Assuming that the Curie tail originates with Gd^{3+} ions, we find a Gd concentration of 2.65×10^{18} cm^{-3}, or 1 Gd ion per 1400 unit cells, a significant reduction from the original result of 1 Gd ion per 52 unit cells deduced from the unetched, contaminated crystal.

We used electron microprobe analysis to find and identify the surface impurity phase one of the Gd doped crystal. The electron backscattering image clearly shows regions with two different phases on the crystal surface, with the lighter shaded surface having a higher average atomic number relative to the darker shaded region (Fig. 5.11(a)). The Pt map shows an even distribution of Pt on the lower right

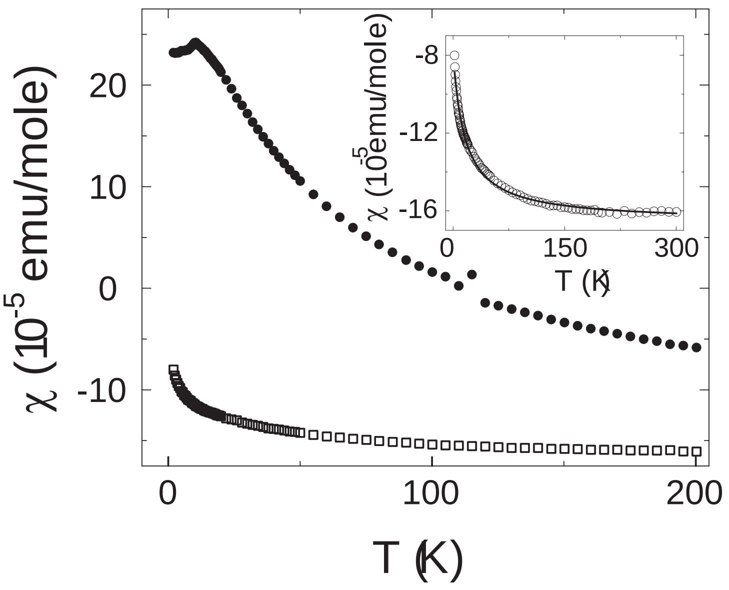

Figure 5.10: The temperature dependence of the DC magnetic susceptibility for a single crystal of Gd doped $PtSb_2$ before (filled circles) and after (hollow squares) a 15 minute etch in heated aqua regia. Inset: A Curie-Weiss fit (solid line) to the magnetic susceptibility data (hollow circles) for the etched crystal.

part of the crystal (Fig. 5.11(b)) associated with $PtSb_2$, indicating that the darker shaded region on the upper left corner is likely a surface impurity phase containing a relatively small percentage of Pt. The Sb map (Fig. 5.11(c)) shows an even distribution of Sb in both the $PtSb_2$ region in the lower right, and in the impurity phase on the upper left, but with relatively more Sb in the $PtSb_2$ region. The brighter regions on the surface indicate regions of excess Sb flux. The Gd map (Fig. 5.11(d)) shows that all the Gd is located at the impurity phase in the upper left region, with no Gd present in the bulk $PtSb_2$ crystal. Quantitative EDS analysis showed that the Gd based surface impurity is roughly 16% Pt, 38% Sb and 46% Gd. To our knowledge, there is no Gd based intermetallic of this composition reported. We conclude that this compound is the source of the ferromagnetism in the Gd doped crystals. We performed a similar electron microprobe measurement (Fig. 5.12) on a Ce doped crystal of $PtSb_2$ that was found to be ferromagnetic via Arrott plot analysis, with $T_C \sim 19$ K. We once again found regions of leftover Sb flux on the

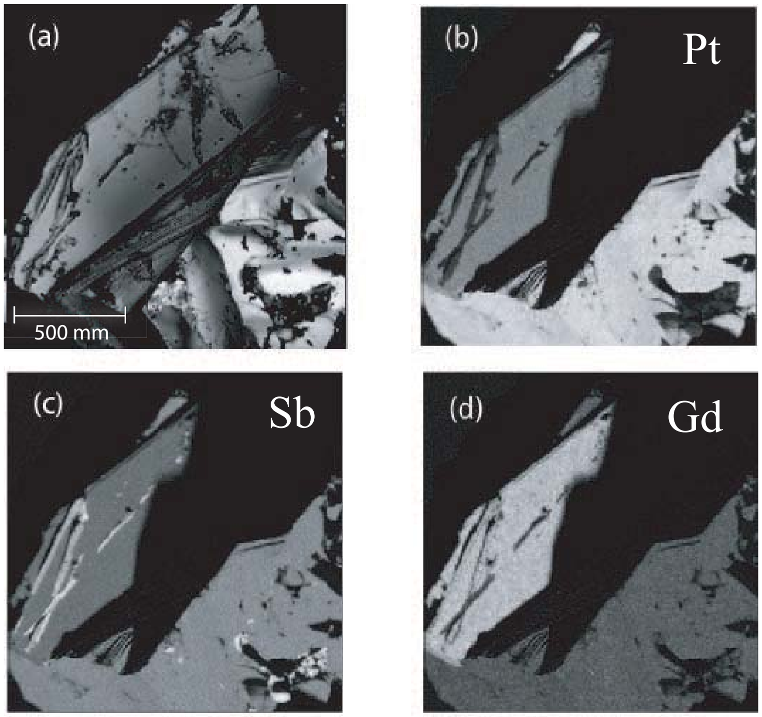

Figure 5.11: (a) An electron backscattering image of a single crystal of Gd doped $PtSb_2$. (b) Pt, (c) Sb, and (d) Gd electron microprobe maps of the same region.

surface (Fig. 5.12(c)) and also a surface impurity region, but over a much smaller area (Fig. 5.12(d)). Quantitative EDS analysis found the composition to be very close to $CeSb_2$, which has a reported Curie temperature of 15 K [65], which is close to the Curie temperature that we estimated using Arrott plot analysis. We conclude that the ferromagnetism in the Ce doped crystal originates with the small amounts of $CeSb_2$ that grew on the surface of $PtSb_2$ as a secondary impurity phase.

So far, we have found that for all of our measured crystals, all observations of superconductivity and ferromagnetism originate with secondary impurity phases found on the crystal surfaces. We have also found that we can remove these impurity phases by acid etching. In the next section, we study the bulk properties of etched rare earth doped $PtSb_2$ via heat capacity measurements.

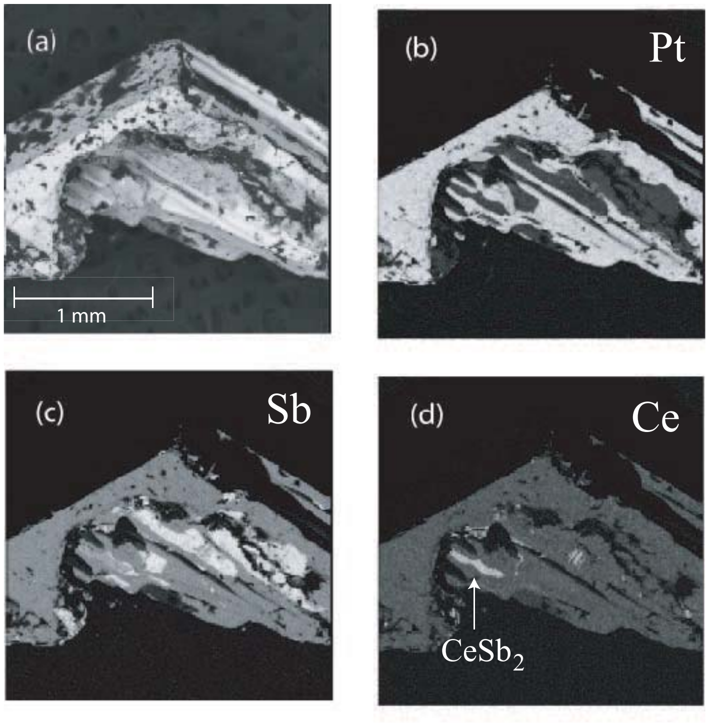

Figure 5.12: (a) An electron backscattering image of a single crystal of Ce doped $PtSb_2$. (b) Pt, (c) Sb, and (d) Ce electron microprobe maps of the same region.

5.3.3 Bulk Properties of Rare Earth Doped $PtSb_2$

In this section, we present the results of heat capacity measurements of etched rare earth doped $PtSb_2$. We compare the bulk electronic properties among the crystals by comparing the electronic part of the heat capacity. We measured the temperature dependence of the heat capacity for three Yb doped crystals, an La doped crystal and a Eu doped crystal. With the exception of the Eu doped crystal, which is insulating, all the other crystals show evidence that the rare earth doping has modified the electronic properties. We assume that the heat capacity has two parts, $C=C_E+C_P$, where $C_E=\gamma T$ is the electronic part of the heat capacity due to the conduction electrons and $C_P=\beta T^3$ is the phononic part of the heat capacity. Experimentally, we obtain values for γ and β by plotting the heat capacity divided by temperature,

$C/T=\gamma+\beta T^2$ as a function of T^2 (Fig. 5.13(a)), where γ is given by the y-intercept and β is given by the slope of the line. We have also experimentally determined the carrier concentrations from Hall voltage measurements, so we can compare the values of γ and β obtained from the heat capacity measurements with those expected in the Sommerfeld model for the free electron gas, where $\gamma=\pi^2 n k_B^2 m_e^*/\hbar^2 k_F^2$, where k_F is the Fermi momentum, given by $k_F=(3\pi^2 n)^{1/3}$, which yields the relation $\gamma=m_e^* n^{1/3}$ (Table 4.2). In Figure 5.13(b), we compare the electron concentration dependence obtained from the heat capacity data with the Sommerfeld value calculated using the electron concentration obtained from Hall voltage measurements. We find that γ increases linearly with n, not as $n^{1/3}$, suggesting that there could be an increase in m^* with increasing n.

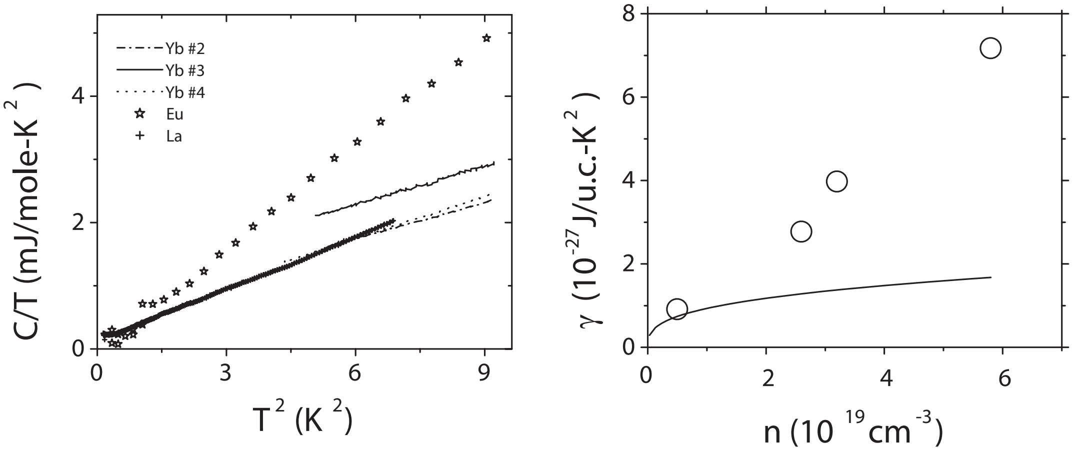

Figure 5.13: (a) The specific heat divided by temperature plotted as a function of temperature squared for three Yb doped crystals, one Eu doped crystal and one La doped crystal. (b) The electron concentration (n) dependence of γ obtained from the Sommerfeld model with with $m^*/m_e=1$ (solid line) and for γ obtained from the plot in (a) (circles).

5.4 Conclusions

Our experimental results indicate that most of rare earth dopants end up in secondary impurity phases on the surface of the $PtSb_2$ crystals, which leads to the

Table 5.2: Calculated and experimental values of γ and β obtained for three Yb doped crystals, one Eu doped crystal and one La doped crystal.

Crystal	γ_{calc} (mJ/mole-K^2)	γ_{fit} (mJ/mole-K^2)	β_{fit}
Yb2	0.097	0.279	0.191
Yb3	0.065	0.279	0.201
Yb4	0.111	0.240	0.221
Eu	2.22	0	0.542
La	0.334	0.410	0.270

observation of partial superconducting or ferromagnetic transitions. However, after removing the impurity phases with an acid etch, we find that some of the rare earth elements were successfully doped into the bulk in up to 1 in 1400 unit cells. A previous attempt to dope $PtSb_2$ with Mn found similar complications during crystal growth [66]. In this case, a Czochralski method was used to grow the crystals, but most of the Mn ended up in secondary impurity phases on the crystal surface. Although neither attempt was successful at doping $PtSb_2$ with high concentrations of magnetic elements, we believe that $PtSb_2$ still holds promise as a host for magnetic ion doping, and does not necessarily have a limited solubility for rare earth or transition metal elements. Given the high crystal symmetry, and the small band gap of $PtSb_2$, we still believe that it holds great promise as a host for magnetic ion doping, but it is clear that neither flux growth, nor Czochralski growth methods are suitable for synthesizing heavily doped single crystals of $PtSb_2$. For the small concentrations of rare earths that were successfully doped into $PtSb_2$, we found that the n dependence of γ was enhanced compared with the Sommerfeld model for the free electron gas, suggesting that m* increases with increasing n.

CHAPTER VI

Magnetic Field Tuning of Electronic and Magnetic Phases in $\mathbf{Yb_3Pt_4}$

6.1 Introduction

We now focus on the high n and N region of Figure 1.1, represented by rare earth based intermetallic compounds, where the magnetic rare earth elements Ce and Yb are combined with other metallic elements to form binary or ternary intermetallics, with the Ce or Yb atoms forming a lattice of local magnetic moments. These compounds typically are magnetically ordered at low temperatures and will sometimes form novel electronic and magnetic states when external pressure or magnetic field is applied [13, 14, 15, 16]. The experimental exploration of these novel phases is the subject of this chapter. We will present our extensive measurements of single crystals of a new binary intermetallic antiferromagnet, Yb_3Pt_4, which we synthesized by the flux growth method. In zero field, the antiferromagnetic transition occurs at T_N=2.4 K for Yb_3Pt_4, but we will show that T_N decreases with increasing magnetic field and eventually at H=1.6 T and T_N=0, terminates at a quantum critical point (QCP). A QCP occurs where the magnetic ordering temperature is suppressed to T=0. This suppression of T_N to zero is common with a number of these types of antiferromagnetic compounds, including $YbRh_2Si_2$, where T_N=70 mK in zero field, but is driven to T_N=0 by applying a magnetic field of 0.7 T [9] and $CeCu_{5.8}Au_{0.2}$, where T_N is driven from 0.22 K at ambient pressure to zero with the application of 5 kbar of pressure [67]. In 1977, based on two competing mechanisms, the Kondo effect and the RKKY interaction, Doniach deduced a generic phase diagram describing this suppression of magnetic order. We begin this chapter with a description of the Kondo Effect, the RKKY interaction and how their competition leads to the Doniach phase diagram.

6.1.1 The Kondo Effect

Understanding the presence of a broad minimum at low temperatures in the resistivity in nominally pure metals had been a theoretical challenge for years until 1964, when J. Kondo solved the problem by considering a single localized d-electron magnetic impurity coupled to itinerant electrons in a metal [68]. The cause of the minimum is the interaction between the conduction electrons and the magnetic impurity. As the temperature decreases, this magnetic interaction between the localized d-electron and the conduction electrons begins to have a significant effect on the resistivity via the spin-flip scattering of the itinerant electrons from the magnetic impurity. At sufficiently low temperature, the conduction electrons form a spin singlet state with the localized moments. This state of lowest energy requires the spins to be antiparallel, which is satisfied for the localized electron having spin up and the itinerant electrons having spin down, or the opposite case. Since these two cases are indistinguishable, the ground state of this system is a singlet linear combination of both states, where the wavefunction is

$$\frac{1}{\sqrt{2}}(\uparrow_L\downarrow_I - \downarrow_L\uparrow_I),$$

where ↑ represents the spin up state, ↓ represents the spin down state and L and I indicate the localized and itinerant electrons. In this way, the Kondo effect quenches the local moments present at high temperatures and creates a non-magnetic ground state.

The exchange interaction between a conduction electron and a local magnetic moment is quantified by the Kondo Hamiltonian,

$$H_K = -2JS_kS_l$$

where J is the exchange interaction, S_k is the spin of the interacting conduction electrons, and S_l is the localized spin. This interaction leads to the resistivity due to the magnetic impurity, $\rho \propto$ -ln(T/T_K) via the second order Born approximation [68], which leads to a correct prediction of the resistivity in metals with magnetic impurities. T_K is the approximate temperature scale, below which the interacting conduction electrons form the Kondo singlet with the local moment. There is, however, another interaction, the Ruderman-Kittel-Kasuya-Yosida (RKKY) interaction, that competes with the Kondo effect in the heavy fermion materials acting to magnetically order localized spins via the conduction electrons.

6.1.2 The RKKY Interaction

In the 1950s, Ruderman and Kittel [69], and Kasuya [70] and Yosida [7], independently determined that the same mechanism responsible for conduction electrons indirectly mediating the hyperfine interaction between nuclear spin and s-electron spin in metals also led to magnetic order in metals where the local moments are located too far apart to experience strong nearest neighbor dipolar interactions. In the RKKY interaction, the magnetization density of the conduction electrons is spatially modulated around localized f-electron moments. The spatially oscillating spin density of the conduction electrons conveys the spin information between distant local moments allowing them to interact indirectly. The exchange Hamiltonian,

$$H_{RKKY} \propto S_i S_j J^2 f(2k_F r),$$

where S_i and S_j are the interacting localized spins, J is the exchange interaction, k_F is the Fermi wave vector, and

$$f(2k_F r) = \frac{sin(2k_F r) - 2k_F r cos(2k_F r)}{(2k_F r)^4},$$

which is a damped oscillating function of $2k_F r$ extending outward from the localized moment (Fig. 6.1) [34], making the exchange interaction ferromagnetic for positive values of f, and antiferromagnetic for negative values of f. The RKKY interaction can create long range magnetic order, coupling moments that are too far apart to order by a direct mechanism. In 1977, based on a one-dimensional chain of interacting moments, Doniach predicted a phase diagram for systems in which RKKY interactions compete with the Kondo effect [71]. We describe the resulting phase diagram in the next section.

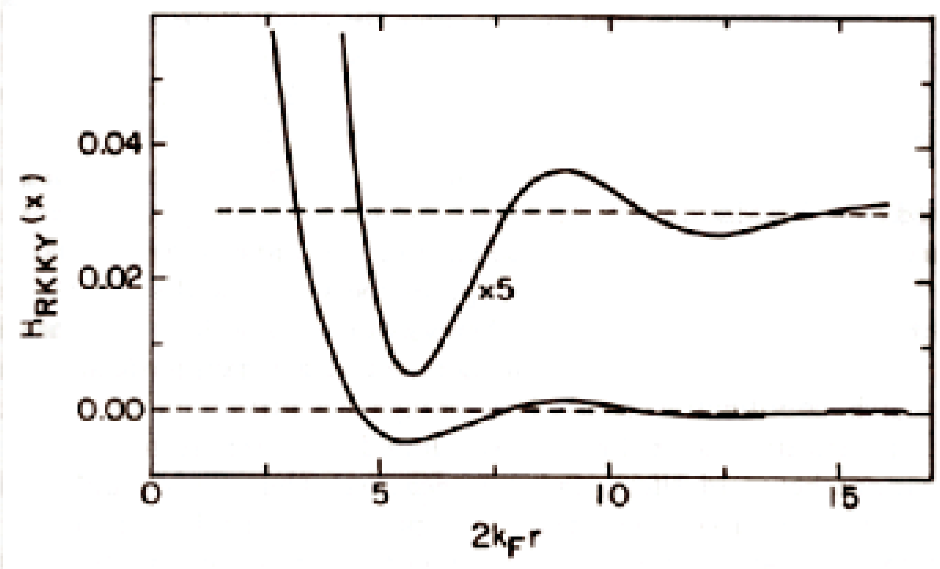

Figure 6.1: A plot of the oscillating RKKY function (Figure from O Handley, 2000 as referenced in the text).

6.1.3 The Doniach Phase Diagram

In Doniach's phase diagram, the resulting phases are determined by the competition between the Kondo effect and the RKKY interaction. The magnetic ordering temperature in the RKKY interaction,

$$T_{RKKY} \propto J^2 \eta(E_F),$$

where J is the exchange interaction, and $\eta(\mathrm{E}_F)$ is the conduction electron density of states at the Fermi level, E_F. In the Doniach model, the exchange interaction, J also governs the Kondo effect, with

$$T_K \propto \eta(E_F)^{-1} e^{\frac{-1}{J\eta(E_F)}}.$$

Experimentally, J can be tuned by a parameter such as doping, magnetic field or pressure to adjust the relative magnitudes of the RKKY interaction and the Kondo effect. Figure 6.2 is a schematic of the Doniach phase diagram. The J dependencies of T_K and T_{RKKY} are plotted on the diagram to show that for low values of J, the RKKY interaction dominates and the material is magnetically ordered. At high values of J, the Kondo effect reduces the local moment magnitude and the magnetic order is suppressed. The phase transition at the QCP occurs at T=0 when $\mathrm{T}_{RKKY} \approx \mathrm{T}_K$. It is remarkable that the resulting phase diagram based on these two simple interactions accurately describes the suppression of magnetic order in heavy fermion systems such as $\mathrm{YbRh_2Si_2}$, by magnetic field and $\mathrm{CeCu_{5.8}Au_{0.2}}$, by pressure. Based on experimental results, the Doniach phase diagram also includes the development of a Fermi liquid (FL) phase, shown in the high J region, which is a fundamental theory that describes normal metals.

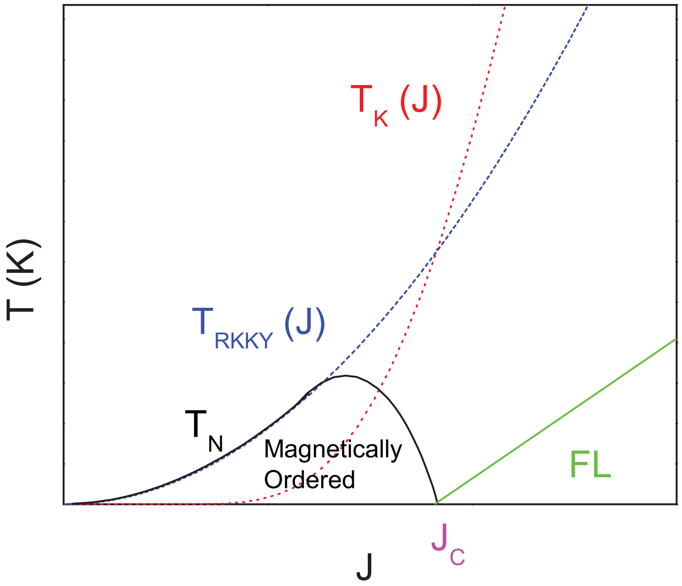

Figure 6.2: The expected Doniach phase diagram for a typical Ce or Yb based intermetallic crystal containing a lattice of local f-electron magnetic moments. Below the QCP, the RKKY interaction is dominant (blue dotted line), but above the QCP, the Kondo effect (red dotted line) is dominant.

6.1.4 Introduction to the Fermi Liquid

Landau proposed his phenomenological Fermi liquid theory to describe the behavior of a collection of strongly interacting fermions, such as liquid ^{3}He. It is a testament to its success that Fermi liquid theory also describes the behavior of electrons in metals, including the normal metallic state of heavy fermion systems at low temperatures. In their book on quantum liquids [72], Pines and Nozieres give a good description of the development of a Fermi liquid from a dilute gas as the temperature is decreased. At high temperature and low density, each fermion behaves independently, with negligible interactions and is well described by the theory of a classical gas. As temperature decreases, the thermal energy decreases and the fermion density increases, leading to an increase in fermion-fermion interactions. Eventually, there is a phase transition to a classical liquid state. As the temperature continues to decrease, the fermions become more and more strongly correlated and the density continues to increase as the thermal energy becomes very small. Eventually, the density is high enough so that the inter-fermion spacing is comparable to the de Broglie wavelength of the fermion, and thus we move from a classical to a quantum regime, where the behavior of fermions and bosons is strikingly different. For example, liquid ^{4}He is a Bose liquid, and liquid ^{3}He is a Fermi liquid. Obvious from their name, heavy fermion materials consist of high densities of fermions (electrons), and so we limit our discussion to the properties of Fermi liquids.

One of the key features of Fermi liquid theory is a one to one correspondence between the electrons in the electron gas and the electrons in the Fermi liquid, which can no longer be viewed as individual particles [72]. Because the electrons are in a liquid-like state, they are strongly correlated and excitations end up simultaneously affecting many electrons. It is thus not accurate to consider the excitations of a single electron. Excitations within this electron liquid are called quasiparticles. Because the electrons are strongly correlated, if the properties of a single electron are measured, it behaves as if it has a much bigger mass than a single electron, because if it is moved by some force, it drags its environment with it and thus seems much heavier. This effect is quantified by replacing the electron mass, m_e with the effective mass, m*. In normal metals, $m^* \approx m_e$, but the heavy fermion materials are called heavy, because they can have values of m* as large as 1000 m_e [73]. In this state, since the electrons are interacting, the action of one electron affects all the other electrons. The Fermi liquid theory describes a system of quasiparticles. The energy of a single quasiparticle is

$$E_0 = \hbar^2 k^2 / 2m*,$$

where k is the wavevector and m* is the effective mass. If we add one quasiparticle to a system of quasiparticles, we need to consider the energy of the quasiparticle, plus the energy of its interactions with each of the other quasiparticles, so its energy will be

$$E_k = E_0 + \frac{1}{V}\sum_{k'} f(k,k')\delta(k'),$$

where k and k' are the wavevectors of the added quasiparticle and the interacting quasiparticle in the system, V is the volume of the system, δ(k') is 1 for a quasi-electron, and -1 for a quasi-hole and f(k,k') is the quasiparticle interaction function. Because the two interacting quasiparticles can have either parallel or antiparallel spins, the interactions can be broken up into two independent parts,

$$f(k\uparrow, k'\uparrow) = f^s(k,k') + f^a(k,k')$$

$$f(k\uparrow, k'\downarrow) = f^s(k,k') - f^a(k,k')$$

Because it is assumed that interacting quasiparticles lie close to the Fermi surface, k≈k'≈k_F, the interaction function can expressed as a series of Legendre polynomials,

$$f^{a,s}(k,k') = \sum_l f_l^{a,s} P_l(cos\theta).$$

These coefficients are normally expressed in a dimensionless form, $F_l^{a,s}$=$\eta(E_F)f_l^{a,s}$, where $\eta(E_F)$ is the density of states at the Fermi level, $\eta(E_F)$=$m^*k_F/\pi^2\hbar^2$. Based on these results, expressions for the expected magnetic susceptibility, specific heat, and resistivity can be deduced.

Specific observable predictions of Fermi liquid theory occur in the temperature dependence of the resistivity, specific heat, and magnetic susceptibility [15, 13, 72]. For the electronic specific heat,

$$C(T) = \gamma T,$$

where γ=$\pi^2k_B^2\eta(E_F)/3$, where $\eta(E_F)$=$m^*k_F/\pi^2\hbar^2$ is the density of states at the Fermi energy. Since $\eta(E_F)$=$m^*k_F/\pi^2\hbar^2$, γ=$k_B^2k_Fm^*/3\hbar^2$. This is the same expression found in the Sommerfeld model of non-interacting electrons, but the mass of the electron, m_e is replaced by the effective mass, m*. Thus, γ is a measure of the effective mass, m*. As mentioned previously, the class of heavy fermion materials is distinguished by their very large m*, up to 1000 m_e [74]. For resistance measurements,

$$\rho(T) = \rho_0 + AT^2 \ (T < T_{FL}),$$

where ρ_0 is the remaining resistivity at T=0, due to impurities, T is the temperature, where T_{FL}=E_F/k_B is the Fermi temperature, and E_F is the Fermi energy. The heavy fermion compounds also have very large values of A, which measures the quasi-particle scattering, $A \propto 1/T_{FL}^2 \propto (m^*)^2$ [13]. The magnetic susceptibility for systems with interacting electrons is given by

$$\chi(T) = \frac{\mu_B^2 m^* k_F}{\pi^2 \hbar^2} \frac{1}{1 + F_0^a},$$

where F_0^a is the dimensionless spin antisymmetric Landau parameter. This is just the temperature independent non-interacting Pauli susceptibility, $\chi = \mu_B^2 \eta(E_F)$, increased by the dimensionless factor, $(m^*/m_e)/(1+F_0^a)$. For χ to remain positive, F_0^a >-1. For the case of the diverging susceptibility associated with ferromagnetism, F_0^a=-1. An in-depth theoretical explanation of the Fermi liquid and the derivations of the expected observables can be found in the quantum liquids book by Pines [72] and in the review article by von Lohneysen [13].

There are two useful relations between Fermi liquid parameters that are often used to analyze and classify heavy fermion materials. In 1986, Kadowaki and Woods observed what seems to be a universal constant relation between A and γ [75]. It is known as the Kadowaki-Woods relation and finds a constant value for most heavy fermion intermetallics, with

$$A/\gamma^2 = 10\mu\Omega - cmK^2mol^2/J^2.$$

Another commonly used ratio is the Sommerfeld-Wilson ratio that relates χ_0 to γ,

$$R_W = \frac{\pi^2 k_B^2 \chi_0}{\mu_{eff}^2 \gamma}.$$

For the case of a non-interacting system, R_W=1, while heavy fermion compounds typically have significantly higher values. Based on a theoretical calculation, a spin 1/2 Kondo system should have a value of R_W=2 [76]. Substantially larger values are found in systems with magnetic correlations [77]. Superconductors are found to have R_W <2 [77]. We will show in later sections that Yb_3Pt_4 shows very high values of χ_0 and A, suggesting that it could be a heavy fermion compound, but the coefficient of the electronic part of the heat capacity, γ is not enhanced. We use the Kadowaki-Woods ratio, and R_W to compare Yb_3Pt_4 to other heavy fermion compounds that have similar values of A and χ_0.

6.1.5 Quantum Critical Points in Heavy Fermion Compounds

Figure 6.3 is a schematic of the typical Doniach-like phase diagram found in quantum critical heavy fermion materials, including $YbRh_2Si_2$ and $CeCu_{6-x}Au_x$. In measurements of these materials, we observe much more than just the suppression of T_N to zero temperature. The point on the phase diagram where T_N=0 is a special point known as a quantum critical point (QCP) that influences the states of matter over a wide region of the phase diagram, and sometimes leads to newly observed phases of matter including an unconventional metallic phase and unconventional superconductivity. We will describe the properties of $YbRh_2Si_2$ and $CeCu_{6-x}Au_x$, which display actual QCPs and of $CePd_2Si_2$ and $CeCu_2(Si_{1-x}Ge_x)_2$ which display unconventional superconductivity.

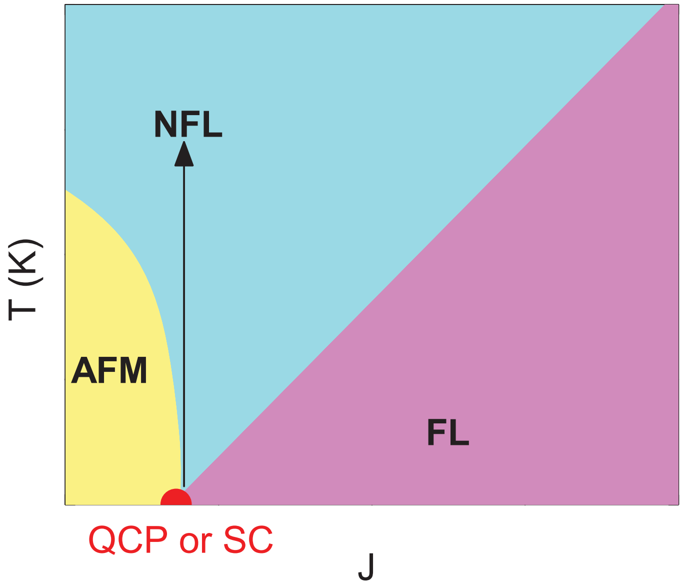

Figure 6.3: A schematic of the typical phase diagram found for quantum critical heavy fermion compounds.

During a classical second order phase transition from a magnetically ordered state at lower temperatures to a paramagnetic state at higher temperatures, thermal fluctuations continuously increase with increasing temperatures until the thermal energy becomes greater than the energy of the magnetic interactions, destroying the magnetic order. Analogously, at a QCP a magnetically ordered state at T=0 transitions to a paramagnetic state via the application of pressure or magnetic field. Because the transition at a QCP occurs at T=0, it is not driven by thermal fluctuations, but by zero-point quantum fluctuations, making it a quantum phase transition (QPT). The discovery of quantum critical points and their associated novel phases of matter in experimentally determined phase diagrams of rare-earth based intermetallic compounds has generated intense interest and experimental and theoretical efforts to better understand these systems [15, 16, 13, 14]. The quantum critical point (QCP) is ultimately thought to be the origin of these phases [13, 14]. It is only very recently that systems with QCPs have been experimentally observed and thoroughly studied and many more quantum critical materials need to be synthesized and measured in order to guide a better theoretical understanding of the mechanisms behind these phases [13, 14]. There are actually many heavy fermion materials that have been tuned to a QCP via doping [15, 16], but these are not very useful systems for the study of quantum criticality, because doping introduces disorder and the effects of the disorder tend to be very strong near quantum critical points. To date, the two best examples of materials that have a QCP are the rare earth based compounds, $YbRh_2Si_2$ (Fig. 6.4(a)) [9] and $CeCu_{6-x}Au_x$ (x=0.1-1) (Fig. 6.4(b)) [67]. These types of compounds are classified as heavy fermions for reasons that will be discussed later in the chapter. Fig. 6.4 shows the field-temperature (H-T) phase diagram for

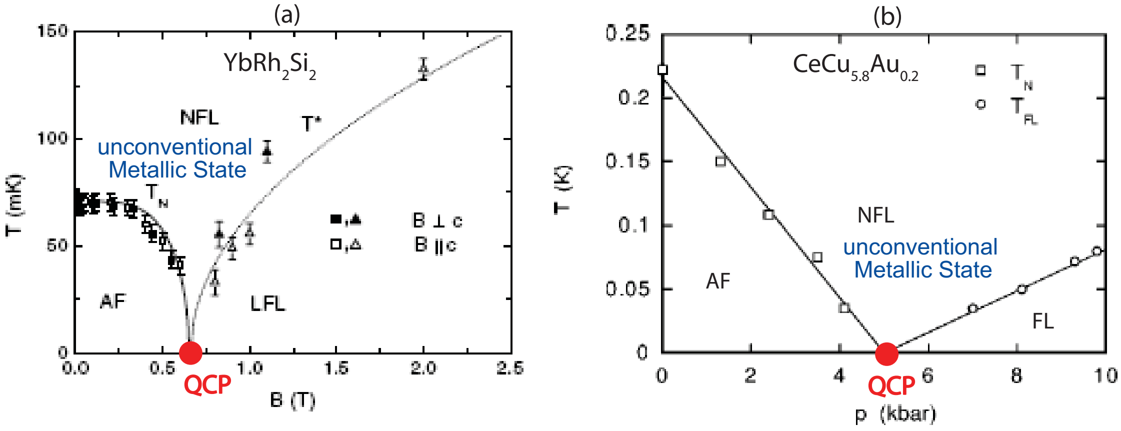

Figure 6.4: (a) The H-T phase diagram for $YbRh_2Si_2$ has a QCP near 0.8 T. At low magnetic fields and temperatures, $YbRh_2Si_2$ is antiferromagnetically ordered and at magnetic fields beyond the QCP, it is in a normal metallic, Fermi liquid state. The unconventional non-Fermi liquid metallic state extends upward in temperature from the QCP (Figure from Gegenwart, 2002 as referenced in the text) (b) The P-T phase diagram for $CeC0_{5.8}Au_{0.2}$ has a pressure driven QCP from an antiferromagnetic state near 5 kbar and also has the unconventional non-Fermi liquid metallic state extending upward in temperature from the QCP (Figure from von Lohneysen, 2001 as referenced in the text).

$YbRh_2Si_2$ and the pressure-temperature (P-T) phase diagram for $CeCu_{5.8}Au_{0.2}$. In each case, there is a QCP, as indicated in the figure. There are common features shared by the phase diagrams of these two quantum critical heavy fermion materials.

At low temperatures and low values of the tuning parameter (pressure or magnetic field), there is an antiferromagnetically ordered state that can then be tuned to a QCP. Beyond the QCP there is a conventional Fermi liquid (FL) metallic state. One of the properties of quantum critical systems that is generating interest is the presence of an unconventional non-Fermi liquid (NFL) metallic state extending upward in temperature over a surprisingly large range, demonstrating the strong influence of the QCP on the electronic properties of quantum critical systems. Equally intriguing is the recent discovery and measurement of unconventional superconductivity in the quantum critical heavy fermion compounds, $CePd_2Si_2$ (Fig. 6.5(a)) [11] and $CeCu_2(Si_{1-x}Ge_x)_2$ (Fig 6.5(b)) [12]. For the case of $CeCu_2(Si_{1-x}Ge_x)_2$, when x=0.25, there is a QCP ∼2.2 GPa, but for x=0.1, as pressure increased, before the antiferromagnetic state reaches a QCP, an unconventional superconducting phase forms

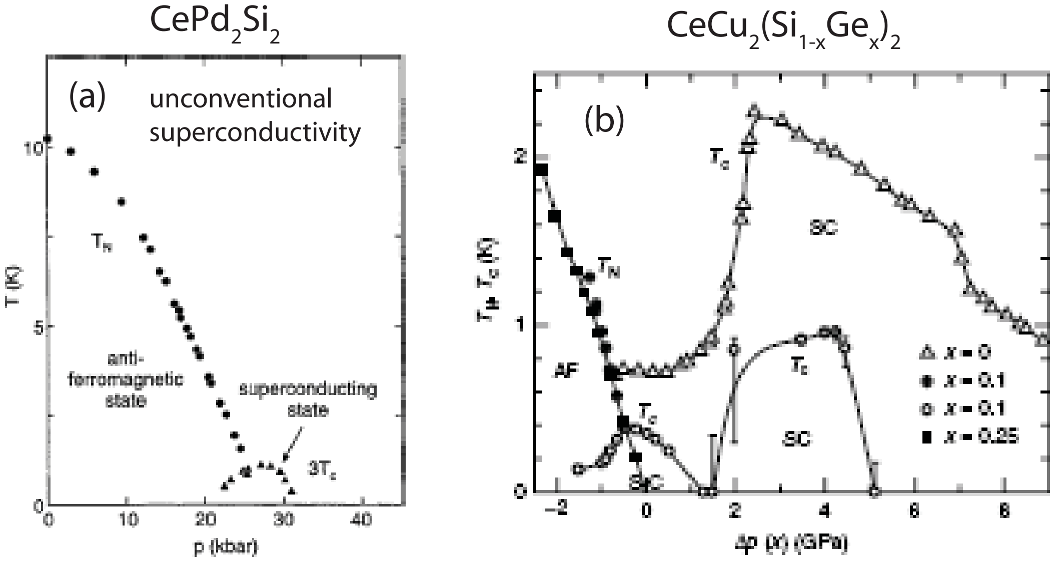

Figure 6.5: (a) The P-T phase diagram for $CePd_2Si_2$ has the expected antiferromagnetic state at low temperatures and pressures, but as pressure increases, instead of reaching a QCP, a region of unconventional superconductivity develops around the expected QCP (Figure from Yuan, 2006 as referenced in the text). (b) The P-T phase diagram for $CeCu_2(Si_{1-x}Ge_x)_2$ again showing how antiferromagnetic order and unconventional superconductivity are found so close together (Figure from Mathur, 1998 as referenced in the text).

around the expected QCP. It is surprising that magnetic order and superconductivity, two normally mutually exclusive states are located so close to one another. The close proximity of these unconventional quantum critical superconducting states to antiferromagnetic QCPs suggests that the superconductivity may be magnetically mediated. This observation has added to the already intense interest in quantum critical systems. However, just like $YbRh_2Si_2$ and $CeCu_{6-x}Au_x$, there are very few materials available that display this unconventional superconductivity. In addition to $CePd_2Si_2$ and $CeCu_2(Si_{1-x}Ge_x)_2$ another promising group of materials showing unconventional superconductivity is the 1-1-5 materials based on $CeCoIn_5$, where Co can be replaced by Rh or Ir [78]. So far, all of the heavy fermion materials displaying either a QCP or unconventional superconductivity are antiferromagnetic and none are quantum critical ferromagnets. It would be a significant experimental breakthrough to discover a heavy fermion ferromagnet that can be tuned to a QCP and very important to theorists working on magnetic QCPs. Unfortunately heavy fermion ferromagnets are rare, and attempts to synthesize one continues to be a major ongoing effort in our research group. Ferromagnetic QCPs do exist in other classes of materials. Quantum critical points have been found in weak itinerant ferromagnets, including $ZrZn_2$ [79] and MnSi [80], FeGe [81] and also in $Sr_3Ru_2O_7$ [82], which is a magnetically induced ferromagnet with a possible QCP. These systems, however, display a different type of phase diagram (Fig. 6.6(a)) [13, 83] with an initially second order phase line becoming a first order phase line before a QCP is reached. The pressure-temperature phase diagram for the itinerant helical ferromagnet, MnSi, for example, becomes first order above a certain pressure, p*, before T_C reaches zero (Fig. 6.6(b)) [13, 84].

Theoretical efforts to understand magnetic quantum phase transitions (QPT) in

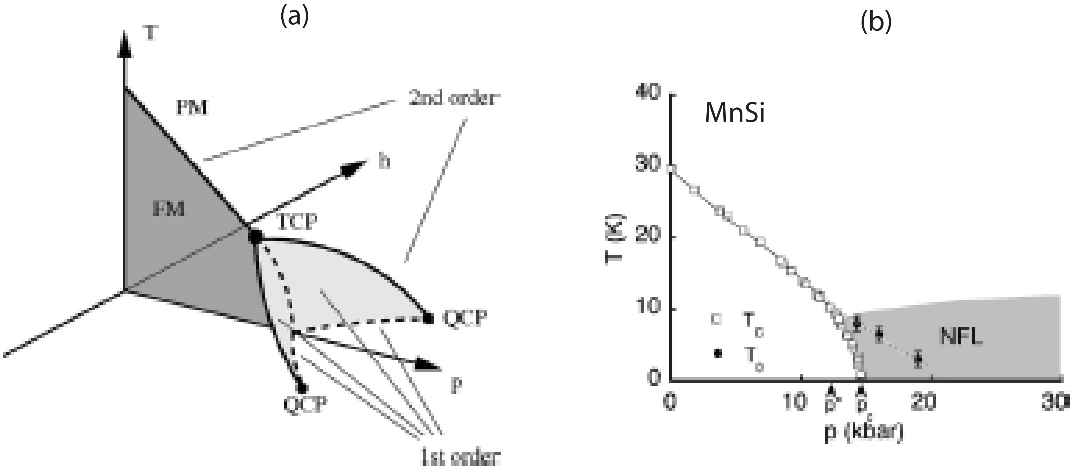

Figure 6.6: (a) Generic pressure-field-temperature phase diagram by Belitz, 2005 (Figure from von Lohneysen, 2007 as referenced in the text). (b) The P-T phase diagram by Pfleiderer, 2004 for MnSi showing the ferromagnetic phase line becoming first order above p* (Figure from von Lohneysen, 2007 as referenced in the text).

metals have been ongoing, beginning with the early work of Hertz in 1976 on continuous quantum phase transitions in metals [85]. Good review articles about the current theoretical and experimental developments can be found in papers by Lohneyesen et al [13] and Gegenwart et al [14]. A comprehensive list of intermetallic compounds displaying NFL behavior can be found in review papers by Stewart [15, 16]. Much more experimental work is needed and the current lack of more quantum critical materials and experimental results has motivated our efforts to synthesize new quantum critical materials. We have succeeded in synthesizing an unconventional antiferromagnetic material, Yb_3Pt_4, which can be tuned to a QCP with an applied magnetic field of 1.6 T. The properties of this material are unique among quantum critical systems, with a weakly first order phase transition from a local moment paramagnetic state to a Fermi liquid antiferromagnetic state at 2.4 K. The temperature of the first order phase transition decreases with increasing magnetic field and terminates at a critical endpoint, but then continues to a QCP, but as a second order phase transition.

6.1.6 Evolution of the Fermi Liquid Parameters across phase lines near a QCP

One of the key signatures of a QCP is the divergence of the effective mass on approach to the QCP from the FL regime [13, 14]. Since the coefficient of the electronic part of the heat capacity, γ is a direct measure of the effective mass in a FL, we expect quantum critical heavy fermions to show a divergence in γ on approach to the QCP in the FL regime. This behavior is observed in the previously discussed quantum critical heavy fermion compound, $YbRh_2Si_2$ (Fig. 6.7 (red circles)) [86]. We also know from FL theory that A $\propto$ $(m^*)^2$, so we also expect A to diverge on approach to the QCP from the FL regime. This is exactly the behavior observed in $YbRh_2Si_2$ (Fig. 6.7 (blue triangles)) [86].

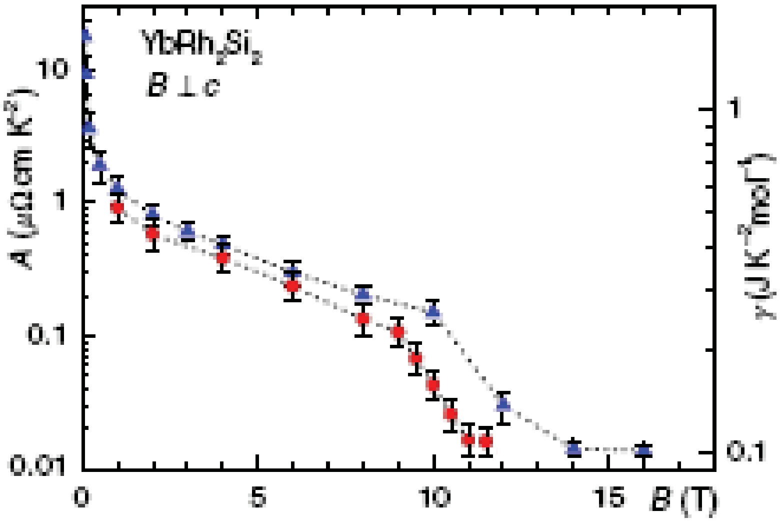

Figure 6.7: The temperature dependence of the quadratic part of the resistivity, A (blue triangles), and the coefficient of the linear temperature dependence of the specific heat for a FL, γ (red circles), showing how both of these values diverge at the QCP because of the diverging effective mass, m* (Figure from Gegenwart et al, 2006 as referenced in the text).

As previously discussed, FL and NFL regimes in quantum critical heavy fermion compounds can be directly observed in measurements of the heat capacity, resistivity and magnetic susceptibility. Values of γ are obtained from measurements of the heat capacity by plotting C/T versus T and extrapolating to T=0. For quantum critical heavy fermions, γ is expected to be large and in the FL regime, C=γT, and in the NFL regime, C$\sim$TlnT. This behavior is evident in the plots of the temperature dependence of these quantities in both $YbRh_2Si_2$ (Fig. 6.8(a))and $CeCu_{5.8}Au_{0.2}$ (Fig. 6.8(c)). γ is 2 J/mole-K^2 for $YbRh_2Si_2$ and 3 J/mole-K^2 for $CeCu_{5.8}Au_{0.2}$, among the highest observed values of γ among heavy Fermion materials. The expected FL behavior is also observed for both materials, with C/T nearly constant in the FL regime, and C/T$\sim$ lnT in the NFL regime, extending upward in temperature from the QCP.

In both $YbRh_2Si_2$ (Fig. 6.9(a)) [9] and $CeCu_{5.8}Au_{0.2}$ (Fig. 6.9(b)) [10], the FL region is also marked by the quadratic temperature dependence of the resistivity. Both materials also show a linear temperature dependence extending upward in temperature from the QCP, as expected for the NFL regime. The expected very high values of the magnetic susceptibility, χ_0 for quantum critical heavy fermion materials are observed in $YbRh_2Si_2$, as high as 10^{-5} m^3/mole, which puts it among the highest values observed in the heavy fermions [87]. At low temperatures and low fields, the susceptibility is temperature independent, consistent with the Pauli susceptibility of a FL. In the next section, we present our measurements of Yb_3Pt_4, which has a field tuned QCP, but with unique properties that deviate from those of the two known quantum critical systems described above. We present our results beginning with our zero field measurements in the following section. As shown in Fig. 6.3, one of the hallmarks of a system with a QCP is a large region of NFL behavior extending upward in temperature from the QCP. We describe the signatures of this NFL behavior in the next section.

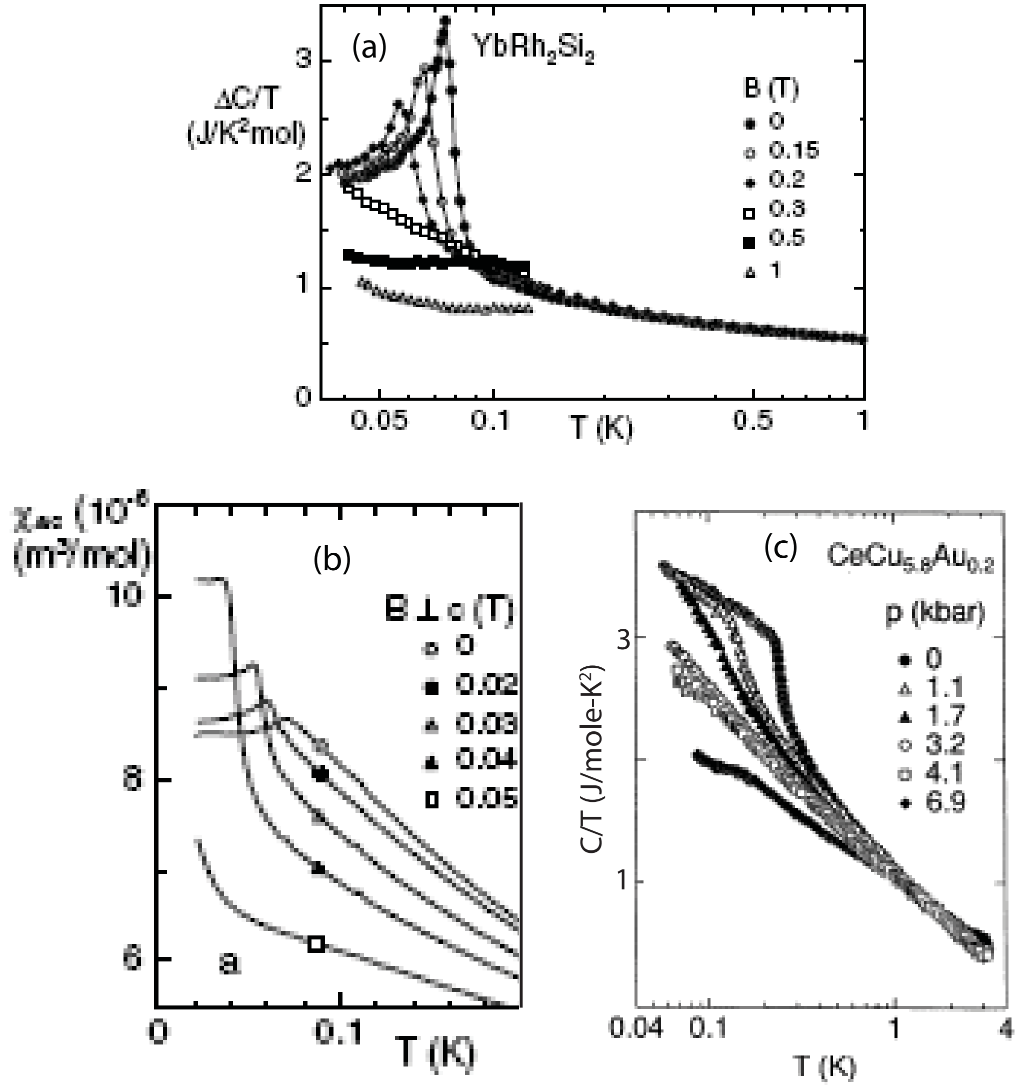

Figure 6.8: (a) A semi-log plot of the temperature dependence of ΔC/T, for $YbRh_2Si_2$ showing the high values of γ. ΔC is the magnetic part of the specific heat minus the specific heat due to the nuclear Schottky peak of Yb at low temperatures. As expected near the QCP, C/T∼logT, and in the higher field FL regime, C/T is a constant (Figure from Gegenwart et al, 2002 as referenced in the text). (b) The temperature dependence of the magnetic susceptibility in different magnetic fields for $YbRh_2Si_2$, showing the very high values of χ_0, as expected for a heavy fermion compound (Figure from Gegenwart et al, 2002 as referenced in the text). (c) A semi-log plot of the temperature dependence of C/T for $CeCu_{5.8}Au_{0.2}$, showing the very high values of between 2 and 4 J/mole-K^2. The temperature dependence of C/T ∼logT illustrating the NFL behavior expected near the QCP. beyond the QCP, at 6.9 kbar, the temperature dependence is nearly constant, consistent with the conventional FL state at higher pressures (Figure from von Lohneysen, 1996 as referenced in the text).

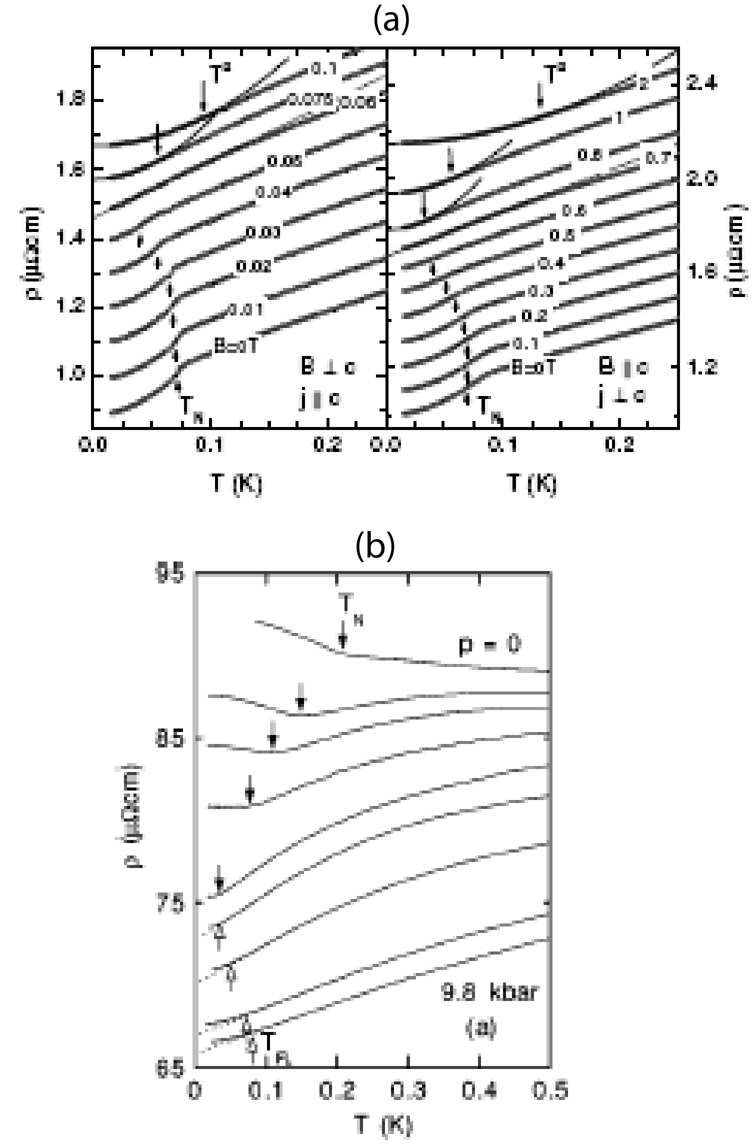

Figure 6.9: (a) The temperature dependence of the resistivity for $YbRh_2Si_2$ for field orientations applied perpendicular to the c-axis of the crystal (left) and parallel to the c-axis of the crystal (right), where the arrows mark the position in temperature where the resistivity deviates from a quadratic (FL) temperature dependence. The expected linear (NFL) temperature dependence extending up in temperature from the QCP is also observed in the data set with no arrow present, which is roughly at the QCP (Figure from Gegenwart, 2002 as referenced in the text). (b) The same type of plot as is shown in (a), with the arrows marking where the temperature dependence of the resistivity for $CeCu_{5.8}Au_{0.2}$ deviates from quadratic. The NFL linear temperature dependence of the resistivity is also observed in the data sets with the hollow arrowheads, just above the FL line (Figure from von Lonhneysen, 1996 as referenced in the text).

6.1.7 Signatures of Quantum Critical Non-Fermi Liquid Behavior

We have discussed how much of the motivation for studying quantum criticality stems from the observation of a universal NFL behavior found in heavy fermion systems with second order antiferromagnetic phase transitions that can be tuned to a QCP. There are measurable signatures of the NFL state in this type of QCP material (Fig. 6.3) [13, 15]. The temperature dependences of ρ(T), C(T), and χ(T) predicted by Fermi liquid theory are no longer observed. Instead, it is observed that $\rho \sim$T, C$\sim$TlnT, and $\chi \sim$T$^{-\delta}$, where δ is small. This behavior is observed in known quantum critical second order antiferromagnetic systems such as $YbRh_2Si_2$ and $CeCu_{5.8}Au_{0.2}$ near the quantum critical point. While anomalous "NFL" is observed in itinerant ferromagnetic systems including MnSi [13] and in the unconventional superconductor, $CePd_2Si_2$, the experimental signatures are different from those of $YbRh_2Si_2$ and $CeCu_{5.8}Au_{0.2}$. The temperature dependence of the resistivity extending upward from the the QCP in MnSi for example is not linear, but $\rho \propto$T$^{3/2}$ [13] and for $CePd_2Si_2$ there is a quasi-linear temperature dependence, $\rho \propto$T$^{1.2}$ [11]. Another difference in the itinerant ferromagnetic systems is the lack of a FL region with $\rho \propto$T^2.

Anomalous "NFL" behavior varies among quantum critical systems and seems to depend on the type and form of magnetic order that is suppressed to form the QCP. Local moment systems show different behavior from itinerant systems, antiferromagnetic systems differ from ferromagnetic systems, and systems with a second order phase transition differ from systems with ferromagnetic order. We will show that Yb_3Pt_4 is unique among quantum critical systems, with no NFL behavior observed near the QCP.

6.1.8 The H-T Phase Diagram for Yb_3Pt_4

The Phase diagram for Yb_3Pt_4 (Fig. 6.10) is unique among quantum critical antiferromagnets. While the previously measured quantum critical heavy fermion antiferromagnets show an entirely second order phase line for the antiferromagnetic phase, Yb_3Pt_4 has a first order phase transition in zero field with T_N=2.4 K. T_N decreases with increasing magnetic field and is driven to a critical endpoint (CEP) at 1.2 K and 1.5 T. Further increasing the magnetic field continues to decrease T_N, with the phase line extending to a QCP near 1.6 T, but as a second order phase line. The ordered phase is a Fermi liquid, and there is a second Fermi liquid region in high fields. In the high field FL region, the crossover line does not terminate at the QCP as it does in the other quantum critical antiferromagnets, but instead has a minimum near the CEP. There is no evidence for NFL behavior extending upward from the QCP, or anywhere else in Yb_3Pt_4. Later, the details of the measurements leading to the construction of the phase diagram for Yb_3Pt_4 will be presented.

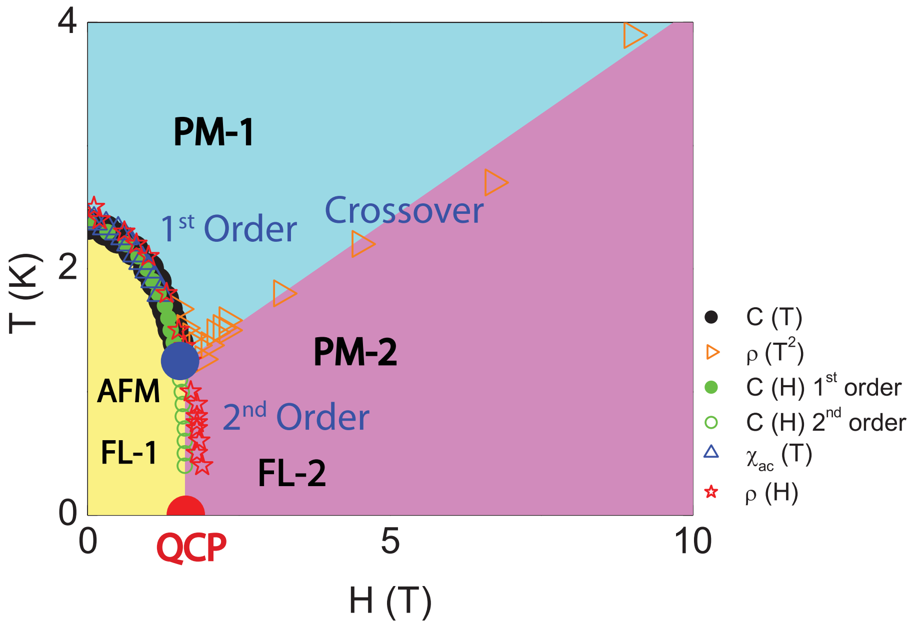

Figure 6.10: The H-T phase diagram for Yb_3Pt_4 based on the data indicated in the key.

Before constructing the phase diagram for any newly grown material, a number of standard exploratory measurements are performed to determine whether the material has the potential to have a quantum critical point and if it does, to thoroughly characterize its zero field properties. We perform these measurements of "the basic properties of Yb_3Pt_4" in the following section. The most important feature is the observation in multiple measurements of a low temperature transition to a magnetically ordered phase. It will be shown in the following sections that Yb_3Pt_4 displays this feature, showing a transition to an antiferromagnetic phase at T_N=2.4 K observed in measurements of the magnetization, AC magnetic susceptibility, heat capacity and resistivity. With the potential for quantum criticality apparent in Yb_3Pt_4, the zero-field properties are thoroughly measured and analyzed in anticipation of a careful analysis of how they evolve with increasing magnetic field.

6.2 The Basic Properties of Yb_3Pt_4

In this section, we present the basic properties of Yb_3Pt_4 based on the zero-field resistance, magnetic susceptibility, heat capacity measurements and the field dependence of the magnetization at different temperatures. These results show that Yb_3Pt_4 has an unusual transition from a local moment paramagnetic phase to a weak antiferromagnetic phase in a FL state via a first order phase transition at 2.4 K. AC magnetic susceptibility measurements suggest that this zero field transition is antiferromagnetic. Powder neutron diffraction measurements confirm that Yb_3Pt_4 is an antiferromagnet with a moment of 1.0 μ_B per Yb atom [88].

6.2.1 The Crystal Structure of Yb_3Pt_4

As described in Chapter 2, single crystals of Yb_3Pt_4 were grown from Pb flux. Polycrystalline Yb_3Pt_4 has been previously studied [89], but we have synthesized single crystals of Yb_3Pt_4 for the first time, and are thus the first to measure its intrinsic physical properties. The single crystals had masses as large as 2 mg, with typical dimensions of $0.2\times0.2\times0.5$ mm^3 (Fig. 6.11). Single crystal X-ray diffraction measurements of a fragment of one of the measured crystals determined that Yb_3Pt_4 crystallizes in a rhombohedral $hR14$ (No. 148) space group with lattice parameters of a = 12.8971 Å, c = 5.6345 Å, and V = 811.65 Å^3, with Z = 6. The structure was solved and refined using the SHELXL-97 program [90]. The atomic coordinates and thermal parameters are listed in table 5.1, and a schematic of the structure is shown in Fig. 6.12. The primitive cell has three Pt positions and just one Yb site symmetry. The full unit cell consists of 18 Yb atoms and 24 Pt atoms. Although Yb_3Pt_4 is overall not a layered system, we show in Fig. 6.12 that some of the Yb atoms form layers of equilateral triangles. These results have been confirmed by powder X-ray diffraction measurements carried out on powders prepared by grinding subsequent batches of Yb_3Pt_4 single crystals.

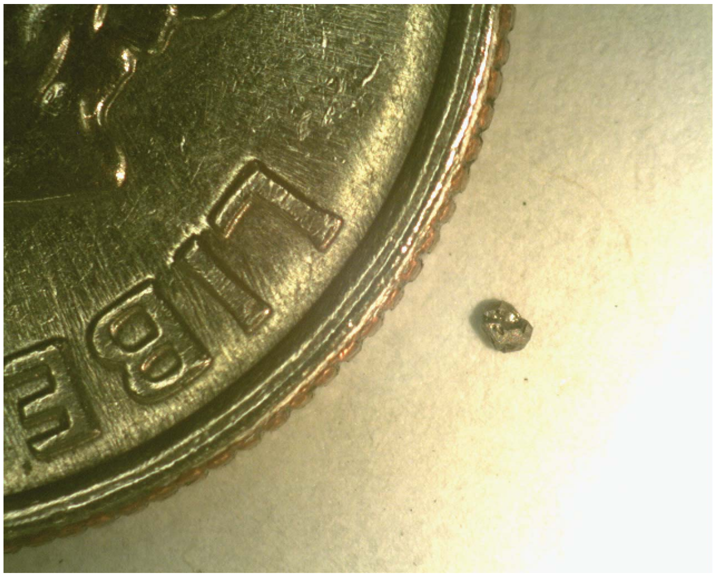

Figure 6.11: A photograph of a single crystal of Yb_3Pt_4 next to a dime.

Table 6.1: Crystallographic data for Yb_3Pt_4.

Atom	Site	x	y	z	$U_eq(\AA^2)$
Pt1	3a	0	0	0	0.00754
Pt2	18f	0.88391	0.28131	0.05311	0.00534
Pt3	3b	0	0	1/2	0.00975
Yb	18f	0.04279	0.21182	0.23494	0.00630

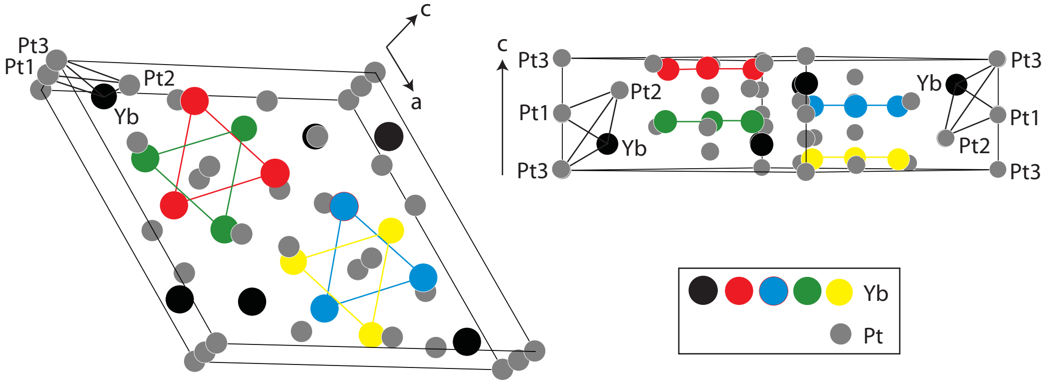

Figure 6.12: Schematic representation of the unit cell with a top view (left) and a side view (right) showing that the Yb atoms form layers of equilateral triangles. The red, blue, green and yellow circles all represent Yb atoms and are used to distinguish between the four equilateral triangles contained in the unit cell.

6.2.2 The Temperature Dependence of the Magnetization

We measured the temperature dependence of the magnetization in a 0.2 T field from 1.8 K to 300 K for two field orientations, parallel and parallel to the a-axis of the crystal and found local moment behavior for most of the temperature range. For both field orientations, the susceptibility increases more and more sharply with decreasing temperature, but with a larger increase when the field is applied parallel to the a-axis (Fig. 6.13a). The anisotropy is well illustrated by measurements of the angle dependence of the magnetization taken on a single crystal of Yb_3Pt_4 mounted on a rotator. We measured the change in magnetization in a 100 G field as we rotate the crystal position with respect to the applied magnetic field from parallel to the c-axis to parallel to the a-axis (Fig. 6.14). We find that the easy magnetic axis lies in the a-b plane of the crystal, with no anisotropy found in this plane. There is no anisotropy ($\chi_\perp/\chi_\parallel = 1$) above ~ 150 K, but below 150 K, the anisotropy increases, reaching a maximum of just over 2 at the lowest temperatures (Fig. 6.13(b)). This value is smaller than the value of approximately 3 implied in Fig. 6.14 and is likely due to misalignment of the crystal with respect to the applied magnetic field.

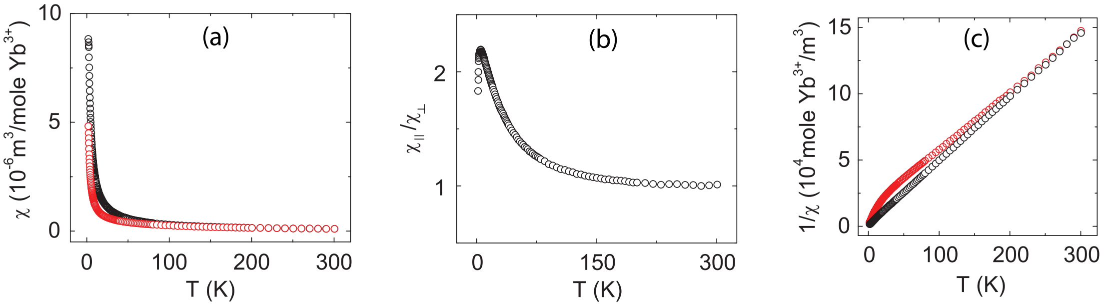

Figure 6.13: (a) The temperature dependence of the DC magnetic susceptibility of Yb_3Pt_4 in a 0.2 T magnetic field applied parallel (red circles), and perpendicular (black circles) to the c-axis of the crystal. (b) The temperature dependence of the anisotropy of the DC magnetic susceptibility, $\chi_\parallel/\chi_\perp$ shows no anisotropy down to 150 K, and a maximum anisotropy of just over 2 at low temperature.

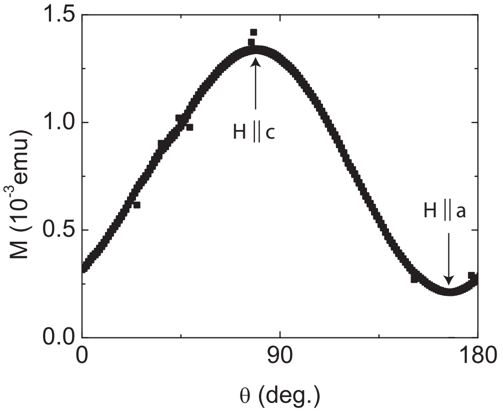

Figure 6.14: The angular dependence of the magnetization of a single crystal of Yb_3Pt_4 at 2 K, in a 100 G field.

The temperature dependence of $1/\chi$ (Figure 6.13(c)) is linear above 150 K for both field orientations, indicating local moment behavior described by the Curie-Weiss expression,

$$\chi_{\parallel,\perp} = C/(T - \theta),$$

where T is the temperature, C is the Curie constant, and θ is the Weiss temperature. A linear fit to $1/\chi_{\perp}$ yields values of θ=-2.3 K, suggesting net antiferromagnetic correlations, and C=4.8×10^{-6}mole Yb^{3+}/m^3K, where,

$$C = g^2\mu_B^2 J(J+1)/3k_B,$$

where the numerator is the effective magnetic moment, μ_{eff}=g$\mu_B\sqrt{J(J+1)}$ squared, g is the Lande g-factor, μ_B is the Bohr magneton, k_B the Boltzmann constant, and J=L+S is the combined intrinsic plus orbital spin. Using the known values for Yb^{3+}, g=8/7 and J=7/2, we obtain an effective moment, μ_{eff}=4.24 μ_B per Yb ion, which is just below the expected Hund's rule moment for Yb^{3+}, 4.54 μ_B. For temperatures below ~150 K, $1/\chi_{\parallel}$ is enhanced relative to $1/\chi_{\perp}$. This could be the result of antiferromagnetic correlations, the crystal electric field splitting of the f-electron states of the Yb ions, or both. At low temperature, there is a slope change at 2.4 K (Fig. 6.15), consistent with a transition to an antiferromagnetic state. The main result of this section is that the Yb moments are trivalent with full CEF occupancy above ~150 K.

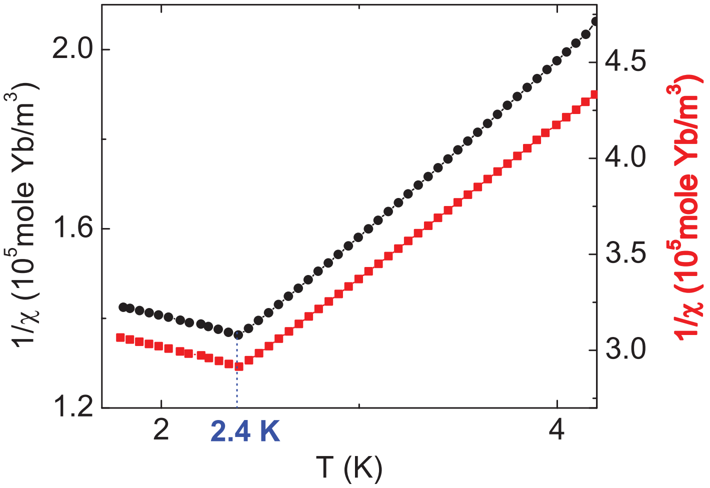

Figure 6.15: The temperature dependence of the inverse dc magnetic susceptibility showing a change in slope at T_N=2.4 K for both $\chi_{\perp}^{-1}$ (black circles) and $\chi_{\parallel}^{-1}$(red squares).

6.2.3 The Temperature Dependence of the AC Magnetic Susceptibility

The temperature dependence of the real part of the zero field ac magnetic susceptibility, χ' (Fig. 6.16), shows a distinct cusp at 2.4 K, indicating that the transition seen in the temperature dependence of the susceptibility (Fig. 6.15) is to an antiferromagnetic state. Also plotted is the derivative, $d\chi'/dT$, which shows a discontinuity at 2.4 K, in agreement with the position of the ordering feature observed in the specific heat. The transition is also seen in the DC magnetic susceptibility data as a change in slope at 2.4 K for both $\chi_{\perp}^{-1}$ and $\chi_{\parallel}^{-1}$ (Fig. 6.15), showing that the antiferromagnetic order develops directly from a local moment paramagnetic state, with no evidence for any significant critical fluctuations. Turning to the measurements of the temperature dependence of the AC magnetic susceptibility, and referring to Fig. 6.16, we find a very high value for the extrapolated zero field susceptibility, χ_0=6.8×10^{-6}m^3/mole Yb. This value is comparable to the highest values found in the heavy fermion materials [87]. We also find that the temperature dependence of χ' in the ordered state is nearly temperature independent, suggesting that it is the

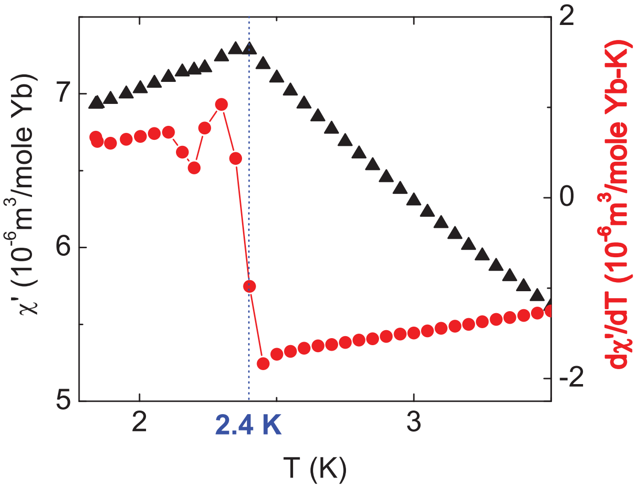

Figure 6.16: The temperature dependence of the ac magnetic susceptibility, χ'_{ac} (black triangles), showing an antiferromagnetic cusp, and a discontinuity in its temperature derivative, dχ'/dT (red circles) at the antiferromagnetic transition temperature, T$_N$=2.4 K.

Pauli susceptibility of a Fermi liquid.

6.2.4 The Field Dependence of the Magnetization

Local moment behavior is also observed in measurements of the field dependence of the magnetization of single crystals of Yb_3Pt_4, taken at temperatures ranging from 1.78 K to 100 K and in fields up to 7 T (Fig. 6.17(a)). At high temperatures, the magnetization is linear with field, but as the temperature is lowered, M increases more and more sharply at low field, then levels off, approaching a maximum value (the saturation magnetization, M_S) of M_S=2.1 μ_B/Yb. A plot of the field dependence of the magnetization for a smaller selection of temperatures is shown in Figure 6.17(b) for clarity. This selection is then re-plotted as a function of H/T (Fig. 6.17(c)). The data collapse onto a single curve, with the low temperature high field magnetization reduced by about a factor of 2 from the expected J=7/2, g=8/7 magnetization expected for an Yb^{3+} based local moment paramagnet, where the magnetization

$$M = NgJ\mu_B B_J(x)$$

where N is the number of Yb^{3+} atoms, g is the Lande factor, and B_J(x) is the Brillouin function,

$$B_J = \frac{2J+1}{2J}coth(\frac{2J+1}{2J}x) - \frac{1}{2J}coth(\frac{x}{2J})$$

where x=gμ_BBJ/k_BT. The wide range of H/T scaling observed in the magnetization of Yb_3Pt_4 shows that local moment magnetism persists down to the lowest temperatures and is not replaced by critical fluctuations. The saturation moment of ~2.1 μ_B/Yb^{3+} is about half of the expected low temperature, high field value of 4.0 μ_B/Yb, but, as shown later, this result is consistent with the crystal electric field splitting of the Yb^{3+} state deduced from specific heat measurements, which breaks the degeneracy of the Yb^{3+} ions. In this section, we have shown further evidence that antiferromagnetic order emerges from a paramagnetic state with nearly ideal local moment behavior.

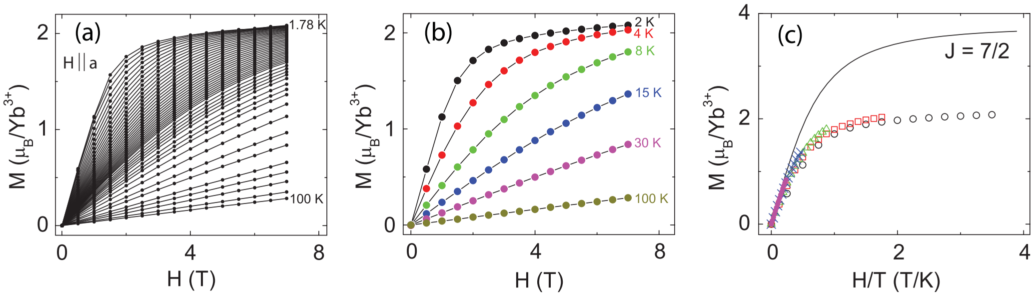

Figure 6.17: (a) The field dependence of the magnetization at temperatures ranging from 1.78 K to 100 K with the field applied parallel to the a-axis of the crystal. At low temperature, the magnetization increases sharply, then levels off, approaching the saturation magnetization, M_{sat}= 2.1 μ_B. (b) The field dependence of the magnetization for a smaller selection of temperatures used in (c) to illustrate the scaling (c) The magnetization plotted as a function of H/T, with the J = 7/2 Brillouin function (black line). The magnetization data are reduced from the J=7/2 Brillouin function because crystal fields lift the degeneracy of the Yb^{3+} ground state.

6.2.5 The Temperature Dependence of the Heat Capacity

In this section, we present the results of our zero-field heat capacity measurements. The temperature dependence of the zero-field heat capacity was measured from 0.38 K to 75 K (Fig. 6.18(a)). Generally, the temperature dependence of the heat capacity is a combination of electronic, magnetic and phonon contributions, with C_{tot}=C_e+C_{mag}+C_{Ph}=C_M+C_{Ph}, where C_M is the combined electronic and magnetic contribution, which depends upon the type of magnetic order and the type of electronic phase. The phonon contribution dominates the heat capacity at intermediate and high temperatures. Fig. 6.18(b) reveals a very sharp feature associated with the antiferromagnetic transition at 2.4 K found in the AC and DC susceptibility measurements. Using the dilution refrigerator insert for the PPMS, we measured the temprature dependence of the heat capacity down to 50 mK (Fig. 6.18(c),(d), black data points) and found that the data agreed with that taken using the ^{3}He insert and revealed an upturn in the temperature dependence at the lowest temperatures associated the nuclear Schottky peak of the Yb atoms.

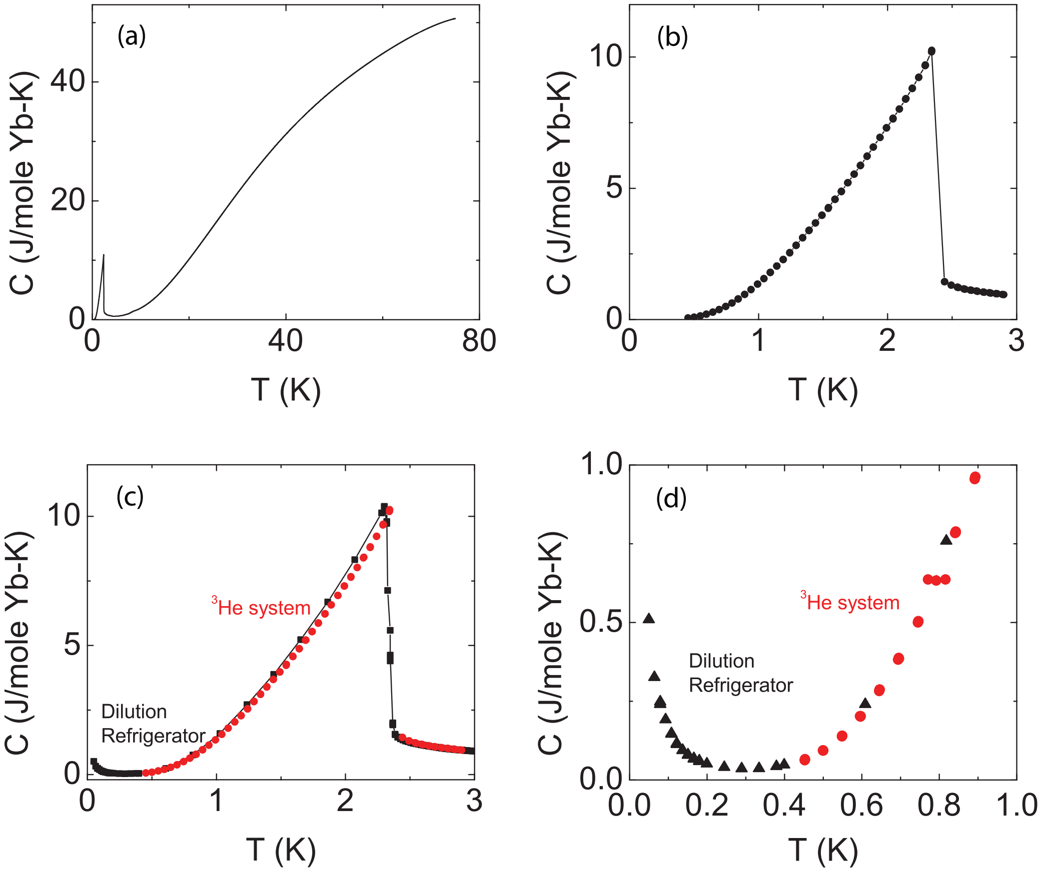

Figure 6.18: (a) The temperature dependence of the heat capacity shows an ordering peak at low temperature and is dominated by the phonon contribution at intermediate and high temperatures. (b) The temperature dependence of the heat capacity near the extremely sharp antiferromagnetic transition at T_N=2.4 K. (c) The temperature dependence of the heat capacity measured in the ^{3}He system (red circles) plotted with the temperature dependence of the heat capacity measured in the dilution refrigerator (black squares), revealing the sharp upturn associated with the nuclear Schottky peak of the Yb atoms at the lowest temperatures. (d) A close-up of the low temperature region of the plot shown in (c) clearly showing the sharp upturn associated with the nuclear Schottky peak of the Yb atoms.

In order to analyze the electronic and magnetic parts of the specific heat, C_M, we need to model and then subtract the phonon contribution, C_{Ph}. The phonon contribution to the specific heat was estimated using the Debye model [5],

$$C_{Ph} = 9nk_B(\frac{T}{\Theta_D})^3 \int_0^{\Theta_D} \frac{x^4 e^x dx}{(e^x - 1)^2}$$

which is then subtracted from the total heat capacity to isolate C_M=C-C_{Ph} (Fig. 6.19, blue line). A close-up view of the temperature dependence of C_M is plotted in Figure 6.19(b), and reveals a broad Schottky-like feature peaked near 26 K. The crystal field splitting scheme is confirmed by a good fit of the data to the Schottky expression,

$$C = \frac{\sum_i E_i e^{-\frac{E_i}{k_B T}}}{\sum_i e^{-\frac{E_i}{k_B T}}}$$

which finds a second doublet, E_1=50 K, and a third doublet, E_2=127 K. To obtain the entropy, S, at some given temperature, T (Fig. 6.20(a), red dashed line), a plot of C/T versus T is numerically integrated using

$$S(T) = \int_0^T \frac{C}{T'} dT'$$

To determine the entropy associated with the magnetic ground state and the excited crystal field states, the specific heat and entropy are plotted together in a composite plot (Fig. 6.20(a)) along with a Schottky fit to the broad crystal electric field feature (Fig. 6.20(a), blue dotted line). The entropy reaches a value of Rln2 just after the large anomaly in the specific heat (Fig. 6.20(a), red dashed line), indicating that the magnetic ground state is a doublet. S reaches Rln4 after the first Schottky peak, indicating that the eight degenerate states of the J=7/2 Yb^{3+} are split by the crystal electric field, into 4 doublet states, as expected for the symmetry of the Yb structure (Fig. 6.20(b)) [91].

Also obtained from a plot of C/T versus T is the coefficient of the electronic part of the heat capacity at T=0, γ. Since the electronic part of the heat capacity is given by C_e= γT, this is easily obtained by plotting C/T versus T, and extrapolating the data to T=0. This analysis yields an extremely low value for γ, which suggests very little mass enhancement of the quasiparticles.

Careful analysis shows that the phase transition is weakly first order. Fig. 6.21 is a plot of the raw temperature versus time data during the decay cycle taken at the phase transition, T_N=2.4 K. As explained in the chapter on experimental technique, the heat flow during the decay cycle can be estimated using the heat flow equation, $dQ/dT=K_W\Delta T$, where K_W is the thermal conductance through the platform wires, which is calculated by the PPMS at each temperature and is approximately 5×10^{-7}J/sec-K and ΔT is the difference between the initial temperature and the time dependent temperature. The latent heat is estimated by multiplying the power by the length of time the raw data remains in the non-linear region. We estimate a latent heat of just $\sim2.17\times10^{-4}$J/g, or 0.09 J/mole Yb. For comparison, Table 5.2 lists other rare-earth elements and rare-earth based compounds with first order magnetic phase transitions. Clearly, Yb_3Pt_4 is very weakly first order.

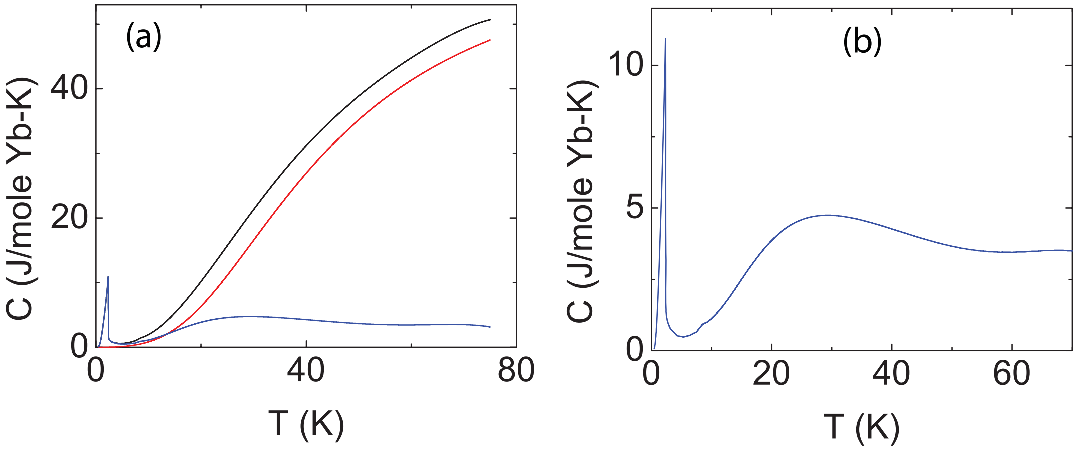

Figure 6.19: (a) The temperature dependence of the specific for temperatures ranging from 0.38 K to 75 K, where the estimated phonon heat capacity (red line) is subtracted from the total heat capacity (black line), isolating the magnetic part of the heat capacity (blue line. (b) A close up of the temperature dependence of the specific heat for temperatures ranging from 0.38 K to 75 K for the magnetic part of the heat capacity, C_M. The sharp ordering anomaly at low temperatures is followed by a broad Schottky-like feature at the higher temperatures.

We found that the temperature dependence of C_M/T in the ordered state has a significant contribution from a Schottky peak originating with the exchange splitting

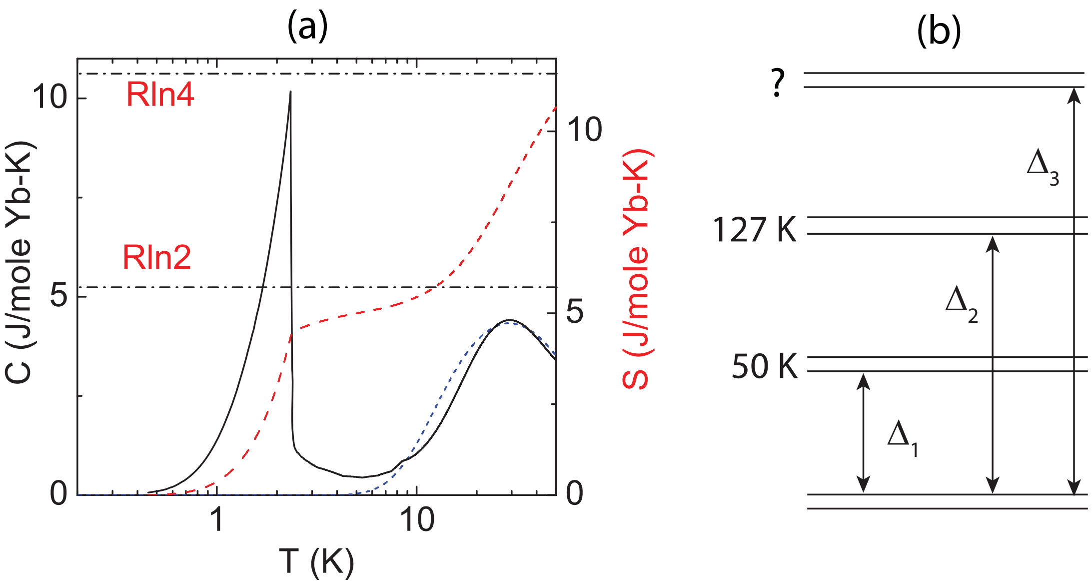

Figure 6.20: (a) A composite plot containing the temperature dependence of the specific heat (solid line), with its associated entropy (red dashed line), and a good fit to the broad feature in the specific heat using the expression for Schottky anomaly (blue dotted line). (b) A schematic of the first three doublet energy levels for the crystal field splitting of the rhombohedral Yb structure.

Table 6.2: Latent heat and critical temperature of first order ferromagnetic or antiferromagnetic transitions in some rare earth elements, and rare earth based compounds.

Compound	T_C(K), T_N(K)	$L(J/moleRE)$	Ref.
Dy	$91(FM)$	39	[92]
Er	$19(FM)$	24	[93]
$Er_{0.4}Ho_{0.6}Rh_4B_4$	$1.9(FM)$	74.5	[94]
Sm_2IrIn_8	$14(AFM)$	5	[95]
$Sm_{0.55}Sr_{0.45}MnO_3$	$130(FM)$	180	[96]
Yb_3Pt_4	$2.4(AFM)$	0.09	this work

of the doublet ground state. We have added the estimated Schottky anomaly to the plot (Fig. 6.22, dashed magenta line) assuming that the doublet ground state is split. We are unable to determine an exact value for the energy splitting of the exchange split doublet, however, because there are likely multiple contributions to the heat capacity in the ordered state and we thus can only estimate a best fit to a Schottky anomaly. We will, however, show later that measurements of the temperature dependence of the heat capacity in large magnetic fields is consistent with the presence of a Schottky anomaly resulting from the increased Zeeman splitting of the exchange

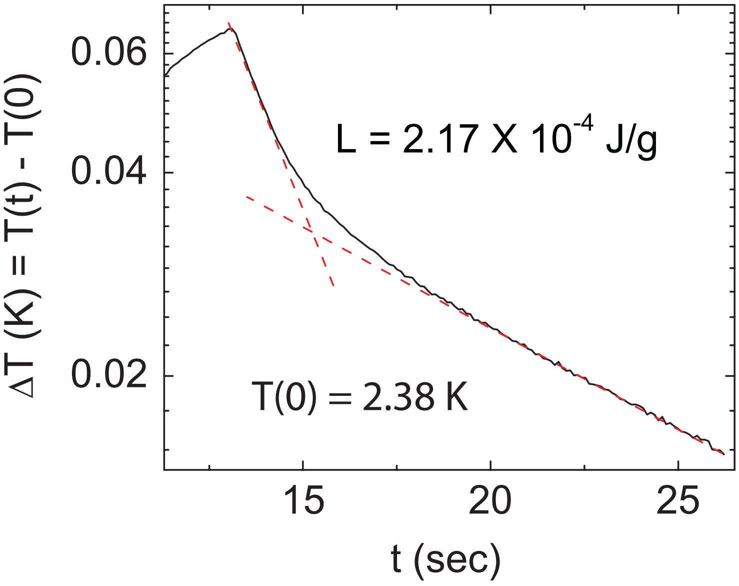

Figure 6.21: The time dependence of the difference between the time dependent temperature, T(t) and the initial temperature, T(0), of the raw heat capacity data taken near T_N=2.4 K during the decay cycle plotted on a semi-log plot. The two linear regions represent the value of the heat capacity on either side of T_N. The region in between is non-linear because there is a latent heat of ~2.17×10^{-4}J/g present.

split doublet ground state with increasing magnetic field.

We initially considered the possibility that the heat capacity in the ordered state may be due to a magnetic spin wave, but rejected this scenario after failing to find a good fit to the data using the expression for a gapped spin wave. We show the results of these fits in Fig. 6.22, where we compare fits for gapped ferromagnetic and antiferromagnetic spin waves in the ordered state, using

$$C_M/T = T^n e^{-\Delta/k_B T},$$

where k_B is the Boltzmann constant, Δ is the spin wave energy gap, and n=2 for and antiferromagnetic spin wave and n=0.5 for a ferromagnetic spin wave [97]. We found that the best fit to the data is for n=0, but we know of no mechanism that would lead to this relation.

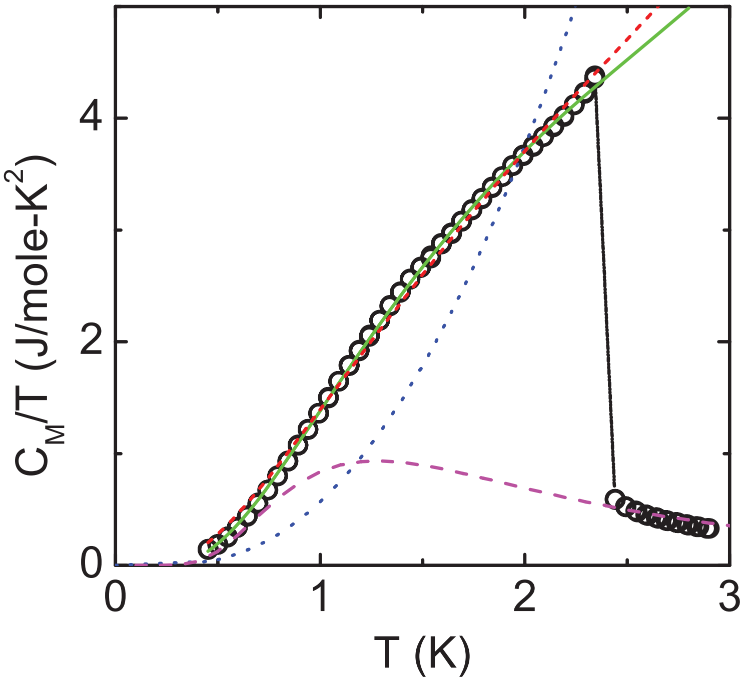

Figure 6.22: The temperature dependence of C_M/T (black circles) is fit to the expression for a ferromagnetic spin wave with a gap, $C_M/T=\gamma+AT^{0.5}e^{-\delta/T}$ (red dashed line), where A=3.3 J/mole-Yb-$K^{5/2}$, $\delta=\Delta/k_B=4.1$ K, where Δ is the spin wave energy gap. The blue dotted line is a fit to an antiferromagnetic spin wave, $C_M/T=\gamma+AT^2e^{-\delta/T}$ assuming a 1 K gap. In both cases, the coefficient of the specific heat, γ is found to be negligible. The best fit to the data in the ordered phase is to $C_M/T=\gamma+AT^0e^{-\delta/T}$ (solid green line). The dashed magenta line is the expected Schottky anomaly if the doublet ground state is split.

6.2.6 The Temperature Dependence of the Resistivity

Measurements of the temperature dependence of the resistivity, ρ(T), of a single crystal of Yb_3Pt_4 (Fig. 6.23(a)) show metallic behavior, with ρ(T) decreasing with decreasing temperature and reaching a minimum value of ρ_0=21$\mu\Omega$-cm at 0.38 K from a 300 K value of 108 $\mu\Omega$-cm. Fig. 6.23(b) shows a sudden change in slope at the transition temperature, T_N=2.4 K, where ρ(T) drops ~25% from ρ(2.4K) to ρ(0). The sudden drop in ρ at the lowest temperatures is caused by the loss of spin disorder scattering due to antiferromagnetic order below T_N=2.4 K. Re-plotting the low temperature data as

$$\rho - \rho(0) = AT^2$$

(Fig. 6.23(c)) reveals a quadratic temperature dependence of the ordered state, indicating that it is a Fermi liquid, with the large coefficient, A=1.7 $\mu\Omega$-cm/K^2, which would be consistent with a large quasiparticle effective mass, characteristic of heavy Fermion compounds. As previously discussed, materials classified as heavy fermions have been shown to obey the Kadowaki-Woods relation, A/γ^2=10$\mu\Omega$-cm-

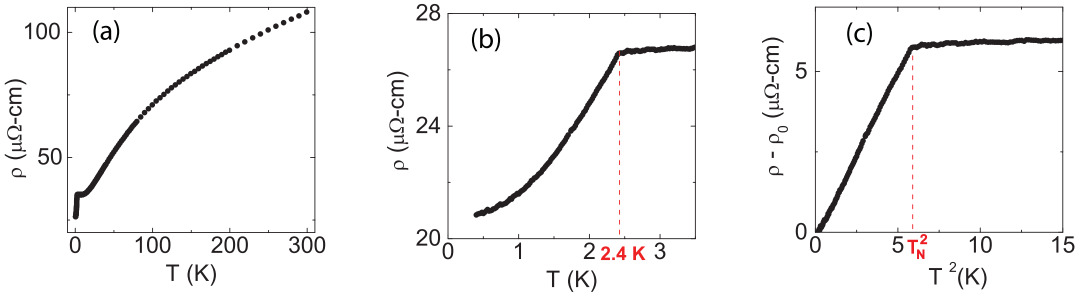

Figure 6.23: (a) The temperature dependence of the resistivity for a single crystal of Yb_3Pt_4 from 0.38 K to 300 K. The sudden drop in the resistivity at the lowest temperatures is associated with a transition to an antiferromagnetic phase. (b) The temperature dependence of the resistivity near T_N=2.4 K. The sudden decrease in spin disorder scattering upon entering the antiferromagnetic state results in a drop in the resistivity (c) $\Delta\rho$=$\rho - \rho_0$ plotted as a function of T^2. The temperature dependence is quadratic below T_N = 2.4 K indicating that the ordered low temperature phase is a Fermi liquid. The slope of the linear fit is 1.7 $\mu\Omega$-cm/K^2, indicating that Yb_3Pt_4 is a heavy fermion.

mole^{2}K^2/J^2 [75]. While the very large value of A=1.7 $\mu\Omega$-cm/K^2 is similar to that of UPt$_3$ and comparable to values found in other heavy fermion materials (Fig. 6.24), γ is extremely small, so we can not ascribe large values of A and χ_0 to a large value of m*. We can not classify Yb$_3$Pt$_4$ as a heavy fermion. We considered the possibility that there is significant reduction in the quasi-particle concentration associated with the magnetic transition at 2.4 K, but recent Hall voltage measurements of Yb$_3$Pt$_4$ do not show any change in electron concentration at T$_N$ [98]. The two known quantum critical systems, YbRh$_2$Si$_2$ and CeCu$_{6-x}$Au$_x$ both show values of A and γ among the highest found, showing that the quasiparticles are very strongly scattered relative to other heavy fermion systems. The value of A for Yb$_3$Pt$_4$ in zero field is comparable, as indicated in Fig. 6.25, but it does not obey the Kadowaki-Woods relation because of the very small value of γ. In 9 T, however, Yb$_3$Pt$_4$ does obey the Kadowaki-Woods relation, showing values of A and γ comparable to UPt$_2$.

Since the ordered state is a Fermi liquid, we can use the Sommerfeld-Wilson ratio, R$_W$=π^2k$_B^2\chi_o/\mu_{eff}^2\gamma$ to determine the strength of magnetic correlations. As previously discussed, in most cases R$_W$=1 for a non-interacting system, R$_W$ <2 for superconducting compounds and R$_W$ >2 for more strongly interacting magnetic systems. We want to see how Yb$_3$Pt$_4$ compares with other previously measured heavy fermions that experience magnetic interactions. For Pd, R$_W$=6-8 [99], for YbAgGe, R$_W$=2 [100], for YbRh$_2$Si$_2$, R$_W$=13 [73], and for SrRu$_2$O$_7$, R$_W$=10 [101]. Fig. 6.25 [87] is a plot of γ versus χ_0 for some know heavy fermion compounds. We have added the zero field and 9 T values for Yb$_3$Pt$_4$. In zero field, Yb$_3$Pt$_4$ has an extremely high value of χ_0, but a very small value of γ, yielding a very high value of R$_W$, over 1000, showing that it is completely different from the typical heavy fermion compounds shown in the plot. At 9 T (red circle), however, Yb$_3$Pt$_4$ is comparable

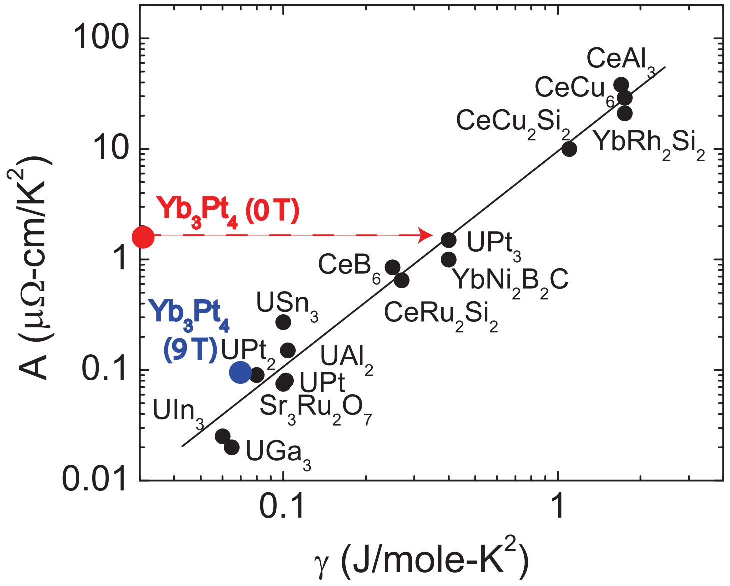

Figure 6.24: A log-log plot of A vs. γ, illustrating the Kadowaki-Woods relation. The horizontal red dashed line shows that the coefficient of the quadratic part of the resistivity for Yb_3Pt_4 in zero field (red circle) is comparable to that of UPt_3, but it does not obey the Kadowaki-Woods relation, because of the very small value of γ. In a 9 T field Yb_3Pt_4 has values of A and γ comparable to those of UPt_2 and has a Kadowaki-Woods ratio consistent with that expected for a heavy fermion material (blue circle). Both of the quantum critical systems previously discussed, $YbRh_2Si_2$ and $CeCu_6$ have very large values of γ and A, because of their very large effective masses. The data for the heavy fermion compounds shown in the plot was obtained from Kadowaki, 1986 and Tsujii, 2003 as cited in the text.

to other known heavy fermion compounds, yielding a value of just over 1, showing that at high magnetic fields it is a weakly interacting Fermi liquid.

We observed a Fisher-Langer relation between the temperature dependences of the specific heat, $C_M(T)$, and the derivative of the temperature dependence of the resistivity, $d\rho/dT(T)$ in the magnetically ordered state [102] (Fig. 6.26). The Fisher-Langer relation predicts that $C_M(T)$ and $d\rho/dT$ should be proportional if the fluctuations in the magnetization are dominantly antiferromagnetic [102]. The observation of the Fisher-Langer relation in Yb_3Pt_4 indicates that antiferromagnetic fluctuations are stronger than ferromagnetic fluctuations around and in the ordered state, which is consistent with the weak cusp observed at T_N in the temperature dependence of the zero field AC magnetic susceptibility.

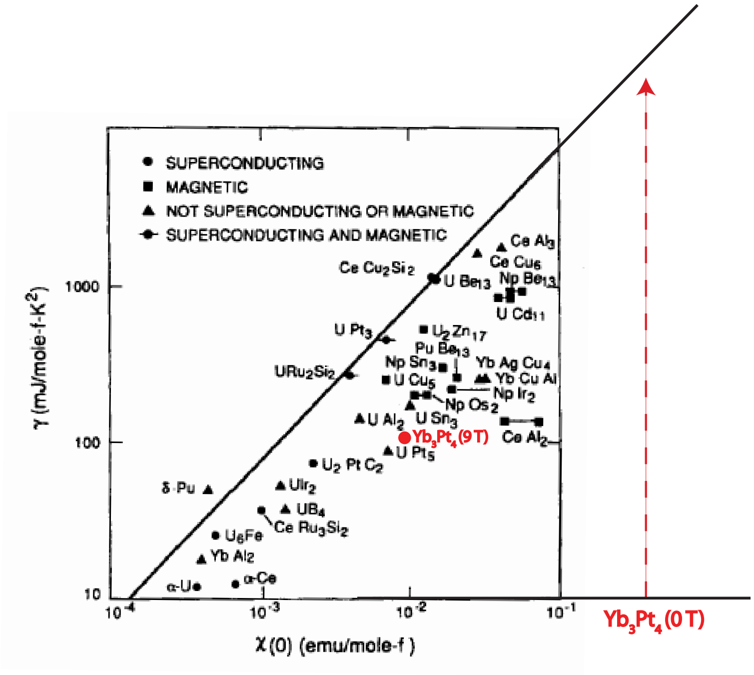

Figure 6.25: A plot of γ versus χ_0 for some known heavy fermion compounds. In zero field, Yb_3Pt_4 has the largest value of χ_0 among the plotted compounds, but has a very small value of γ, placing it well below the range of the plot. The red dashed line indicates where Yb_3Pt_4 would lie on the plot based only on its value of χ_0. In a 9 T field, it has values of χ_0 and γ comparable to UPt_5 and fits in well with the other heavy fermion compounds (Figure from Fisk, 1987 as referenced in the text).

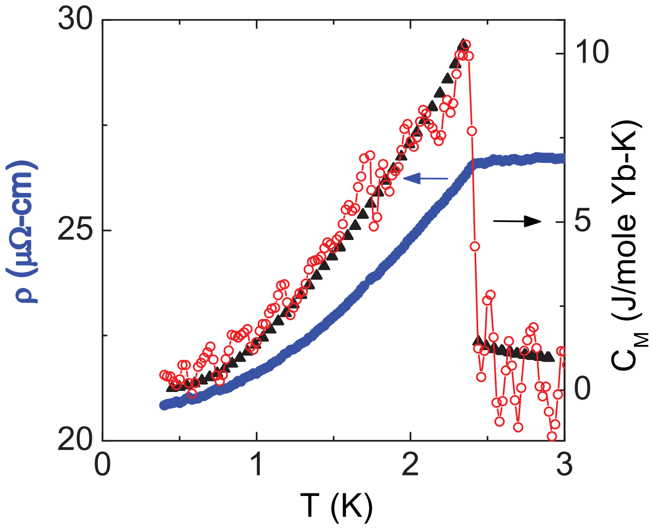

Figure 6.26: A plot of the temperature dependence of the resistivity, ρ(T) (blue circles), and its derivative, dρ/dT (red circles), compared with the temperature dependence of the specific heat divided by temperature, C_M/T (black triangles) near the transition temperature, T_N.

6.2.7 Analysis of the Magnetically Ordered State

Recent powder neutron diffraction measurements [88] confirm that Yb_3Pt_4 orders antiferromagnetically. The magnetic structure was solved assuming that each Yb ion hosts a localized moment, with pairs of nearest neighbor spins interacting antiferromagnetically (Fig. 6.28). The magnetic diffraction pattern was obtained from the difference between neutron powder patterns above and below T_N (Fig. 6.27(a)) and the magnetic structure was solved using representation symmetry analysis. The moment on the Yb site was determined to be $\sim 1\mu_B$ and the temperature dependence of the primary magnetic peak is shown in Fig. 6.27(b). Based on previous measurements of the temperature dependence of the magnetization, we find 1.4 μ_B per Yb in the paramagnetic phase at temperatures just above T_N and extending right down to T_N (Fig. 6.15). This is in fairly good agreement with the value of $1\mu_B$ found in the ordered state just below T_N. This slightly lower value in the magnetically ordered state could be due to the exchange splitting of the doublet ground state. In the next section we show, based on measurements of the temperature dependence of the heat capacity in different magnetic fields, that the doublet ground state in Yb_3Pt_4 is split by the applied magnetic field, with the magnitude of the splitting increasing with increasing magnetic field as expected.

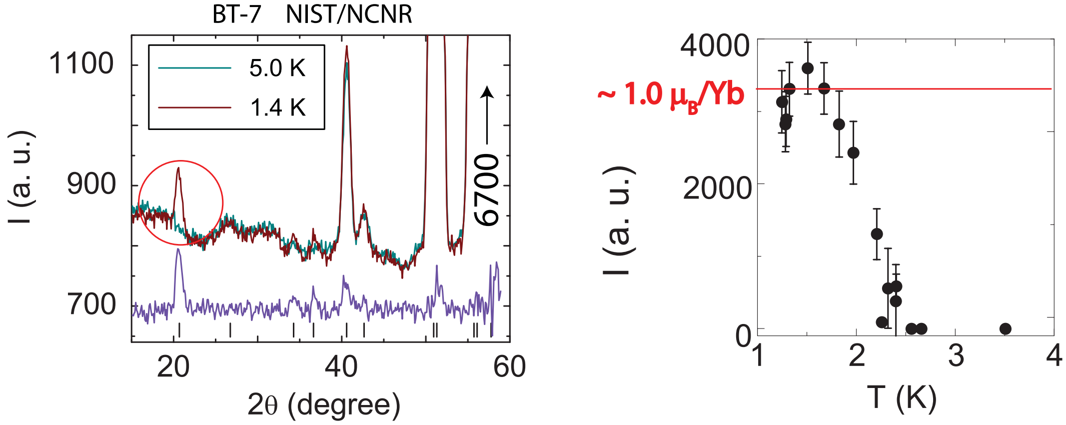

Figure 6.27: (a) The neutron intensity plotted as a function of angle at 5 K (above T_N) and 1.4 K (below T_N)(b) The intensity of the main magnetic peak plotted as a function of temperature. Analysis results indicate an effective moment of 1.0 μ_B per Yb ion (Figure courtesy of P. Stephens).

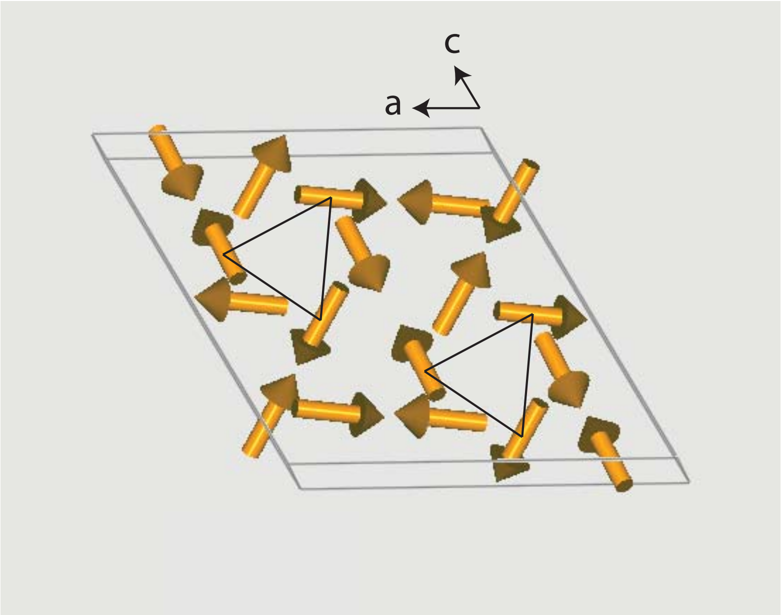

Figure 6.28: (A schematic of the solved magnetic structure for the antiferromagnetically ordered phase of Yb_3Pt_4 (Figure courtesy of Y. Janssen).

6.2.8 Initial Conclusions

Our initial results are that Yb_3Pt_4 orders antiferromagnetically and becomes a Fermi liquid at T_N=2.4 K, and has some weak magnetic anisotropy. The presence of a latent heat, measured from the raw heat capacity data shows that the antiferromagnetic transition is weakly first order. Also, the measurements of the temperature dependence of the heat capacity and the magnetic susceptibility do not show significant critical fluctuations. Powder neutron diffraction measurements [88] have confirmed the antiferromagnetic structure of Yb_3Pt_4, the Fisher-Langer relation observed between C(T) and dρ(T)/dT suggests that antiferromagnetic fluctuations are dominant, but while weak, there may also be a net ferromagnetic component. The underlying Schottky anomaly from the Zeeman splitting of the doublet ground state make it difficult to determine, separate and fit all the components of the specific heat. However, we believe that the Sommerfeld coefficient is very small in the ordered state.

The most remarkable result is that the magnetic ordering enables the formation of a Fermi liquid. Our results indicate that the magnetic phase transition is from a local moment paramagnet to an antiferromagnet, with at best weak coupling between the local magnetic moments and the conduction electrons. There is little evidence for the Kondo effect in zero field, universally present in the known heavy fermion quantum critical systems. At 21$\mu\Omega$-cm, the base temperature resistivity is also high compared with other quantum critical metals, but the significant drop in resistivity at T_N suggests that the high resistivity is not the result of impurity scattering, but of quasiparticle scattering from magnetization fluctuations. Considering the weak coupling between conduction electrons and local magnetic moments combined with the extremely small value of γ, it is surprising to find that the the ordered state shows the resistivity of a Fermi liquid, with ρ=ρ_0+AT^2, with the very high value of A= 1.7 Ω-cm/K^2, which is similar to values found in heavy fermion systems.

The low ordering temperature of T$_N$=2.4 K automatically makes Yb$_3$Pt$_4$ a good potentially quantum critical candidate. We need only to attempt to decrease T$_N$ via pressure or magnetic field to see if it can be tuned to a QCP. On a deeper level, in order to gain a better understanding of the different mechanisms at play in different types of quantum critical systems, we need to be able to classify the phase transition based on order type, and how the electronic and/or crystal structures are affected by the development of magnetic order and other underlying mechanisms. We know that the magnetic phase transition is antiferromagnetic and weakly first order, but it is not clear whether the phase transition is a local moment type of transition, or if it originates with a Fermi surface instability. We do know from recent Hall voltage measurements [98] that there is not a change in the electron density going from the paramagnetic phase at higher temperatures to the antiferromagnetic phase at lower temperatures, suggesting that there is not a significant change in the number of electrons contained in the Fermi surface. The development of Fermi liquid behavior exactly at T$_N$ is unusual and suggests significant and perhaps a novel type of modification to the Fermi surface. Powder neutron diffraction measurements show that we have a antiferromagnetic order that can be modeled assuming local magnetic moments [88], but we are unsure about what role the itinerant electrons play in the magnetic order. In the next section, we tune T$_N$ to a QCP by applying a magnetic field and based on the field and temperature dependences of the heat capacity, resistivity, magnetization and the AC magnetic susceptibility, we build a magnetic field-temperature (H-T) phase diagram.

6.3 The Construction of an H-T Phase Diagram for Yb_3Pt_4

The initial measurements presented in the previous section showed that Yb_3Pt_4 holds great promise as a potential host for quantum criticality and its associated non-Fermi liquid behavior. After the initial measurements, our strategy was to use magnetic field to suppress T_N from 2.4 K to 0 K at some finite achievable field, revealing the quantum critical phenomena in Yb_3Pt_4. In this section, we show that T_N can indeed be driven to a QCP (T_N=0) with an applied magnetic field of 1.6 T. Based on extensive in-field measurements of the specific heat, resistivity, and magnetic susceptibility, we construct an H-T phase diagram for Yb_3Pt_4 at fields up to 9 T. Measurements of the temperature dependence of the heat capacity in different magnetic fields show that the first order phase transition in zero field at 2.4 K terminates at a critical endpoint at 1.2 K, 1.5 T when the field applied parallel to the a-axis of the crystal. We find some anisotropy, with the critical endpoint occurring at 1.2 K, 3.5 T when the field is applied parallel to the c-axis of the crystal. Measurements of the magnetoresistance and of the field dependence of the specific heat show that the phase line continues downward in temperature with increasing magnetic field to a QCP at 1.6 T, but as a second order phase transition.

6.3.1 The Temperature Dependence of the Specific Heat in a Magnetic Field

This section describes the evolution of the temperature dependence of the heat capacity with increasing magnetic field, and begins the construction of a magnetic field-temperature (H-T) phase diagram. Fig. 6.29(a) is a plot of the full data set of the temperature dependence of the specific heat in magnetic fields ranging from zero to 9 T, with the field applied parallel to the a-axis of the crystal. In Fig. 6.29(b), we focus on the sharp ordering anomaly at low temperatures to illustrate the effects of the magnetic field on the position and shape of the ordering anomaly. Both the position of the peak, T_N, and its magnitude, ΔC, decrease with increasing magnetic field and eventually the sharp ordering anomaly is gone and only the broad maximum in the background remains. This broad maximum moves upward in temperature with increasing magnetic field, suggesting that it is a Schottky anomaly with an energy originating with the Zeeman splitting of the doublet ground state. We consider this possibility and provide a more detailed analysis in section 5.4. In Fig. 6.30(a), we have plotted the temperature dependence of the specific heat in different magnetic fields, with the field applied parallel to the c-axis of the crystal and it too shows a decrease with increasing fields in both ΔC and T_C. Also shown in Fig. 6.30(a) are graphical definitions of ΔC and T_C. To lay the foundation for our H-T phase diagram, we have plotted the field dependence of T_N, revealing the phase line of the antiferromagnetic state. As discussed previously, the zero field transition at 2.4 K is a weakly first order phase transition with a latent heat of 0.09 J/mole Yb (Fig. 6.31). As the applied magnetic field is increased, however, the transition loses its first order character (Fig. 6.29(b)), resembling a second order phase transition beyond 1.5 T. For the perpendicular configuration, the first order phase line ends at 1.2 K, and 1.5 T, indicating the presence of a critical endpoint (Fig. 6.30(b)). The results for the parallel field configuration are similar, but the phase line ends at 1.2 K, and 3.5 T (Fig. 6.30(b)). In the next section, we present the results of measurements of the field dependence of the latent heat, obtained by examining the raw temperature versus time heat capacity data.

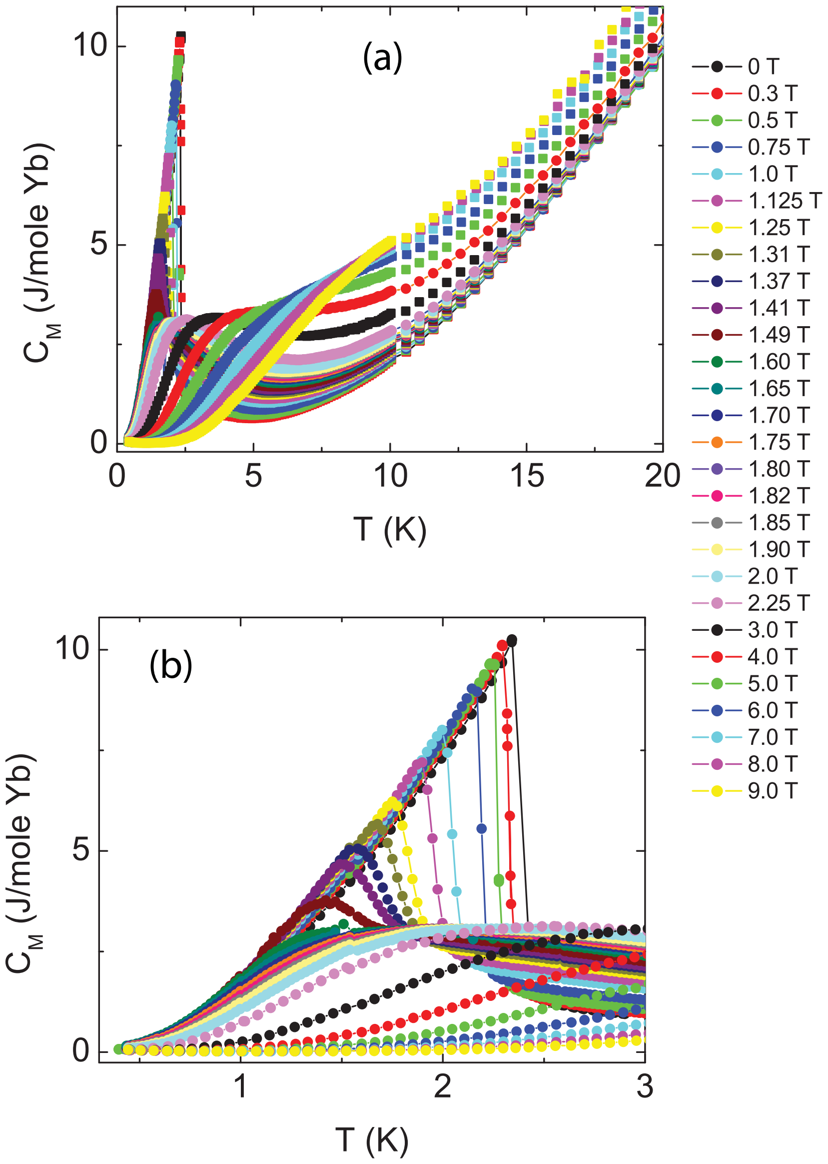

Figure 6.29: (a) The temperature dependence of the specific heat in different magnetic fields for temperatures up to 20 K. The sharp feature at low temperature marks the phase transition to the antiferromagnetic state. There is also a broad maximum at slightly higher temperatures(b) The same plot described in (a), but zooming in on the low temperature region to show the details of the ordering anomaly associated with the antiferromagnetic phase transition.

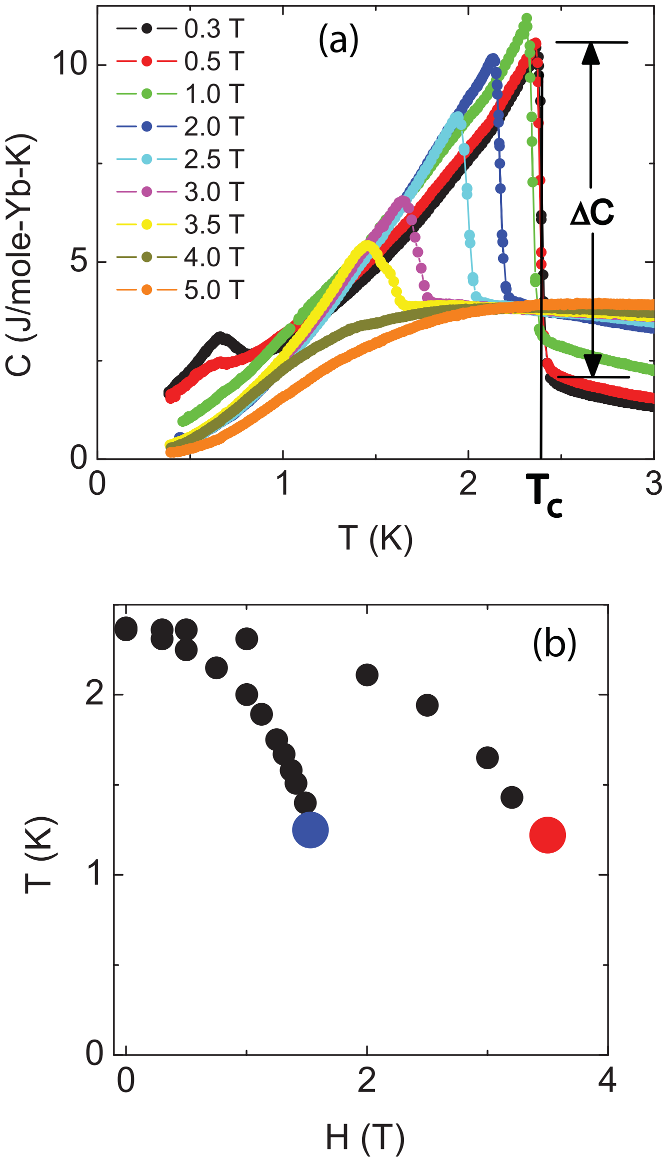

Figure 6.30: (a) The temperature dependence of the specific heat in different magnetic fields with the field applied parallel to the c-axis of the crystal. The small peak at low temperature is due to the presence of a very small amount of a secondary impurity phase, which has been identified as Yb_3Pt_5. The net magnitude of a peak is defined as ΔC and the position of the peak in temperature is defined as T_C. It takes about twice as much magnetic field to suppress the ordering anomaly in the parallel field configuration compared to the perpendicular field configuration. (b)The temperature at which the specific heat peak occurs, T_C, as a function of magnetic field for both the perpendicular and parallel configurations. The peak disappears below 1.3 K, 1.53 T (blue circle) for the perpendicular configuration, and below 1.3 K, 3.5 T (red circle) for the parallel configuration, indicating the presence of a critical endpoint at these positions.

Estimating the Latent Heat

Fig. 6.31 shows a progression of the time dependence of the temperature of a single crystal of $\mathrm{Yb_3Pt_4}$ from zero field to 0.4 T to 1 T for a single crystal of $\mathrm{Yb_3Pt_4}$ near T_C. The non-linear region associated with the latent heat decreases with increasing field, and is nearly gone when the field reaches 1 T. A true second order phase transition, no matter how sharp, would not have a non-linear region, just an immediate transition from one linear region to another with a different slope, with no non-linear region (no latent heat). Fig. 6.32 shows plots of the field dependence of the latent heat. The latent heat is proportional to the reduced field, h=(H-H_{CEP})/H_{CEP} to the power 2.4, where H_C is the value of the magnetic field at the critical endpoint, 1.5 T (Fig. 6.32(b)). A composite plot of the field dependence of the latent heat and the field dependence of ΔC, shows that both quantities decrease with increasing field, but at different non-linear rates, and disappear at the critical endpoint (Fig. 6.33).

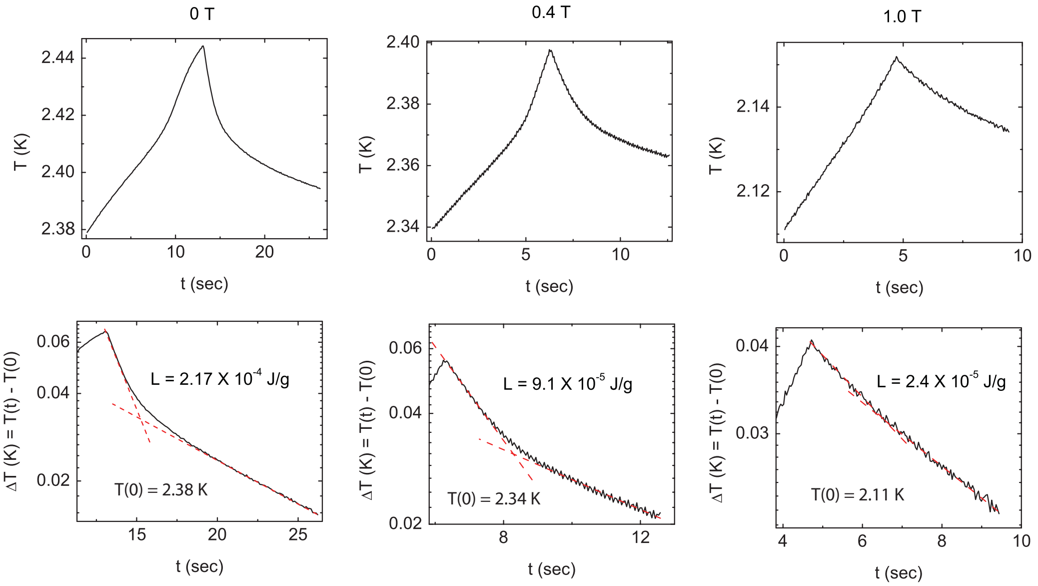

Figure 6.31: A progression of plots of raw T(t) vs. t data for zero, 0.4 T, and 1.0 T fields with heat pulses that rise through the critical temperature. The top row shows the raw data, and the bottom row shows the data re-plotted as logΔT vs. t to illustrate the two linear regions separated by the the field dependent non-linear region associated with a latent heat. At 1 T, the latent heat is nearly gone, and the phase transition resembles a second order phase transition.

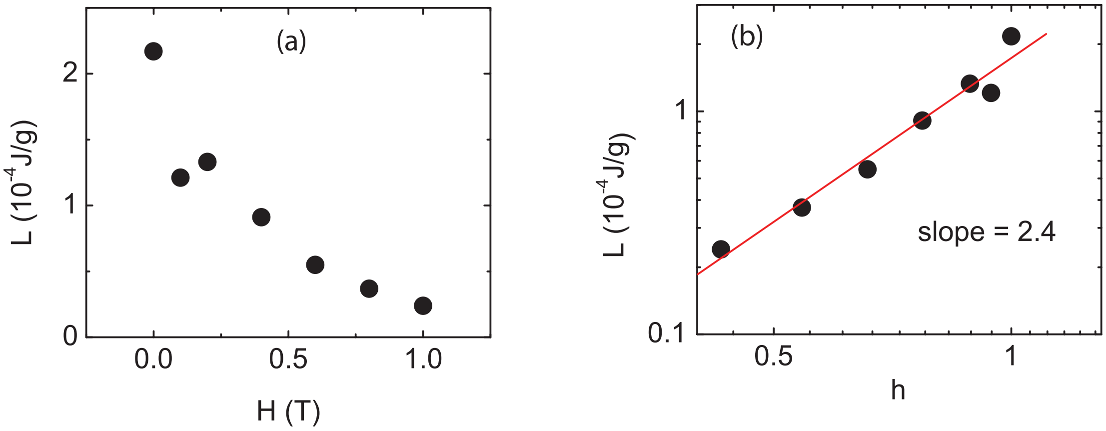

Figure 6.32: (a) A plot of the field dependence of the latent heat. (b) The field dependence of the latent heat plotted on a log-log plot to show its power law behavior. The latent heat, L$\sim$h$^{2.4}$, where the reduced field, h=(H-H$_{CEP}$)/H$_{CEP}$.

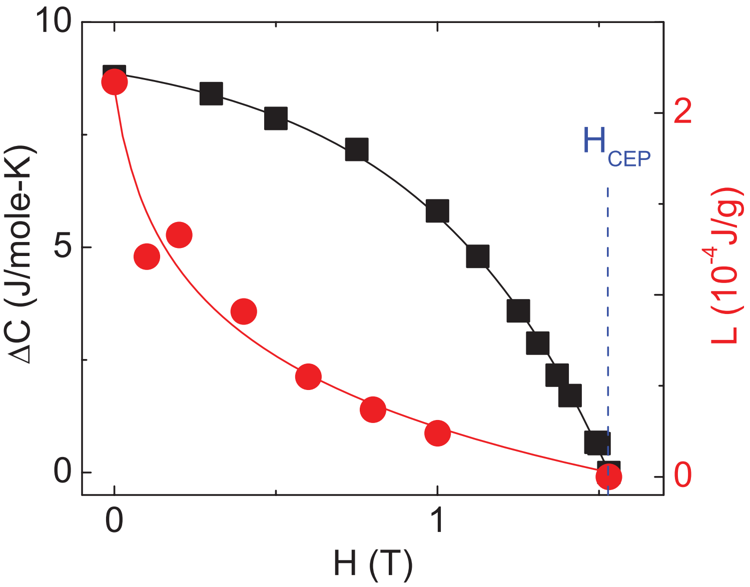

Figure 6.33: A composite plot of the field dependence of the latent heat and ΔC.

6.3.2 The Field Dependence of the Specific Heat at Different Temperatures

To take a more careful look at the nature of the antiferromagnetic phase line at temperatures near and below that of the critical endpoint at 1.2 K, we measured the heat capacity again, but this time holding temperature constant and sweeping the magnetic field. We are especially interested in determining whether the first order phase line extends beyond the critical endpoint to a QCP as the the magnetoresistance data suggests. Fig. 6.34(a) is a plot of the field dependence of the specific heat at different temperatures. Above the 1.2 K critical endpoint, the field dependence of the heat capacity shows a step at the phase line, in agreement with the sharp weakly first order phase transition observed in the C(T) measurements. Below 1.2 K, the step becomes a lambda-like anomaly, as expected for a second order phase transition. The results verify the presence of a first order phase line down to a critical endpoint at (1.5 T, 1.2 K), which becomes a second order phase line below 1.2 K. This information is added to the H-T phase diagram and is in good agreement with the C(T) data (Fig. 6.34(b)). In the next section, we verify the position of the phase line in each field configuration by overplotting the position in field (H_C) of a peak observed in measurements of the magnetoresistance, and find that the phase line continues downward in temperature below the critical endpoint and terminates as a QCP at T=0, and H≈1.6 T.

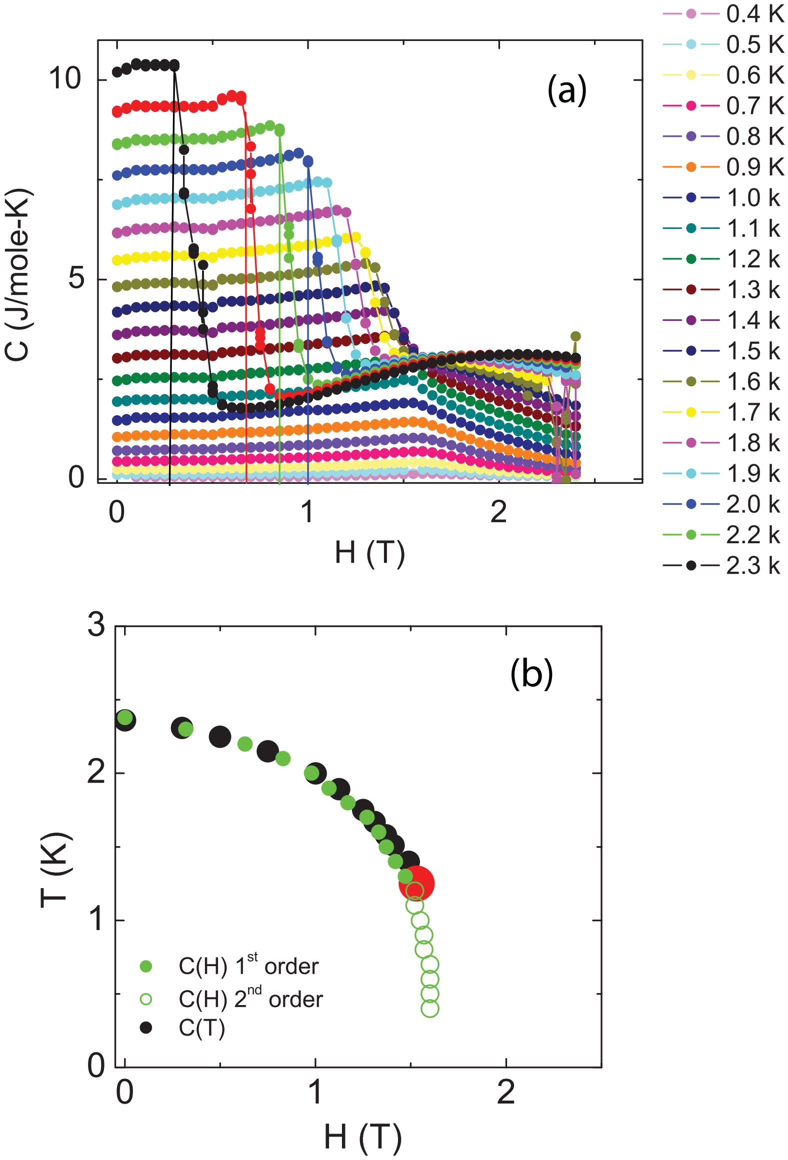

Figure 6.34: (a) The field dependence of the specific heat taken at different temperatures indicated in the key. (b) The position of the phase line determined from the position of the feature observed in the data in (a). The temperatures at which the feature seems first order (solid green circles) and second order (hollow green circles) are added to the H-T phase diagram.

6.3.3 Magnetoresistance

The magnetoresistance was measured at magnetic fields as high as 9 T, and at temperatures ranging from 0.4 K to 30 K with the field both parallel to the a-axis and parallel to the c-axis of the crystal. For higher temperatures within the ordered state, the phase line is marked by a change in slope, which moves up in field as the temperature is decreased (Fig. 6.35) and becomes a peak below ∼1.5 K. This is consistent with the heat capacity data that established a first order phase transition at temperatures higher than the critical endpoint and a second order phase transition for temperatures below the critical endpoint. The magnetoresistance is negative at lower fields, as expected from the decrease in spin disorder scattering with increasing field, but shows a tendency toward a quadratic temperature dependence at higher fields, as expected for a metal. When the positions of the peak in the magnetoresistance are added to the H-T phase diagram, the resulting phase line lies right on top of the line obtained from the heat capacity measurements, and continues the the phase line beyond the critical endpoint. The phase diagram, updated to show

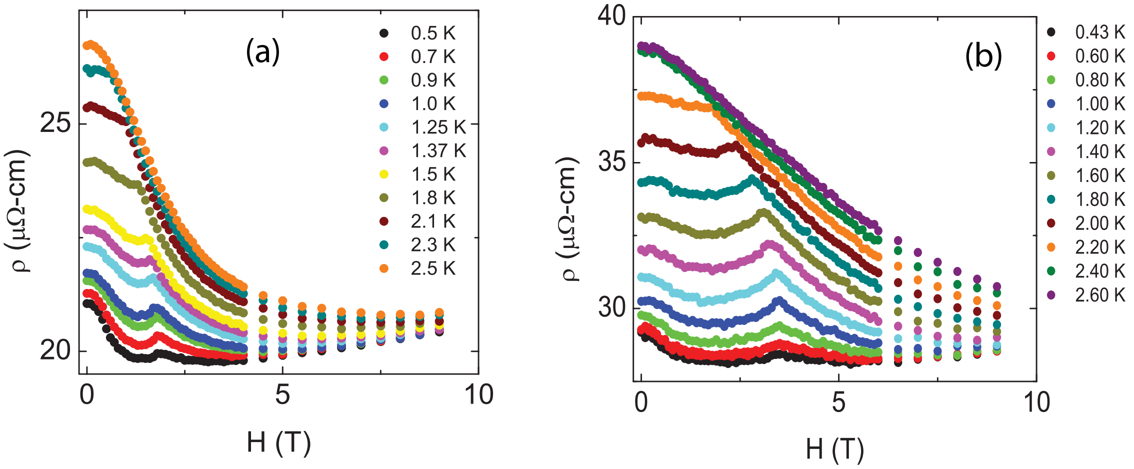

Figure 6.35: (a) The field dependence of the resistivity with the field applied parallel to the a-axis of the crystal. (b) The field dependence of the resistivity with the field applied parallel to the c-axis of the crystal.

the addition of the field dependence of the peak position of the magnetoresistance is shown in figure 6.35. We will show in the following two sections that there is step associated with the phase transition observed in both the temperature and field derivatives of the magnetization.

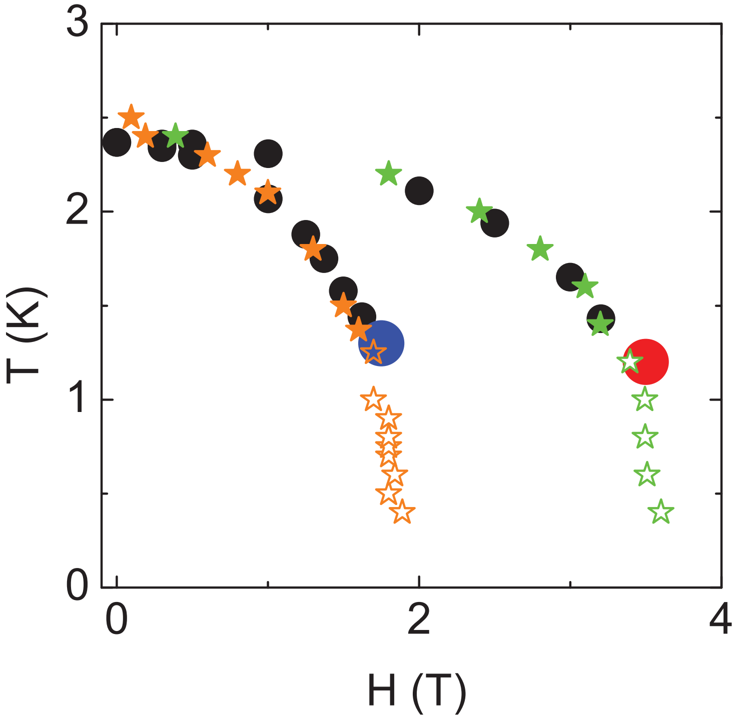

Figure 6.36: An H-T phase diagram for Yb_3Pt_4 from heat capacity and magnetoresistance measurements of a single crystal. The black circles represent the position of the ordering anomaly in the temperature dependence of the heat capacity, with the first order phase line terminating at a critical endpoint for the field applied parallel to the c-axis of the crystal (red) and parallel to the a-axis of the crystal (blue). The orange stars represent the position of the ordering feature in the magnetoresistance when the field is applied parallel to the a-axis, which is a change in slope associated with a first order phase transition at temperatures higher than the position of the critical endpoint (solid stars) and a peak associated with a second order phase transition for temperatures lower than the position of the critical endpoint (hollow stars). The same data for the field applied parallel to the c-axis is represented by the solid and hollow green stars. The phase line mapped out by the magnetoresistance agrees with the specific heat data for the same single crystal of Yb_3Pt_4.

6.3.4 The Temperature Dependence of the AC Magnetic Susceptibility in Different Magnetic Fields

In this section we present our measurements of the field derivative of the magnetization, which is determined from the AC magnetic susceptibility (χ_{AC}=χ'+iχ”), where χ'(H)=∂M/∂H. In Fig. 6.37, we have plotted the temperature dependence of the in-phase AC magnetic susceptibility, χ' at different fixed fields above and below the value of the field at the critical endpoint, H_{CEP}. In zero field the magnetic susceptibility has a cusp at T_N=2.4 K, but when a magnetic field is applied, a sharp step-like anomaly in the magnetic susceptibility develops at T_N, which increases in magnitude with increasing magnetic field (Fig. 6.37(b)). We have added the position of the step-like anomaly to our H-T phase diagram and it lies right on top of the phase line determined from the specific heat and magnetoresistance data (Fig. 6.38, blue triangles). The phase line based on the magnetoresistance data (Fig. 6.32, magenta stars) does not line up with the heat capacity data (Fig. 6.38, green circles). We have verified that T_N(H) is the same for crystals taken from different batches, but since we only control sample orientation to ~5°, the difference between the two data sets most likely reflects this uncertainty. The crystal used for the magnetoresistance measurements seems to have been misaligned by ~5° from the a-axis of the crystal, resulting in the phase line falling to zero temperature at a slightly higher field, consistent with the known anisotropy properties described earlier. There is also a broad maximum at higher temperatures that moves upward in temperature with increasing magnetic field (Fig. 6.37(a)). We will take a closer look at this broad maximum in sec. 5.4 and show that it could be associated with the Zeeman splitting of the ground state doublet.

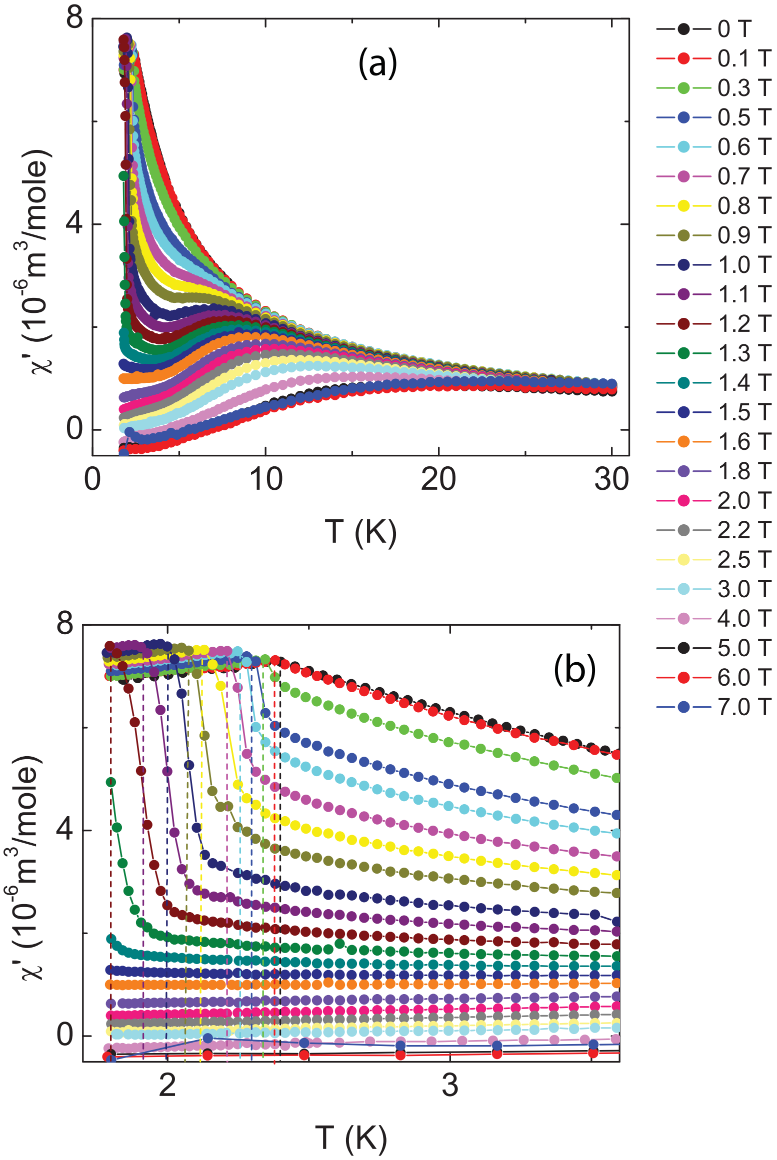

Figure 6.37: (a) The temperature dependence of the AC magnetic susceptibility in different fields in temperatures up to 30 K for a single crystal of Yb_3Pt_4 with the magnetic field applied perpendicular to the c-axis of the crystal. (b) The same data as in (a), but zooming in on the low temperature region to show the sharp feature associated with the transition to the antiferromagnetic state. The vertical dashed lines show the position in temperature of the antiferromagnetic transition, T_N.

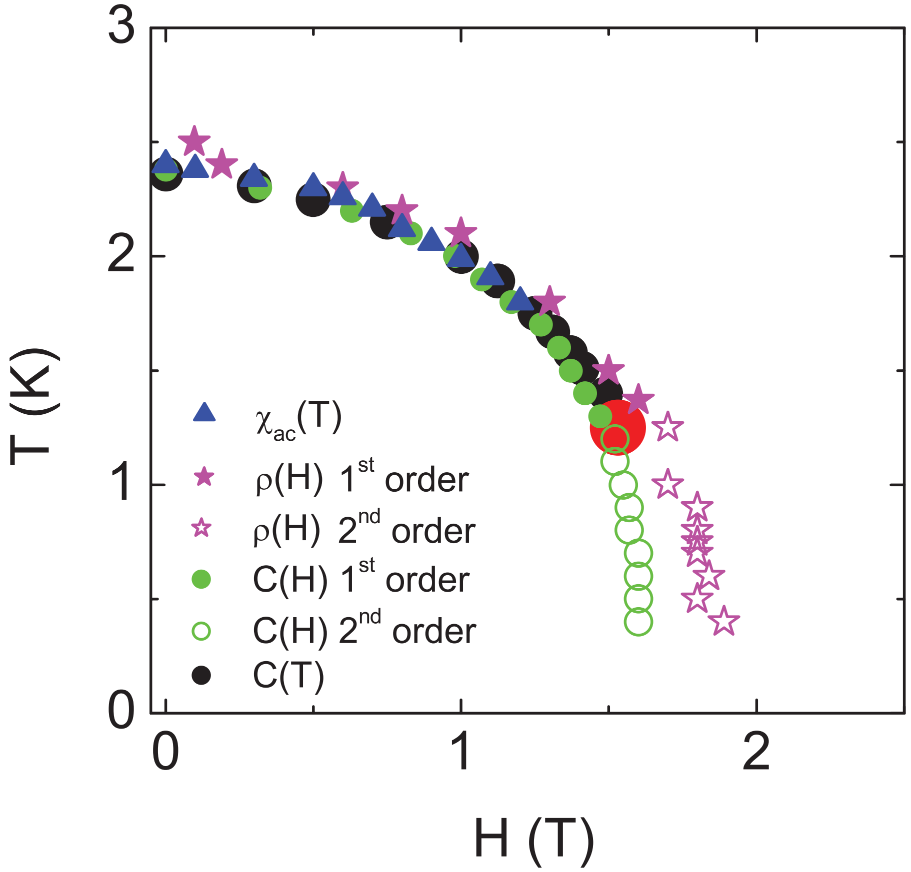

Figure 6.38: The H-T phase diagram with the temperature and field position of the sharp drop in the AC magnetic susceptibility added (blue triangles). The magnetoresistance data (magenta stars) deviate from the actual phase line, because they were taken using a different single crystal that was misaligned ∼5° from the field magnetic field direction parallel to the a-axis of the crystal.

6.3.5 The Temperature Dependence of the Magnetization in Different Magnetic Fields

In this section, we show that there is also a step in the temperature derivative of the magnetization, dM/dT and it corroborates the position of the antiferromagnetic phase line. Fig. 6.33(a) is a plot of the temperature dependence of the magnetization measured in different fixed magnetic fields. We find a weak slope change at T_N, which occurs at decreasing temperature with increasing magnetic field. The temperature derivative, dM/dT, shows a step-like anomaly at T_N (Fig. 6.39(b)). We have added the position of the step like anomaly in dM/dT to our H-T phase diagram and it too agrees with all the previous measurements (Fig. 6.40, yellow squares). We now have a well established H-T phase diagram for Yb_3Pt_4 based on a number of different measurements.

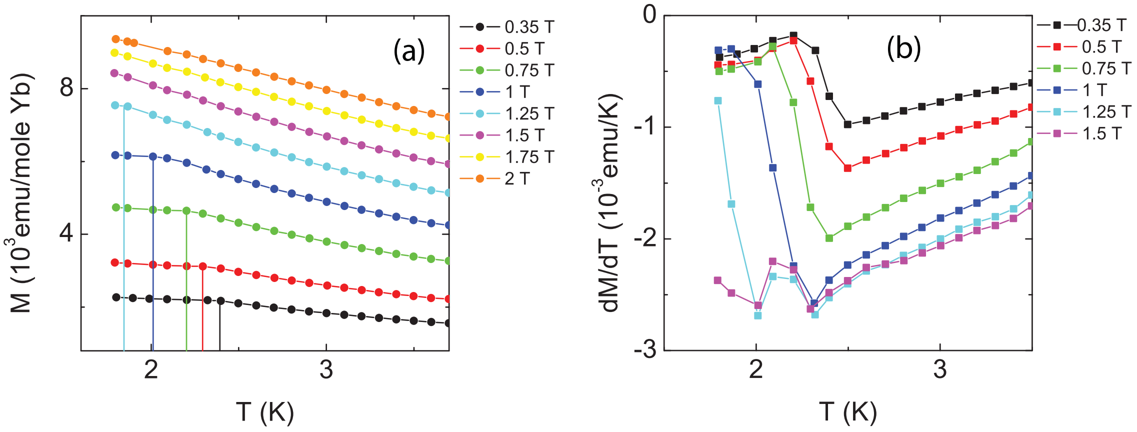

Figure 6.39: (a) The temperature dependence of the magnetization taken in different magnetic fields indicated in the key (b) The derivative, dM/dT of the data in (a).

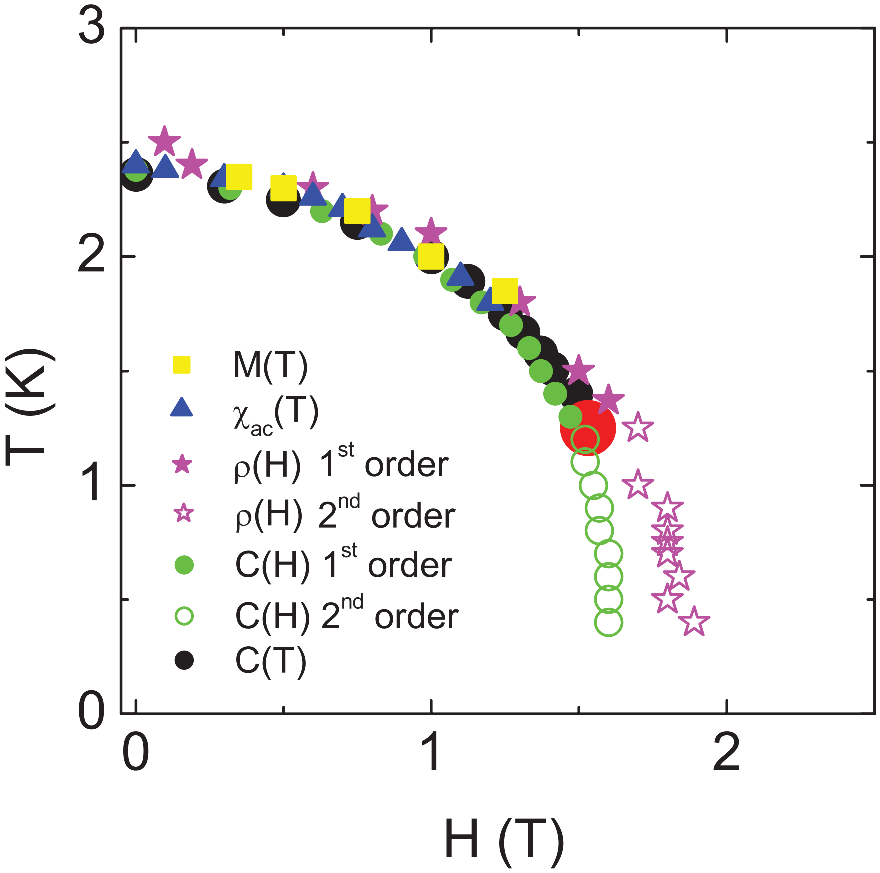

Figure 6.40: The H-T phase diagram with the position of the weak peak in the magnetization added (yellow squares). Recall that the magnetoresistance data (magenta stars) deviate from the actual phase line, because of the ∼5° misalignment with respect to the field direction parallel to the a-axis of the crystal.

6.3.6 Mapping the Fermi Liquid Region

Since the region of quadratic temperature dependence of the resistivity defines the Fermi liquid (FL) region, this region can be added to the phase diagram by measuring the temperature dependence of the resistivity in different applied magnetic fields and marking on our H-T phase diagram the position in field and temperature where the resistivity first deviates from a quadratic temperature dependence. Fig. 6.41 shows plots of the temperature dependence of the resistivity in different magnetic fields with the field applied perpendicular to the c-axis of the crystal (a) and parallel to the c-axis of the crystal (b). The sharp drop in ρ at T_N due to spin disorder scattering in zero field is gradually suppressed with increasing magnetic field (Fig. 6.41(a)), showing that the application of a magnetic field gradually decreases the spin disorder scattering. Evidence for spin disorder scattering is found in the relation between the magnetoresistance and the magnetization shows the expected behavior of the fluctuating paramagnetic spins gradually forced to align with the increasing

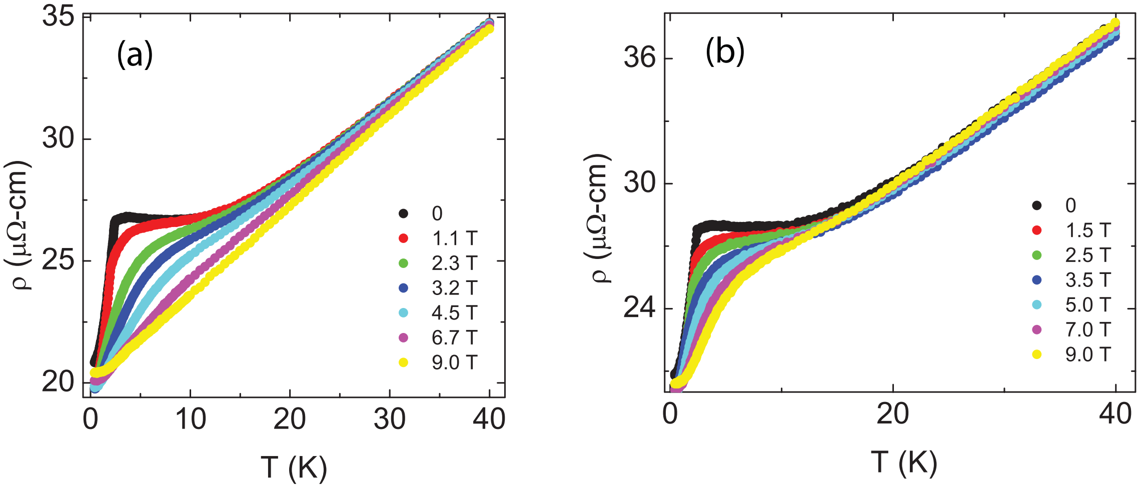

Figure 6.41: (a) The temperature dependence of the resistivity in fields up to 9 T, applied perpendicular to the c-axis. (b) The temperature dependence of the resistivity in fields up to 9 T, applied parallel to the c-axis.

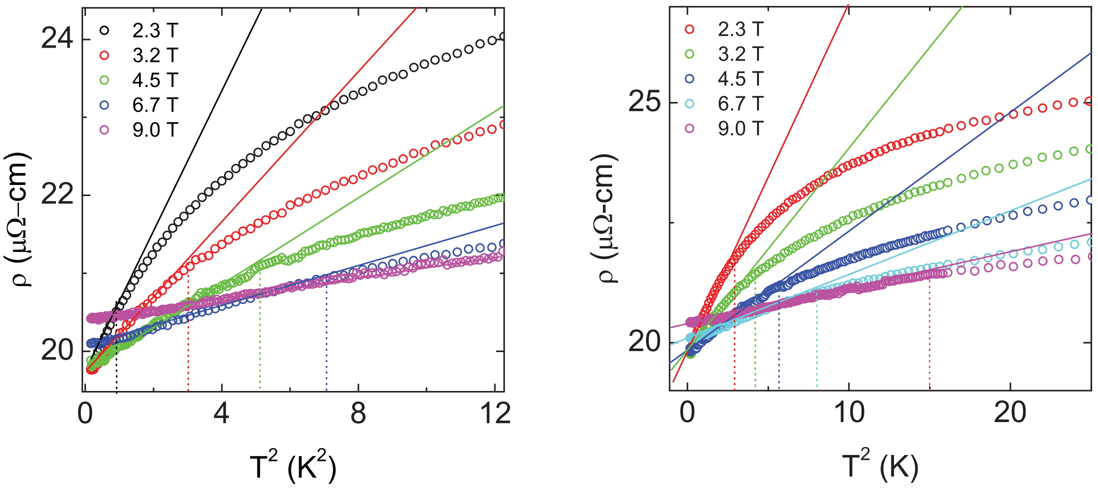

Figure 6.42: (a) The resistivity plotted as a function of temperature squared in fields up to 9 T applied perpendicular to the c-axis. The vertical dotted lines indicate the position where the resistivity deviates from a quadratic temperature dependence(b) The same plot as in (a), but with the field applied parallel to the c-axis.

magnetic field, resulting in a drop in resistivity according to

$$\frac{\Delta\rho}{\rho} \propto \left(\frac{M}{M_s}\right)^2,$$

where $\Delta\rho/\rho$ is the magnetoresistance, M is the magnetization, and M$_S$ is the saturation magnetization. The data deviate from this behavior after entering the magnetically ordered phase (Fig. 6.44(a), black circles and red circles). With the field applied perpendicular to the c-axis of the crystal, the application of a 9 T field completely suppresses the spin disorder scattering, rendering the resistivity linear with temperature from 3 K all the way up to 40 K. With the field applied parallel to the c-axis of the crystal, a similar trend is seen, but because of the weak anisotropy, 9 T is not quite enough to completely suppress the spin disorder scattering in this orientation. In Fig. 6.42, we have re-plotted the data from Fig. 6.41 as function of T^2 to show more clearly where the temperature dependence deviates from quadratic behavior. These temperatures and fields have been plotted on our H-T phase diagram (Fig. 6.43), defining an effective Fermi temperature for the quasiparticles, T$_{FL}$, below which FL behavior is found.

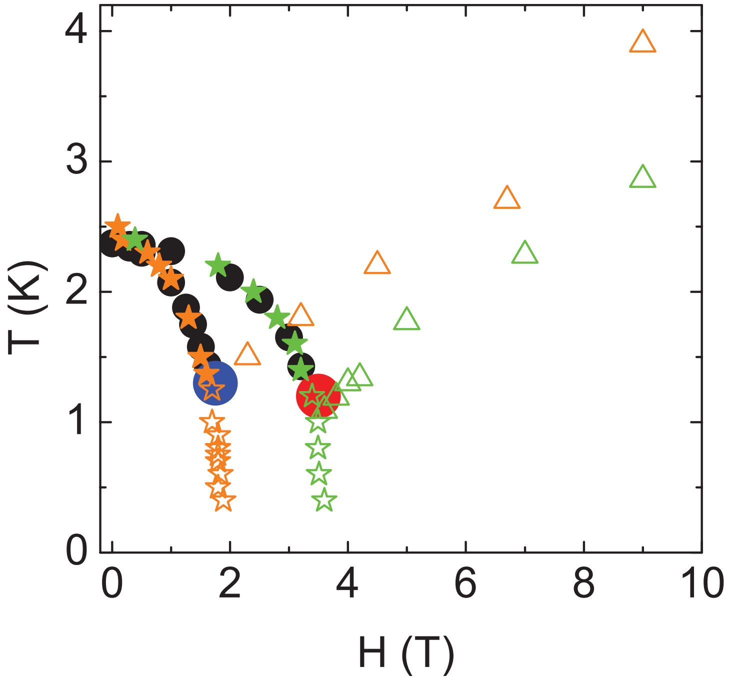

Figure 6.43: The H-T phase diagram with the Fermi liquid phase lines obtained from the quadratic temperature dependence of the resistivity in field. The orange triangles represent the FL line with the field applied parallel to the a-axis and the green triangles represent the FL line when the field is applied parallel to the c-axis.

For Yb_3Pt_4, the Fermi liquid crossover line appears to end not at H=H_{QCP}=1.6 T, but closer to H=H_{CEP}=1.5 T, near the critical endpoint. This is an important observation, showing the anomalous quantum critical behavior of Yb_3Pt_4. To make absolutely sure that the Fermi liquid crossover line does not extend sharply down to the QCP, we measured the temperature dependence of the resistivity in a high density of fields around H_{CEP} (Fig. 6.45(a)). To map out the crossover line, we used the same technique as we used earlier, by plotting ρ-ρ_0 versus T^2 (Fig. 6.45(b)), and marking the position in temperature where the resistivity deviates from a quadratic temperature dependence. The high density data verify that the high field Fermi liquid crossover line terminates at the critical endpoint, forming a minimum at H_{CEP} (Fig. 6.46, orange triangles). The FL data were taken with the same experimental set-up and crystal, so have the same alignment as the magnetoresistance data (magenta

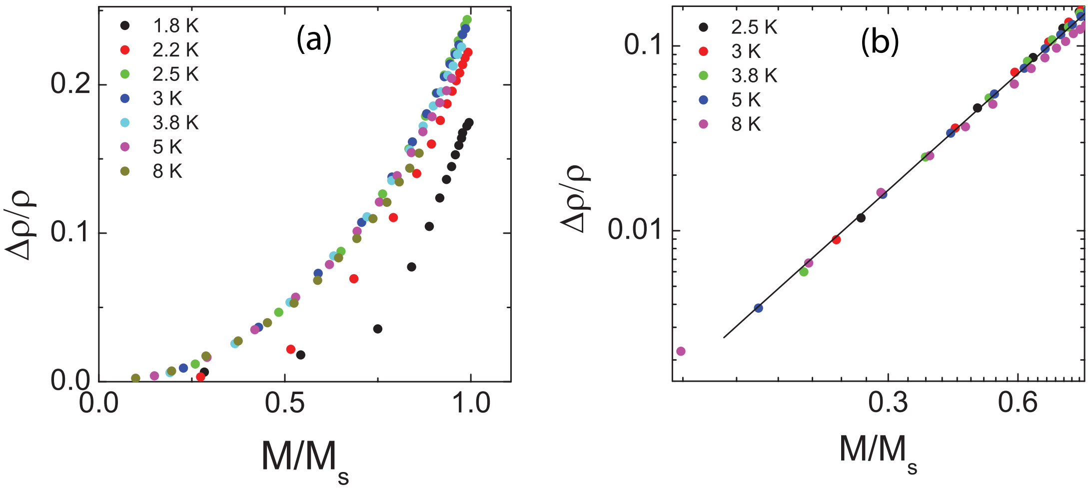

Figure 6.44: (a) A plot of the normalized resistivity as a function of the normalized magnetization showing that the data collapse onto a single quadratic curve for data outside the ordered phase (b) The data from outside the ordered phase only plotted on a log-log plot showing that they collapse onto a single line that has a slope of 2, showing the expected quadratic dependence of the normalized resistivity on the normalized magnetization.

stars). This leads to the FL crossover line also deviating somewhat from the actual crossover line.

It is remarkable that $T_{FL} \approx T_N$, suggesting that the transition to an antiferromagnetic state somehow enables the formation of a Fermi liquid. In the FL region ($T<T_{FL}$) we can no longer consider individual electrons and instead consider quasiparticles with an enhanced mass, m*. In well studied quantum critical materials such as $YbRh_2Si_2$ and $CeCu_{5.8}Au_{0.2}$, T_{FL}=0 at the QCP, suggesting that both the Fermi liquid state and thus the quasiparticles and thus m* disappear. It is thus unusual and unexpected that $T_{FL} \neq 0$ anywhere for Yb_3Pt_4, despite the presence of the QCP at 1.6 T.

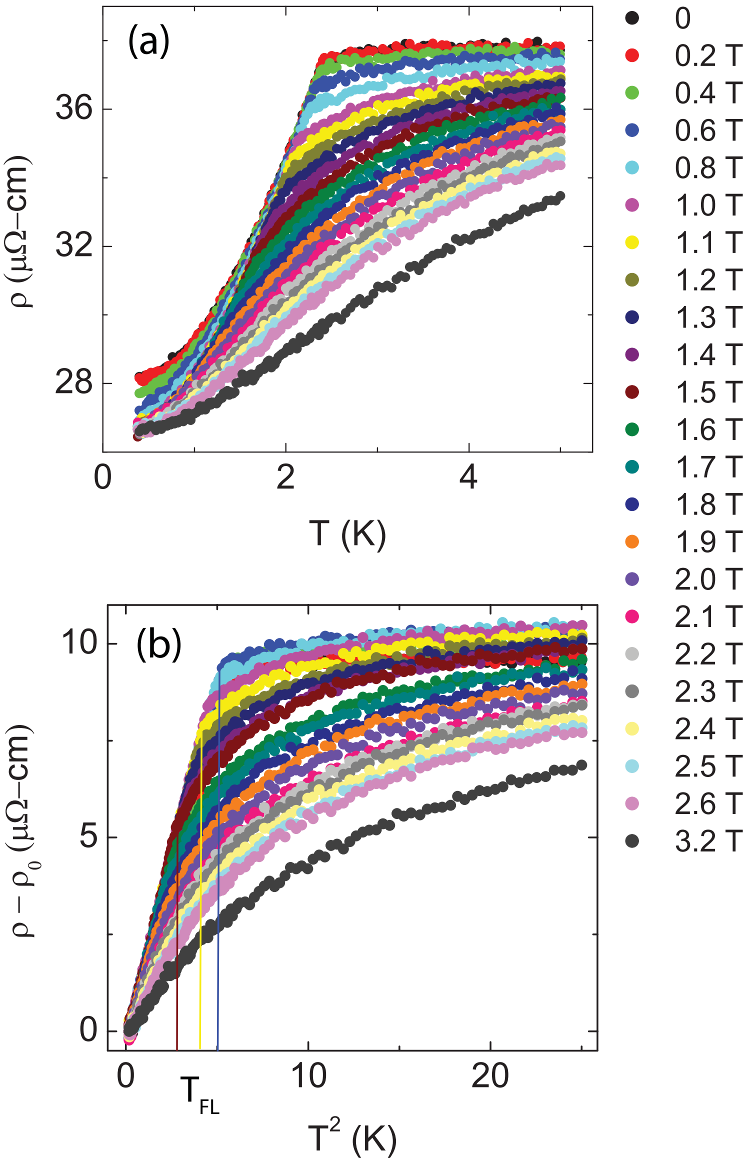

Figure 6.45: (a) The temperature dependence of the resistivity measured over a high density of fields from zero to 3.2 T, with the magnetic field applied perpendicular to the c-axis of the crystal. (b) The same data as (a) plotted as a function of T^2. The vertical lines mark where the resistivity begins to deviate from a quadratic temperature dependence at different fields. (c) A close up of the region of the H-T phase diagram showing that the Fermi liquid line definitely does not drop sharply to zero at the QCP, but has a minimum at the critical endpoint.

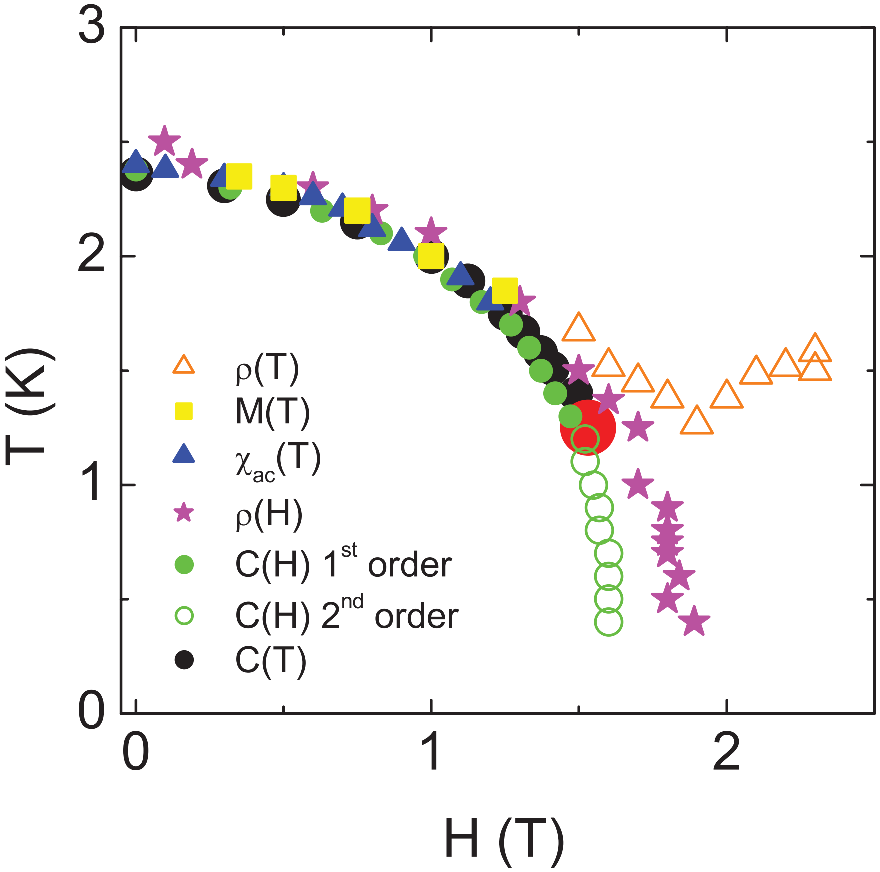

Figure 6.46: A close up of the region of the H-T phase diagram showing that the Fermi liquid line (orange triangles) definitely does not drop sharply to zero, but terminates near the critical endpoint. The data points based on the magnetoresistance data (magenta stars) and the ρ(T) in field data deviate slightly from the actual phase line, because the single crystal used for these measurements was misaligned with respect to the intended magnetic field orientation parallel to the a-axis of the crystal.

6.3.7 The Complete Phase Diagram for Yb_3Pt_4

We have created an H-T phase diagram for Yb_3Pt_4 at fields up to 9 T, applied parallel to the a-axis of the crystal, with the phase lines well established and corroborated by multiple measurement techniques (Fig. 6.46). There is local moment paramagnetism over the entire region of the phase diagram from room temperature right down to the magnetic and Fermi liquid phase lines (blue region). We find a critical endpoint at (1.5 T, 1.2 K) (blue circle) and a QCP near 1.6 T (red circle). The ordered state (yellow region) is a Fermi liquid and there is a second paramagnetic Fermi liquid state (magenta region) in the high field region outside the ordered state. In the next section we will further analyze the data that we used to construct the phase diagram and uncover some of the mechanisms leading to this unique phase diagram.

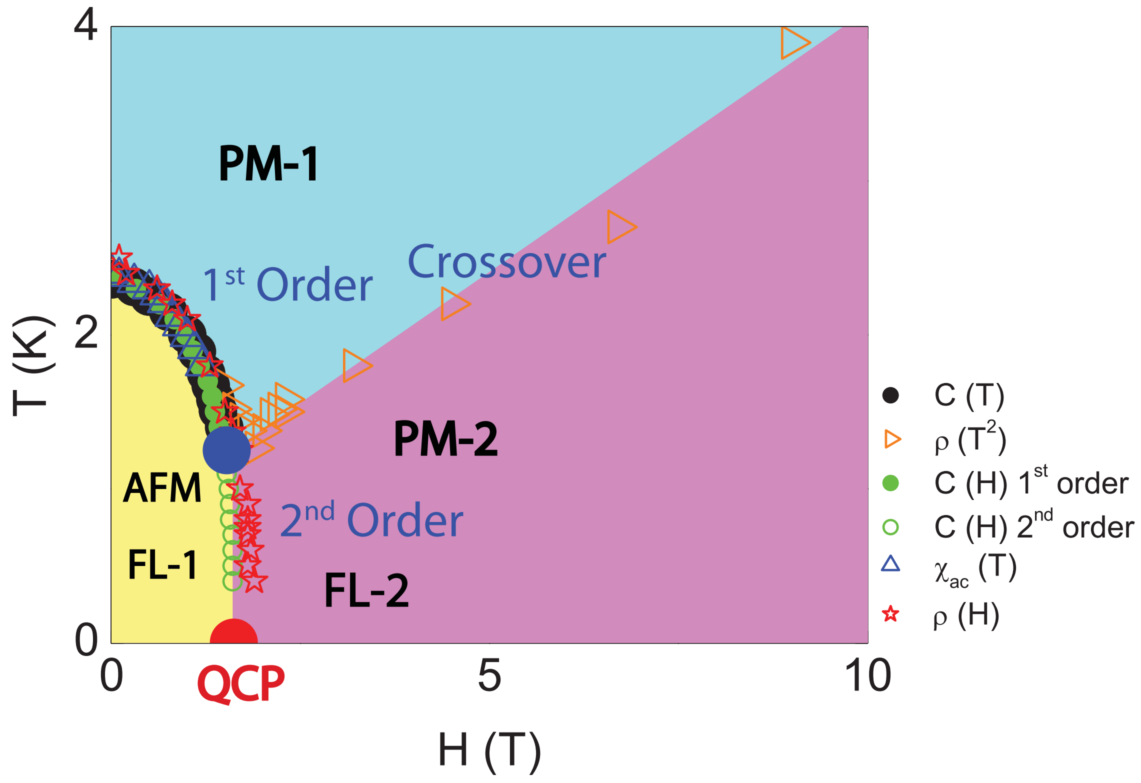

Figure 6.47: The H-T phase diagram for Yb_3Pt_4 based on the data indicated in the key.

6.4 Properties of the Magnetic Field Tuned Phases in Yb_3Pt_4

In this section, we continue our analysis of the magnetic field dependent data that were used to build the phase diagram and present some key properties of the Yb_3Pt_4 H-T phase diagram revealed by our analysis. We finish this section by comparing the properties of the Yb_3Pt_4 phase diagram with the properties of the expected phase diagram for typical heavy fermion materials such as $YbRh_2Si_2$ and $CeCu_{6-x}Au_x$. We begin in the next section by demonstrating the prevalence of H/T scaling and magnetic field suppression of spin disorder scattering, both of which are expected in a local moment paramagnetic phase (Fig. 6.47, blue region). In subsequent sections, we will describe the zero field magnetic structure of Yb_3Pt_4 determined from powder neutron diffraction measurements, followed by an analysis of the heat capacity data that shows the presence of Zeeman splitting of the doublet ground state, affecting the value of the heat capacity from the ordered state through the high field FL region. Finally, we will show the field dependence of the FL parameters, γ, χ_0 and A and compare their behavior, and the entire Yb_3Pt_4 phase diagram to their analogs expected for a typical heavy fermion quantum critical compound such as $YbRh_2Si_2$.

6.4.1 H/T Scaling in the Local Moment Paramagnetic Phase

We know from the basic properties described in previous sections that in the high temperature paramagnetic phase we find nearly the full Yb^{3+} moment of 4.24 μ_B/Yb from measurements of the DC magnetic susceptibility and Brillouin-like behavior in the field dependence of the magnetization, indicating local moment character right down to the antiferromagnetic phase line, with no sign of the approaching magnetic order (Fig. 6.48). We find additional evidence that the local moment paramagnetism is dominant in the field dependence of the heat capacity measured at different temperatures and the temperature dependence of the magnetization measured in different magnetic fields, which both clearly show H/T scaling right up to the antiferromagnetic phase line and no evidence for NFL behavior anywhere in the H-T phase diagram for Yb_3Pt_4. Fig. 6.48(a) shows that measurements of the heat capacity at different fields and temperatures taken outside the magnetically ordered phase fall onto a universal curve when plotted as a function of H/T, with a broad maximum near H/T=1 T/K. The data that do not fall on the universal curve represent the magnetically ordered phase, with the sharp step at the higher temperatures associated with the first order phase transition betweent the two phases. Fig. 6.48(b) shows that measurements of the magnetization at different fields and tempetatures also fall onto a universal curve when plotted as a function of T/H, with the data from the ordered phase deviating from the universal curve at sufficiently low values of T/H.

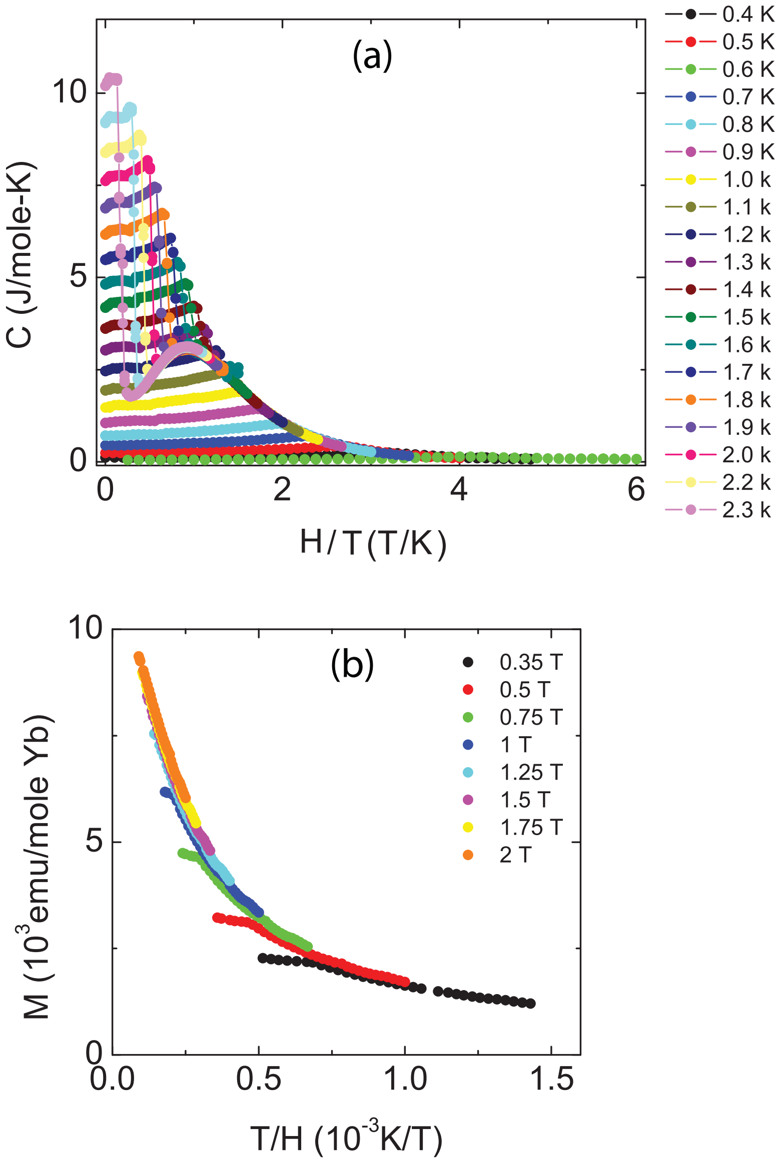

Figure 6.48: (a) A plot of the specific heat as a function of H/T, showing how the data collapse on to a single curve for all points outside of the ordered phase. (b) A plot of the magnetization as a function of T/H showing that the data again collapse onto a single curve for data outside of the ordered phase.

6.4.2 Zeeman Splitting of the Doublet Ground State

Our specific heat measurements show that the doublet ground state is split by the applied magnetic field. The broad feature in the temperature dependence of the specific heat fits well to the expression for a Schottky anomaly, and the energy of the splitting increases with increasing field (Fig. 6.49). As expected, the broad feature moves up in temperature with increasing magnetic field reflecting the increased energy spacing between the ground and excited states. The Schottky fits (Fig. 6.49(a), black lines) work very well at temperatures above the antiferromagnetic phase transition, but within the ordered phase, it is very difficult to estimate what contribution the Schottky anomaly is, because there are likely multiple mechanisms contributing to the heat capacity in the ordered phase. However, the energy splitting seems to become constant in the ordered phase ∼4 K. In the next section, we will show how the FL parameters evolve with changing magnetic field, especially near the QCP.

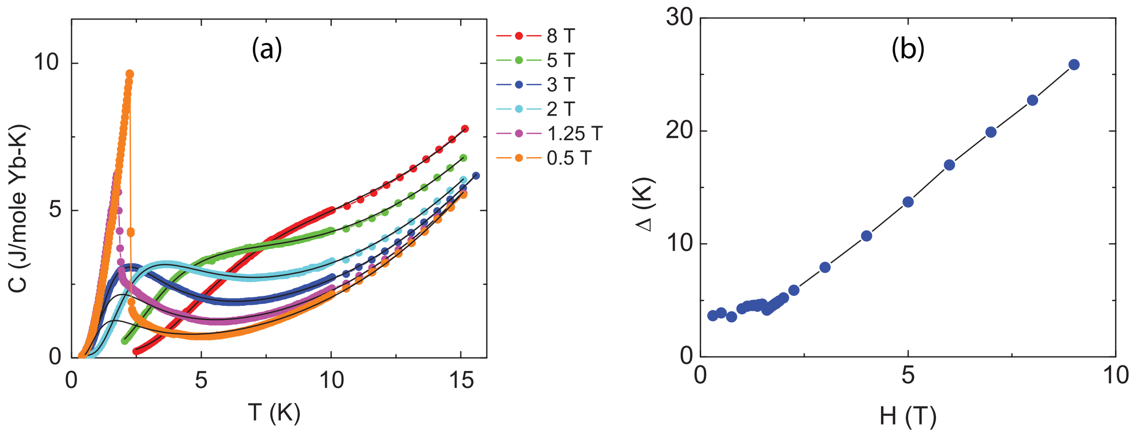

Figure 6.49: (a)The temperature dependence of the heat capacity in different magnetic fields indicated in the key with fits to a Schottky anomaly (black lines). The fits become less accurate at the lower fields within the ordered state, because of the large ordering anomaly. (b) The field dependence of the energy between the first and second level of the split doublet ground state.

6.4.3 The Field Dependence of the Fermi Liquid Parameters

In this section, we present the field dependence of the FL parameters, γ, A, and χ_0 for Yb_3Pt_4, especially near the QCP. Previously, we discussed how the effective mass, and therefore A and γ diverge as the QCP is approached from the high field FL phase in typical quantum critical heavy fermion compounds like $YbRh_2Si_2$ and $CeCu_{6-x}Au_{0.2}$. The field dependences of the FL parameters exhibit very different behavior in Yb_3Pt_4. While moderately high values of γ are found in the high field FL phase (Fig. 6.50(a)), γ is extremely small in the ordered FL phase despite the very high values of χ_0 and A, making it difficult to classify the ordered phase of Yb_3Pt_4. The major difference compared with previously studied quantum critical systems is that instead of diverging near the QCP, γ is essentially field independent in the high field FL phase, with a weak maximum near 5 T. The values of γ are moderate compared with heavy fermion materials with γ ranging from ~60 mJ/mole-K^2 to ~160 mJ/mole-K^2 at the peak near 5 T. The coefficient of the quadratic part of the resistivity increases by a factor of ~30 in the high field FL phase from 9 T to H_{CEP}, then remains nearly field independent through the antiferromagnetic phase (Fig. 6.50(b)). In the ordered phase, χ_0 and A are large and almost field independent (Fig. 6.50(b)). The Sommerfeld-Wilson ratio (R_W) appears to diverge on approach to H_{CEP} from the high field FL phase (Fig. 6.51(a)), but a more careful analysis reveals that it actually diverges at H=0, with $R_W \sim H^{-3}$ (Fig. 6.51(b)), but is cut off near H_{CEP} by the phase transition to the antiferromagnetic state. We find a similar result for the field dependence of the Kadowaki-Woods ratio, which initially also seems to diverge at H_{CEP} (Fig. 6.51(c)), but on closer analysis, also is found to diverge at H=0, with $A/\gamma^2 \sim H^{-3}$ (Fig. 6.51(d)), but is cut off near H_{CEP}. There is no divergence of the quasiparticle effective mass observed in Yb_3Pt_4 at the QCP, rather

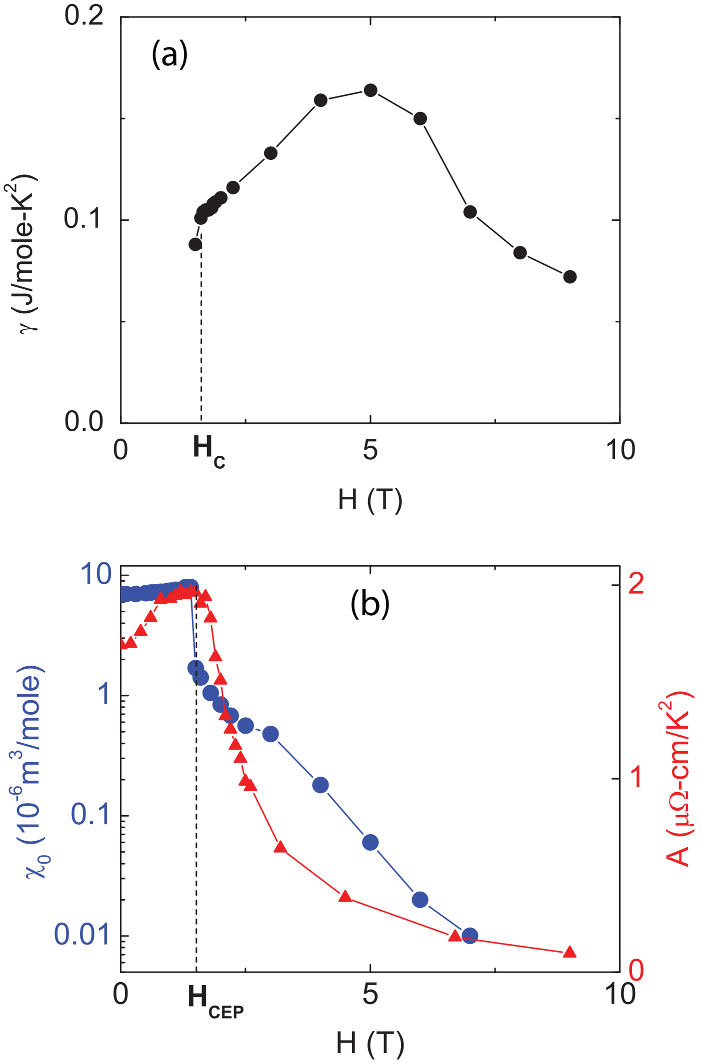

Figure 6.50: (a)The field dependence of γ, showing a weak maximum near 5 T. (b) The field dependence of χ_0 and A.

the magnetic order is driven by the diverging quasiparticle interactions, evidenced by the diverging R_W.

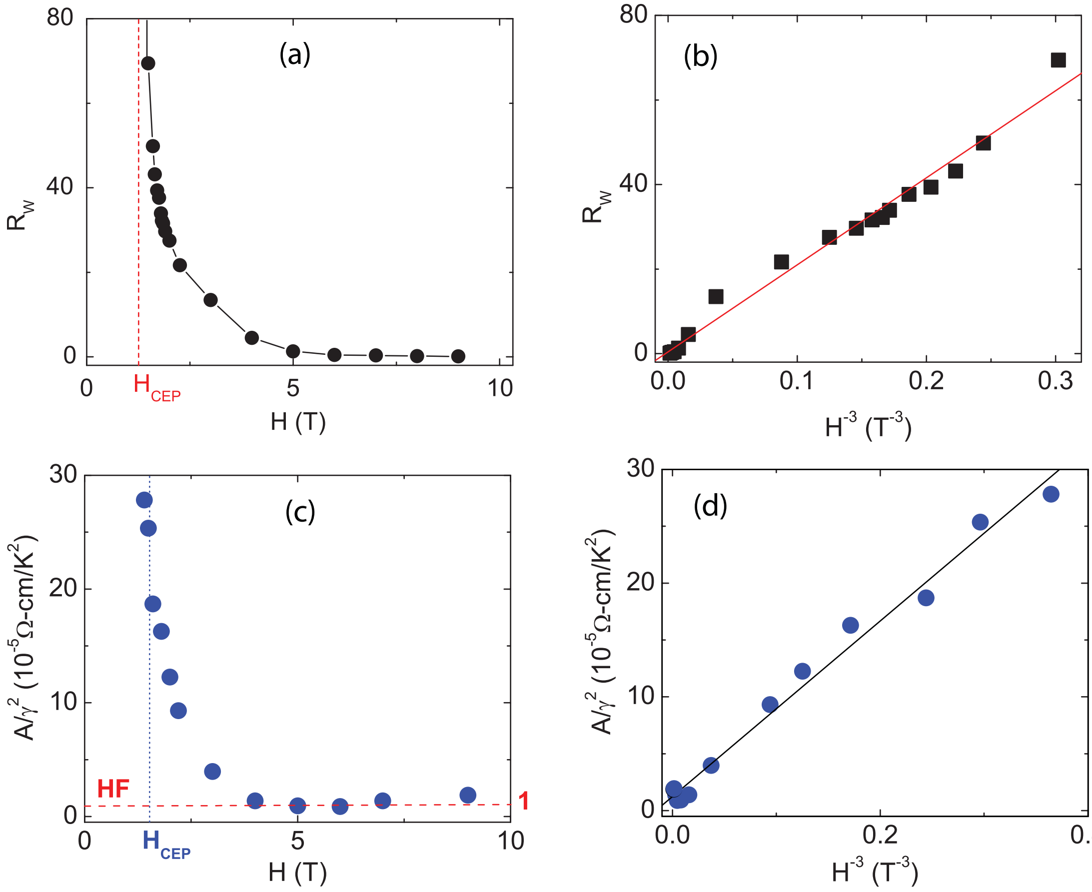

Figure 6.51: (a) The field dependence of R_W seems to diverge on approach to H_{CEP} (red dashed line) from the high field FL phase. (b) A closer analysis reveals that R_W actually diverges at H=0, with $R_W \sim H^{-3}$. (c) The field dependence of the Kadowaki-Woods ratio, A/γ^2, showing that Yb_3Pt_4 has the expected heavy fermion value of $1\times10^{-5}\Omega cm/K^2$ (red dashed line), but like R_W, seems to diverge at H_{CEP} (blue dotted line). (d) A closer analysis reveals that the Kadowaki-Woods ratio, like R_W, actually diverges at H=0, with $A/\gamma^2 \sim H^{-3}$.

6.4.4 Phase Diagram Comparison

We now take a look at the overall phase diagram and see how it compares with some of the general properties of other experimentally determined quantum critical systems and current theoretical models. In Fig. 6.52, we have plotted the phase diagram for Yb_3Pt_4 next to the generic type of phase diagram displayed by typical previously measured quantum critical systems such as $YbRh_2Si_2$ and $CeCu_{6-x}Au_x$. There are several major differences. The phase diagram for Yb_3Pt_4 is unique. It is the only known example of a quantum critical system with a first order antiferromagnetic transition that can be tuned first to a critical endpoint, and then to a QCP near 1.6 T, with the phase transition second order from the critical endpoint to T=0, a required feature of a QCP. For $YbRh_2Si_2$ and $CeCu_{6-x}Au_x$, there is no critical endpoint and the entire phase line is second order. Another significant difference is that the FL crossover line does not extend to the QCP for Yb_3Pt_4, but instead T_{FL} has a minimum near the critical endpoint. The field dependences of the FL parameters also show unusual behavior. γ (~m*) for Yb_3Pt_4 is only very weakly field dependent near the QCP, but both A (~m^{*2}) and χ_0 (~m*) diverge at H=0, but are suddenly cut off by the weakly first order antiferromagnetic phase transition at H>0.

One of the unique characteristics of Yb_3Pt_4 is that γ, and therefore m* do not diverge on approach to the transition to the ordered state. We do, however, observe that both the Kadowaki-Woods ratio, A/γ^2, and R_W ($\propto \chi/\gamma$) do diverge on approach to H=0 from the high field FL state. We conclude that these divergences are due not to a diverging m*, which is normally the case for quantum critical heavy fermions, but due to the magnetic interactions among the quasiparticles. Since $A \propto m^{*2}$, $\gamma \propto m^*$, and $\chi_0 \propto m^*/1+F_0^a$, both R_W, and the Kadowaki-Woods ratio are m* independent and thus the divergence in these quantities must be due to the $1/1+F_0^a$ term, which is the term representing the magnetic interactions among the quasiparticles in a Fermi liquid.

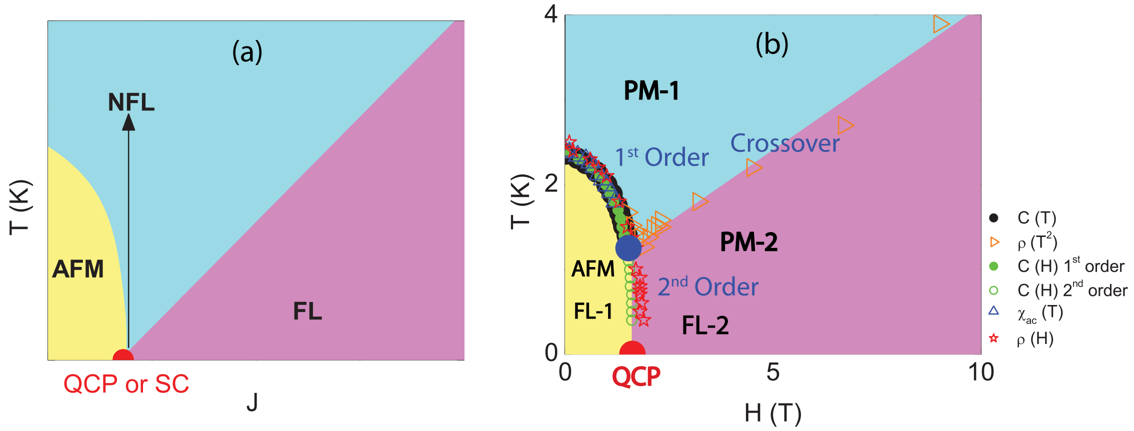

Figure 6.52: (a) The generic phase diagram expected for quantum critical heavy fermion materials (b) The H-T phase diagram for Yb_3Pt_4.

6.4.5 Summary and Conclusions

Summary

- We determined the magnetic field-temperature phase diagram for Yb_3Pt_4 from measurements of the heat capacity, electrical resistivity, magnetization and AC magnetic susceptibility. In zero field, Yb_3Pt_4 undergoes a weakly first order phase transition to an antiferromagnetic state at T_N=2.4 K. The application of a magnetic field parallel to the a-axis of the crystal decreases T_N, with the first order phase line terminating at a critical endpoint at 1.2 K and 1.5 T. Further increasing the magnetic field continues to decrease T_N, forming a second order phase line that is driven to a QCP at 1.6 T. Local moment paramagnetism dominates at higher temperatures, with both the heat capacity and the magnetization showing H/T scaling outside the ordered phase.

- We find two FL states in the H-T phase diagram for Yb_3Pt_4. The transition to the antiferromagnetic state at T_N=2.4 K coincides with the formation of a Fermi liquid, with T_{FL} for the ordered state terminating at the CEP. A FL phase is also found on the high field side of the CEP, with T_{FL} extending upward in field and temperature from the CEP. T_{FL} never reaches T=0, having a minimum at T_{CEP}. We find no evidence for NFL behavior near the QCP, or anywhere else within the phase diagram.

- The zero field Fermi liquid parameters for Yb_3Pt_4, A=1.7 $\mu\Omega$-cm/K^2 and χ_0 = 6.8×10^{-6}m^3/mole Yb are among the highest found for heavy fermion compounds, suggesting substantial mass enhancement of the quasiparticles, but surprisingly, γ is extremely small in the ordered phase, contradicting this result and suggesting little or no mass enhancement. In the high field FL phase, γ ∼100 mJ/mole-K, suggesting moderate mass enhancement in agreement with the moderately high values of χ_0 and A. A and χ_0 diverge on approach to the antiferromagnetic phase from the high field FL phase, with A increasing by a factor of ∼30 from 9 T to H_{CEP}. χ_0 shows a much stronger divergence on approach to the CEP, increasing nearly three orders of magnitude from ∼10^{-8} m^3/mole at 7 T to ∼10^{-5} m^3/mole at H_{CEP}. γ remains largely field independent on approach to H_{CEP}, showing a weak maximum near 5 T, with values ranging from 60 to 160 mJ/mole-K^2.

Conclusions

- The phase diagram for Yb_3Pt_4 is unique among quantum critical materials. It is the only known example of an antiferromagnet with a first order phase transition. Application of a magnetic field leads to a critical endpoint (CEP) at 1.2 K and 1.5 T and then to a QCP at 1.6 T as a second order phase line. Other known quantum critical antiferromagnets such as $\mathrm{YbRh_2Si_2}$ and $\mathrm{CeCu_{6-x}Au_x}$ all have second order phase transitions along the entire antiferromagnetic phase line. The presence of a CEP is also unique among quantum critical antiferromagnets. The phase diagram of $\mathrm{Yb_3Pt_4}$ is somewhat similar to those of the itinerant ferromagnets $\mathrm{ZrZn_2}$ and MnSi, in that they also show a phase line that has both a first and second order region, but with the second order phase line occurring first at higher temperatures but becoming a first order phase line before reaching a QCP.

- It is remarkable that the first order transition to an antiferromagnetic state coincides with the formation of a FL. The Fermi liquid crossover line, T_{FL}, does not go to zero at the QCP as it does in other quantum critical materials such as $\mathrm{YbRh_2Si_2}$ and $\mathrm{CeCu_{6-x}Au_x}$, instead terminating at the CEP, suggesting that the point influencing all the phases in $\mathrm{Yb_3Pt_4}$ is the CEP and not the QCP. The properties of the FL in $\mathrm{Yb_3Pt_4}$ are also unusual. While it is not surprising that A and χ_0 diverge on the approach to the ordered phase from the high field FL phase and then remain large in the ordered phase, which is expected in quantum critical antiferromagnets, it is surprising that γ is largely field independent in the high field FL phase and then seems to become extremely small in the ordered state. Both $\mathrm{YbRh_2Si_2}$ and $\mathrm{CeCu_{6-x}Au_x}$ show a diverging γ on approach to the QCP and a very large value of γ in the magnetically ordered phase. We propose that the explanation for this unusual behavior is found in the plot of the field dependence of R_W for $\mathrm{Yb_3Pt_4}$, which does show a zero field divergence cut off by the advent of the ordered phase. The diverging Kadowaki-Woods ratio and R_W (m* independent) show that the divergence in A (quasiparticle scattering) and χ_0 ($\sim$m*/1+F_0^a) indicate that magnetic order is driven by diverging magnetic interactions among the quasiparticles, quantified by the $1/1+F_0^a$ term and not by a diverging quasiparticle mass.

- Despite the presence of a QCP, no NFL behavior is observed in measurements of the heat capacity, magnetic susceptibility, or resistivity in Yb_3Pt_4. This differs from the results for the known quantum critical materials, both among the heavy fermion antiferromagnetic compounds like $YbRh_2Si_2$ and $CeCu_{6-x}Au_x$, in the itinerant ferromagnetic compound, MnSi and in the near quantum critical superconductors $CePd_2Si_2$ and $CeCu_2(Si_{1-x}Ge_x)_2$, all of which show various types of NFL behavior extending over wide regions of temperature and magnetic field or pressure from the QCP. Perhaps the first order character of the phase line is responsible for the weakness of the critical fluctuations in Yb_3Pt_4.

CHAPTER VII

Conclusions

We have presented the results of measurements of CaB_6, rare earth doped $PtSb_2$, and Yb_3Pt_4. We proposed to experimentally study the mechanisms leading to the electronic and magnetic phases found in materials that contain varying densities of local magnetic moments and itinerant electrons. We began by exploring the possibility of the existence of a three dimensional ferromagnetic Wigner lattice in doped CaB_6. We found that the high T_C ferromagnetism observed in a 1999 experiment likely originated with Fe and Ni contamination on the crystal surface and not with the formation of a Wigner lattice.

The next class of materials that we studied were doped magnetic semiconductors. We sought to explore the mechanisms that lead to magnetic order in $PtSb_2$ doped with rare earth elements, specifically to determine how the magnetic interactions evolve from dipolar to RKKY as the local moment and itinerant electron concentrations change. We were unable to dope sufficient amounts of rare earth elements into $PtSb_2$ to create magnetic order. Initial observations of superconductivity and ferromagnetism in some of the crystals originated with minority impurity phases and were not a property of the bulk crystal.

The bulk of our work focused on the synthesis and extensive measurements of

Yb_3Pt_4. Our primary interest is to better understand the the mechanisms behind the formation of the novel states of matter associated with magnetic systems comprised of a lattice of local magnetic moments in the presence of a high density of itinerant electrons. We found that Yb_3Pt_4 is a unique quantum critical system. Our results showed some very different behavior compared with $YbRh_2Si_2$ and $CeCu_{1-x}Au_x$. We conclude that while the presence of a QCP drives novel electronic and magnetic phases in materials like $YbRh_2Si_2$ and $CeCu_{1-x}Au_x$, in other types of quantum critical systems the same types of phases do not necessarily exist. The effect of a QCP on the physical properties of a material depends upon the specific type of magnetic order and phase transition. Thus, different types of quantum critical materials with low temperature magnetic phases need to be synthesized, studied and classified. The unique properties of Yb_3Pt_4 illustrate that we are far from a broad understanding of quantum criticality and more materials that host quantum criticality still need to be synthesized and measured.

It is highly likely that many more quantum critical systems will be found, because there remains a vast number of new materials that have not yet been grown. In the Yb-Pt phase diagram alone, we found at least three new Yb-Pt binary compounds with low temperature magnetically ordered phases. There are many more incomplete binary phase diagrams to be explored and there are even more undiscovered ternary phases, and even more undiscovered quartenary phases many of which will likely produce new quantum critical materials.

BIBLIOGRAPHY

BIBLIOGRAPHY

[1] D. P. Young, D. Hall, M. E. Torelli, Z. Fisk, J. D. Thompson, H. R. Ott, S. B. Oseroff, R. G. Goodrich, and R. Zysler. *Nature*, 397:412, 1999.

[2] C. C. Grimes and G. Adams. *Phys. Rev. Lett.*, 42(12):795, 19 March 1979.

[3] I. M. Tsidil'kovskii. *Sov. Phys. Usp.*, 30:676, August 1987.

[4] M. C. Bennett, M. C. Aronson, D. A. Sokolov, C. Henderson, and Z. Fisk. *J. Alloys and Compounds*, 400:2–10, 2005.

[5] N. W. Ashcroft and N. D. Mermin. *Solid State Physics*. Harcourt College Publishers, 1976. 717.

[6] P. G. De Gennes. *J. Phys. Rad.*, 23:510, 1962.

[7] K. Yosida. *Phys. Rev.*, 106(5):893, Jun. 1 1957.

[8] J. C. Cooley, M. C. Aronson, J. L. Sarrao, and Z. Fisk. *Phys. Rev. B*, 56:14 541, 1997.

[9] P. Gegenwart, J. Custers, C. Geibel, K. Neumaier, T. Tayama, K. Tenya, O. Trovarelli, and F. Steglich. *Phys. Rev. Lett.*, 89(056402), 2002.

[10] H.von Lohneysen. *J. Phys. Cond. Mat.*, 8:9689, 1996.

[11] N. D. Mathur, F. M. Grosche, S. R. Julian, I. R. Walker, D. M. Freye, R. K. W. Haselwimmer, and G. G. Lonzarich. *Nature*, 394:39, 1998.

[12] H. Q. Yuan, F. M. Grosche, M. Deppe, G. Sparn, C. Geibel, and F. Steglich. *Phys. Rev. Lett.*, 96:047008, 2006.

[13] H. V. Lohneyesen, A. Rosch, M. Vojta, and Peter Wolfle. *Rev. Mod. Phys.*, 79, Jul.-Sep. 2007.

[14] P. Gegenwart, Q. Si, and F. Steglich. *Nature Physics*, 4:186, Mar. 2008.

[15] G. R. Stewart. *Rev. Mod. Phys.*, 73, Oct. 2001.

[16] G. R. Stewart. *Rev. Mod. Phys.*, 78, Jul.-Sep. 2006.

[17] Quantum Design, San Diego, CA 92121-1311. *Quantum Design PPMS Hardware and Options Manuals*, 1999.

[18] Jih Shang Hwang, Kai Jan Lin, and Cheng Tien. *Rev. Sci. Instrum.*, 68(1), Jan. 1997.

[19] J. C. Lashley, M. F. Hundley, A. Migliori, J. L. Sarrao, P. G. Pagliuso, T. W. Darling, M. Jaime, J. C. Cooley, W. L. Hults, L. Morales, D. J. Thoma, J. L. Smith, J. Boerio-Goates, B. F. Woodfield, G. R. Stewart, R. A. Fisher, and N. E. Phillips. *Cryogenics*, 43:369–378, 2003.

[20] G. R. Stewart. *Rev. Sci. Instrum.*, 54(1), Jan. 1983.

[21] B. L. Zink, B. Revaz, R. Sapey, and F. Hellman. *Rev. Sci. Instrum.*, 73(4), Apr. 2004.

[22] R. Bachmann, F. J. DiSalvo Jr., T. H. Geballe, R. L. Greene, R. E. Howard, C. N. King, H. C. Kirsch, K. N. Lee, R. E. Schwall, H. U. Thomas, and R. B. Zubeck. *Rev. Sci. Instrum.*, 43(2), Feb. 1972.

[23] S. G. Doettinger-Zech, M. Uhl, D.L Sisson, and A. Kapitulnik. *Rev. Sci. Instrum.*, 72(5), May 2001.

[24] Quantum Design, San Diego, CA 92121-1311. *Quantum Design MPMS XL Hardware and Software Reference Manuals*, 1999.

[25] M. McElfresh. *Fundamentals of Magnetism and Magnetic Measurements.* Quantum Design, San Diego, CA 92121-1311, 1994.

[26] A. Arrott. *Phys. Rev.*, 108(6):1394, 1957.

[27] S. Sullow, I. Prasad, M. C. Aronson, S. Bogdanovich, J. L. Sarrao, and Z. Fisk. *Phys. Rev. B*, 62(17):11 626, 1 Nov. 2000.

[28] D. A. Sokolov, M. C. Aronson, W. Gannon, and Z. Fisk. *Phys. Rev. Lett.*, 96:116404, 2006.

[29] M. Tinkham. *Introduction to Superconductivity.* Dover Publications, 1996. 65.

[30] Z. Fisk and J. P. Remeika. *Growth of Single Crystals From Molten Metal Fluxes.* Elsevier Science Publishers B. V., 1989.

[31] T. B. Massalski, H. Okamoto, P. R. Subramanian, and L. Kacprzak, editors. *Pt-Yb Phase Diagram.* William W. Scott, Jr., 1990.

[32] www.ccdc.cam.ac.uk. *Cambridge Structural Database.* Cambridge crystallographic Data Centre, 2008. 12 Union Rd., Cambridge CB2 1EZ, U.K.

[33] H. R. Ott, J. L. Gavilano, B. Ambrosini, P. Vonlanthen, E. Felder, L. Degiorgi, D. P. Young, Z. Fisk, and R. Zysler. *Physica B*, 281-2:423–27, June 2000.

[34] R. C. O'Handley. *Modern Magnetic Materials Principles and Applications.* John Wiley and Sons, Inc., 2000.

[35] K. Matsubayashi, M. Maki, T. Tsuzuki, T. Nishioka, and N. K. Sato. *Nature*, 420:143, 2002.

[36] C. Meegoda, M. Trenary, T. Mori, and S. Otani. *Phys. Rev. B*, 67(172410), 2003.

[37] E. Wigner. *Phys. Rev.*, 46:1002, 1934.

[38] D. Ceperley and B. Alder. *Phys. Rev. Lett.*, 45:566, 1980.

[39] G. Ortiz, M. Harris, and P. Ballone. *Phys. Rev. Lett.*, 82:5317, 1999.

[40] P. Vonlanthan, E. Felder, L. Degiorgi, H. R. Ott, D. P. Young, A. D. Bianchi, and Z. Fisk. *Phys. Rev. B*, 62(10076), Oct. 15, 2000 2000.

[41] G. Allard. *Bull. Coc. Chim. Fr.*, 51:1213, 1932.

[42] L. Pauling and S. Weinbaum. *Z. Kristallog*, 87:181, 1934.

[43] H. C. Longuet-Higgins and M. V. Roberts. The electronic structure of the borides. *Proc. R. Soc. Lond. A*, 224:336–347, 1954.

[44] A. J. Arko, G. Crabtree, J. B. Ketterson, F. M. Mueller, P. F. Walch, L. R. Windmiller, Z. Fisk, R. F. Hoyt, A. C. Mota, and R. Viswanathan. *Int. Quantum Chem. Biol. Symp.*, 9:569, 1975.

[45] H. J. Tromp, P. van Gelderen, P. J. Kelley, G. Brocks, and P. A. Bobert. *Phys. Rev. Lett.*, 87(016401), 2001.

[46] S. Massidda, A. Continenza, T. M. de Pascale, and R. Monnier. *Z. Phys. B*, 102:83–89, 1997.

[47] J. D. Denlinger, J. A. Clack, J. W. Allen, G. H. Gweon, D. M. Poirier, C. G. Olson, J. L. Sarrao, A. D. Bianchi, and Z. Fisk. *Phys. Rev. Lett.*, 89(157601), 2002.

[48] J. Etourneau, J. P. Mercurio, R. Naslain, and P. Hagenmuller. *J. Solid State Chem.*, 2:332–342, 1970.

[49] D. Hall, D. P. Young, Z. Fisk, T. P. Murphy, E. C. Palm, A. Teklu, and R. G. Goodrich. *Phys. Rev. B*, 64(233105), 2001.

[50] K. Taniguchi, T. Katsufuji, F. Sakai, H. Ueda, K. Kitazawa, and H. Takagi. *Phys. Rev. B*, 66(064407), 2002.

[51] M. C. Bennett, J. van Lierop, E. M. Berkeley, J. F. Mansfield, C. Henderson, M. C. Aronson, D. P. Young, A. Bianchi, Z. Fisk, F. Balakirev, and A. Lacerda. *Phys. Rev. B*, 69(132407), 2004.

[52] F. Matsukura, H. Ohno, A. Shen, and Y. Sugawara. *Phys. Rev. B*, 57:R2037, 1998.

[53] T. Story, R. R. Galazka, R. B. Frankel, and P. A. Wolff. *Phys. Rev. Lett.*, 56:777, 1986.

[54] F. Holtzberg, T. R. McGuire, S. Methfessel, and J. C. Suits. *Phys. Rev. Lett.*, 13:18, 1964.

[55] T. Jungwirth, J. Konig, J. Sinova, J. Kucera, and A. H. MacDonald. *Phys. Rev. B*, 66:012402, 2002.

[56] R. A. Reynolds, M. J. Brau, and R. A. Chapman. *J. Phys. Chem. Solids*, 29:755, 1968.

[57] A. A. Abdullaev, L. A. Angelova, V. K. Kuznetsov, A. B. Ormont, and Y. I. Pashintsev. *Phys. Status Solidi*, 18:459, 1973.

[58] D. H. Damon, R. C. Miller, and P. R. Emptage. *Phys. Rev. B*, 5:2175, 1972.

[59] N. E. Breese and H. G. von Schnering. *Zeitschrift Fuer Anorganische und Allgemeine Chemie*, 620:393, 1994.

[60] P. R. Emptage. *Phys. Rev.*, 138:A246, 1964.

[61] J. O. Shaughnessy and C. Smith. *Solid State Commun.*, 8:481, 1970.

[62] D. H. Damon, R. C. Miller, and A. Sagar. *Phys. Rev.*, 138:A636, 1965.

[63] B. T. Matthias. *Phys. Rev.*, 92:874, 1953.

[64] Y. Yamaguchi, S. Waki, and K. Mitsugi. *J. Phys. Soc. Jpn.*, 56:419, 1987.

[65] P. C. Canfield, J. D. Thompson, and Z. Fisk. *J. Appl. Phys.*, 70:5992, 1991.

[66] R. A. Laudise, W. A. Sunder, R. L. Barns, and G. W. Kammlott. *J. Cryst. Growth*, 102:21, 1990.

[67] H. V. Lohneysen, C. Pfleiderer, T. Pietrus, O. Stockert, and B. Will. *Phys. Rev. B*, 63:134411, 2001.

[68] J. Kondo. *Prog. Theor. Phys.*, 32:37, 1964.

[69] M. A. Ruderman and C. Kittel. *Phys. Rev.*, 96(1):99, Oct. 1 1954.

[70] T. Kasuya. *Prog. Theor. Phys.*, 16(1):45, Jul. 1956.

[71] S. Doniach. *Physica B*, 91:231–234, 1977.

[72] David Pines and Philippe Nozieres. *The Theory of Quantum Liquids.* W. A. Benjamin, Inc., 1966.

[73] P. Gegenwart, J. Custers, Y. Tokiwa, C. Geibel, and F. Steglich. *Phys. Rev. Lett.*, 94:076402, 2005.

[74] O. Stockert, M. Nicklas, P. Thalmeier, P. Gegenwart, and F. Steglich. *Magnetism and Quantum Criticality in Heavy-Fermion Compounds: Interplay with Superconductivity.* John Wiley and Sons, Ltd., 2007.

[75] K. Kadowaki and S. B. Woods. *Solid State Comm.*, 58:507, 1986.

[76] D. M. Newns and A. C. Hewson. *J. Phys. F: Metal Phys.*, 10:2429–45, 1980.

[77] L. E. Delong, R. P. Guertin, S. Hasanain, and T. Fariss. *Phys. Rev. B*, 31:7059, 1985.

[78] P. G. Pagliuso, R. Movsovich, A. D. Bianchi, M. Nicklas, N. O. Moreno, J. D. Thompson, M. F. Hundley, J. L. Sarrao, and Z. Fisk. *Physica B*, 312-313:129, 2002.

[79] M. Uhlarz, C. Pfleiderer, and S. M. Hayden. *Phys. Rev. Lett.*, 93:256404, 2004.

[80] C. Pfleiderer, P. Boni, T. Keller, U. K. Rossler, and A. Rosch. *Science*, 316(5833):1871–1874, June 29 2007.

[81] P. Pedrazzini, H. Wilhelm, D. Jaccard, T. Jarlborg, M. Schmidt, M. Hanfland, L. Akselrud, H. Q. Yuan, U. Schwarz, Y. Grin, and F. Steglich. *Phys. Rev. Lett.*, 98:047204, Jan. 26 2007.

[82] S. A. Grigera, P. Gegenwart, R. A. Borzi, F. Weickert, A. J. Schofield, R. S. Perry, T. Tayama, T. Sakakibaram, Y. Maino, A. G. Green, and A. P. Mackenzie. *Science*, 306:1154, 2004.

[83] Belitz. *Phys. Rev.*, 2005.

[84] C. Pfleiderer, D. Reznik, L. Pintschorius, H. V. Lohneyesen, M. Garst, and A. Rosch. *Nature*, 427:227, 2004.

[85] J. A. Hertz. *Phys. Rev. B*, 14(3):1165, Aug. 1 1976.

[86] P. Gegenwart, Y. Tokiwa, T. Westerkamp, F. Weickert, J. Custers, J. Ferstl, C. Krellner, C. Geibel, P. Kerschl, K. H. Muller, and F. Steglich. *New J. Phys.*, 8:171, 2006.

[87] Z. Fisk, H. R. Ott, and G. Aeppli. *Japanese Journal of App. Phys.*, Supp. 26-3:1882, 1987.

[88] Y. Janssen et al. *unpulished*, 2008.

[89] A. Palenzona. *J. Less Common Metals*, 53:133, 1977.

[90] G. M. Sheldrick. *SHELXL-97 Program for Crystal Structure Refinement.* University of Göttingen, Germany, 1997.

[91] M. S. Kim, M. C. Bennett, D. A. Sokolov, M. C. Aronson, J. N. Millican, J. Y. Chan, Q. Huang, Y. Chen, and J. W. Lynn. *Phys. Rev. B*, 74:224431, 2006.

[92] K. D. Jayasuriya, S. J. Campbell, and A. M. Stewart. *Phys. Rev. B*, 31(9):6032, 1985.

[93] C. S. Durfee and C. P. Flynn. *Phys. Rev. Lett.*, 87(9):057202–1, 2001.

[94] B. Lachal, M. Ishikawa, A. Junod, and J. Miller. *J. Low Temp. Phys.*, 46(5,6), 1982.

[95] P. G. Pagliuso, J. D. Thompson, M. F. Hundley, J. L. Sarrao, and Z. Fisk. *Phys. Rev. B*, 63:054426, 2001.

[96] A. S. Chernyshov, M. I. Ilyn, A. M. Tishin, O. Y. Gorbenko, V. A. Amelichev, S. N. Mudrestsova, A. F. Mairova, and Y. I. Spichkin. *Cryocoolers*, 13:381, 2004.

[97] E. S. R. Gopal. *Specific Heat at Low Temperatures.* Plenum, Inc., New York, 1966.

[98] K. S. Kim et al. *unpublished*, 2008.

[99] F. M. Mueller, A. J. Freeman, J. O. Dimmock, and J. M. Furdyna. *Phys. Rev. B*, 1:4617, 1970.

[100] Y. Tokiwa, A. Pikul, P. Gegenwart, F. Steglich, S. L. Budko, and P. C. Canfield. *Phys. Rev. B*, 73:094435, 2006.

[101] S. I. Ikeda, Y. Maeno, S. Nakatsuji, M. Kosaka, and Y. Uwatoko. *Phys. Rev. B*, 62:R6089, 2000.

[102] M. E. Fisher and J. S. Langer. *Phys. Rev. Lett.*, 20:665, 1968.